ISSN: 1847-9286
Open Access Journal
www.jese-online.org

JESE

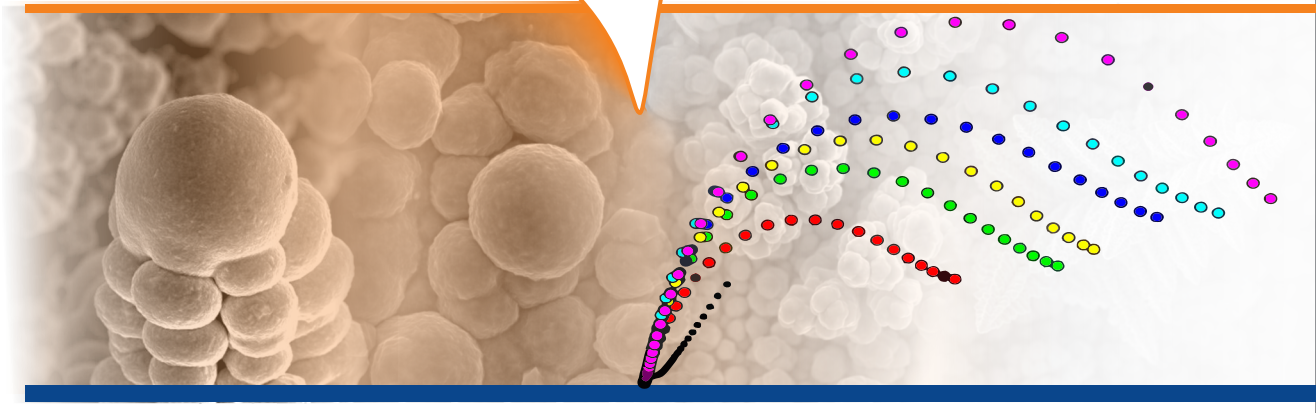

Journal of Electrochemical Science and Engineering

J. Electrochem. Sci. Eng. **14**(**4**) 2024, 417-522
Special Issue: **Advanced coatings**

IAPC Publishing

J. Electrochem. Sci. Eng. **14(4)** (2024) 417-418; http://dx.doi.org/10.5599/jese.2473

Open Access : : ISSN 1847-9286
www.jESE-online.org

Editorial

Corrosion and wear resistant advanced coatings for typical engineering applications

Hitesh Vasudev[1,✉] and Lalit Thakur[2]

[1]*Research and Development Cell, Lovely Professional University, Phagwara 144411, India*
[2]*National Institute of Technology, Kurukshetra, Haryana 136119, India*

Corresponding author: ✉hiteshvasudev@yahoo.in

Received: August 17, 2023; Accepted: August 18, 2023; Published: August xx, 2023

This special issue highlights the original research on the advanced coatings used in the various industrial applications.

The research by R. Lingappa *et al.* uses HVOF and HVAF to coat solution-treated 21-4N steel with WC-Co-Cr. The microstructure, hardness, surface quality, porosity, slurry erosion, and corrosion resistance of HVOF and HVAF coatings on solution-treated 21-4N steel were compared. The research found that the high-velocity air fuel sprayed WC-Co-Cr coating outperformed the oxygen fuel sprayed coating in erosion and corrosion resistance.

In another study by N. Kamboj *et al*., YSZ-IN625 composite cladding was placed on a stainless-steel substrate using a tungsten inert gas welding manipulator to prevent solid particle erosion. The ASTM G76-18 technique was used for room-temperature erosion wear testing. Micro-cutting, detached splats, and cracks caused composite cladding wear at 30 and 90° impact angles.

Third paper belongs to a review category, where the P.K. Verma *et al.* have discussed about the biocompatible, corrosion-resistant, and mechanically robust metallic biomaterials utilized to repair and replace human body parts. Hydroxyapatite is a good ceramic biomaterial for covering metals, because it's biocompatible with synthetic and natural bone. HAp-based thermal spray coatings to improve crystallinity and adhesion and create thick metallic biomaterial coatings are gaining popularity. The bioactivity of HAp coatings depends on their capacity to stimulate bone formation and osseointegration and their knowledge of bioactivity processes and advances.

In another review study by S. K. Awasthi *et al.*, the research has focused on surface hydrophilicity and hydrophobicity management. Surface energy frequently determines hydrophobicity. There are several ways to adjust surface energy. Intelligent nano-based materials are being utilized to generate highly hydrophobic coatings that protect metallic components from mechanical abrasion, corrosion, and fouling. Recent popularity has made these coatings great for steel pipeline protection. Spraying is the most versatile and popular method for ultra hydrophobic coatings on any substrate, according to research.

A study by M. Singh, employed powder metallurgy to create porous Ti6Al4V alloy structures with space holder powder particles was presented to this issue. To study electrochemical behavior, samples were made with different compaction pressures while other process parameters were kept the same. Microstructure study showed that increased compaction pressure densified powder particles. The research suggests using 300 MPa or greater compaction pressure to make biomedical porous materials.

In the final paper (M. S. Alam *et al.*), materials and coatings' hot corrosion resistance has been represented for the air engine operating temperatures. Hot corrosion involves oxidizing or sulphidating the substrate behind a salt melt deposit, which either forms a thick layer of sulphide scale or penetrates the matrix via grain boundaries. It may alter the thermally sprayed coating's microstructure, phase composition, and properties. Recently, thermally sprayed cermet coatings on steel have become popular for hot corrosion resistance. This review study qualitatively analyzes thermal sprayed coatings' latest hot corrosion performance improvements.

J. Electrochem. Sci. Eng. **14(4)** (2024) 419-439; http://dx.doi.org/10.5599/jese.2340

Open Access : : ISSN 1847-9286
www.jESE-online.org

Review paper

Bioactivity and corrosion analysis of thermally sprayed hydroxyapatite based coatings

Praveen Kumar Verma[1], Vinod Kumar[1] and Hitesh Vasudev[2,✉]

[1]*Department of Mechanical Engineering, Punjabi University Patiala Punjab 147002, India*
[2]*School of Mechanical Engineering, Lovely Professional University, Phagwara, Punjab 144411, India*

Corresponding author: ✉ *hiteshvasudev@yahoo.in*

Received: April 2, 2024; Accepted: July 29, 2024; Published: August 2, 2024

Abstract

Metallic biomaterials have been used to repair and replace human body parts because of their excellent biocompatibility, strong corrosion resistance, and high mechanical properties. A ceramic biomaterial that is highly suitable for coating on metallic biomaterials is hydroxyapatite. This is because it is biocompatible with synthetic and natural bone tissue. There has been a growing interest in HAp-based coatings using thermal spray techniques to enhance the crystallinity and adhesion quality and produce a dense coating of metallic biomaterials. Thermally sprayed coating material has been studied and reviewed in detail in the bioactivity analysis and electro-corrosion analysis. Furthermore, the bioactivity of HAp coatings is determined by their ability to promote bone formation and osseointegration and a valuable understanding of the mechanisms and current advancements in bioactivity. Additionally, the corrosion behaviour of thermally sprayed HAp coatings under simulated conditions has been reviewed.

Keywords

Biocompatibility; biomaterials; surface engineering; plasma spray; bio-implants; fixation devices

Introduction

Every year, approximately 2.2 million patients worldwide receive bone grafting procedures because of bone-related diseases that cause fractures [1]. Additionally, the population of the planet is growing yearly. Therefore, it is not an exaggeration to state that the need for implants to address bone issues is growing daily. Worldwide, arthritic joint replacement, osteoporosis, hip and knee replacements, correction of spinal fractures, long bone fracture fixation, and other orthopaedic and maxillofacial reconstruction applications are among the many implants uses. Improved implants with superior biocompatibility and high functionality are in great demand because of the previously indicated increase in implant demand [2].

To improve a patient's quality of life, metallic biomaterials are vital for failed tissue, particularly failed hard tissue, bone repair, and fracture fixing. This is a result of their extreme durability, toughness, and strength. However, a concern with orthopaedic implants is their deficiency of biocompatibility. The disadvantages of implants include high corrosion rates, a lack of anti-infection properties, and implant loosening because of wear debris particulates, which are toxic to human health. Therefore, in implants, one of the main issues is premature failure. For orthopaedic implants to survive over the long term, it is crucial to enhance their qualities by reducing the drawbacks. Applying a bioactive material coating to implants is one way to enhance their characteristics and lifespan [3].

Hydroxyapatite [HAp, $Ca10(PO_4)_6(OH)_2$] coating is by far the best of the several bioactive materials that are used to make implants, and it has been applied clinically to many orthopaedic sectors. Owing to its osteogenic qualities and capacity to establish robust connections with the host bone tissues, HAp has been used in calcium phosphate bioceramics to cover metal prosthetics. To create the HAp coating, numerous techniques are available. The choice of coating method and associated process parameters can affect the HAp coating's mechanical characteristics, phase composition, and crystallinity [4]. By adding HAp coatings to metallic substrates, inert metallic materials become bioactive and aid in osseointegration the process by which implants directly fuse with surrounding bone tissue, enhancing implant durability and long-term performance.

Hydroxyapatite (HAp) is often deposited on the surface of substrate implants to enhance their bioactivity in the bone by forming a factual joining with the bone tissue. Implant osseointegration development needs to be improved so that the device can fuse with the surrounding bone tissue properly. That is precisely what this approach does. After a while, the hydroxyapatite coating improves soft tissue adaption, looks better, and forms a hydroxyapatite layer necessary for bone growth and finally strengthens the bond between the implant and bone tissue [5].

HAp-based thermally sprayed coatings have attracted significant attention because of their bioactive properties and resilience to corrosion. Because of their bioactivity, these coatings have been demonstrated to help injured tissues, reduce bacterial adhesion, and enhance corrosion resistance, making them ideal for a range of biomedical. HAp coatings have been demonstrated in numerous studies to interact chemically and physiologically with body fluids while possessing antibacterial properties.

Furthermore, by reducing the surface roughness value, these coatings lessen the adherence of germs [6-7]. The techniques for preventing corrosion are shown in Figure 1.

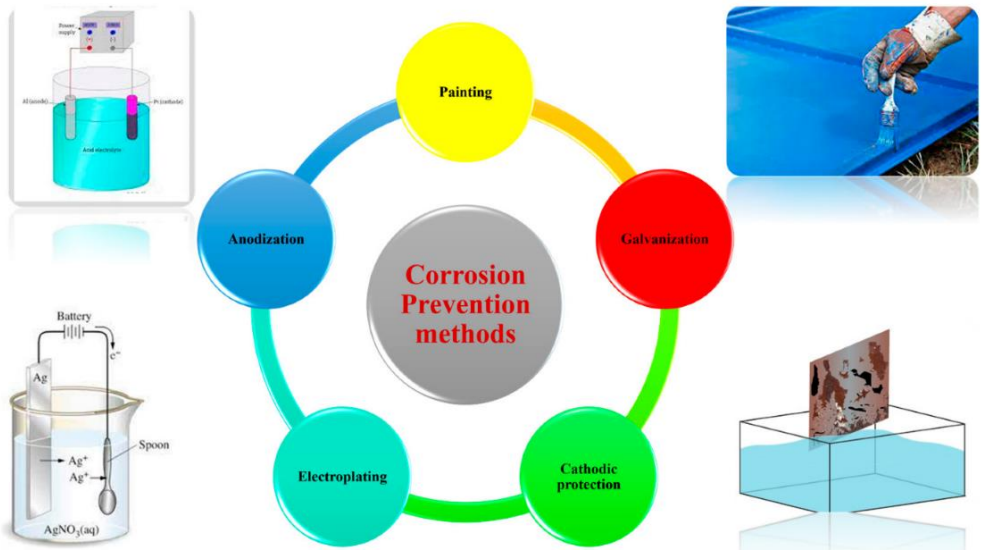

Figure 1. *Techniques for preventing corrosion [8] (CC BY 4.0 Attribution)*

Hydroxyapatite

The inanimate phase of bone areas contains HAp carbonate apatite, deficient in calcium. The phases HAp of calcium phosphate are utilized in bone replacement and repair of bone graft materials and as coatings on metallic implants to help fixation to the bone without cement because of their chemical resemblance to bone minerals [9].

HAp can be applied to metallic implants using a variety of coating methods. Metals' non-bioactivity aspect can be readily made up for by using HAp because the strong interaction between the coating and the implant with HAp coating promotes the growth of new bone. Moreover, HAp coating functions as a protective film against corrosive bodily fluids. Additionally, by delaying the pace at which metallic ions dissolve, this HAp coating reduces the likelihood of leaching, as well as increases their biological activity, and slows down the rate of disintegration. Furthermore, the coating containing HAp has better bone conductivity and biological activity [10].

There are numerous coating techniques available for applying HAp to metallic implants. High-velocity oxyfuel spraying (HVOF), dip coating, sol-gel, and flame spraying are some of these methods. Because thermal spray coating leaves a homogeneous layer on metal surfaces, it is currently the most effective and widely used method for coating metallic implants. Figure 2 shows the hexagon-shaped crystalline structure of HAp [11].

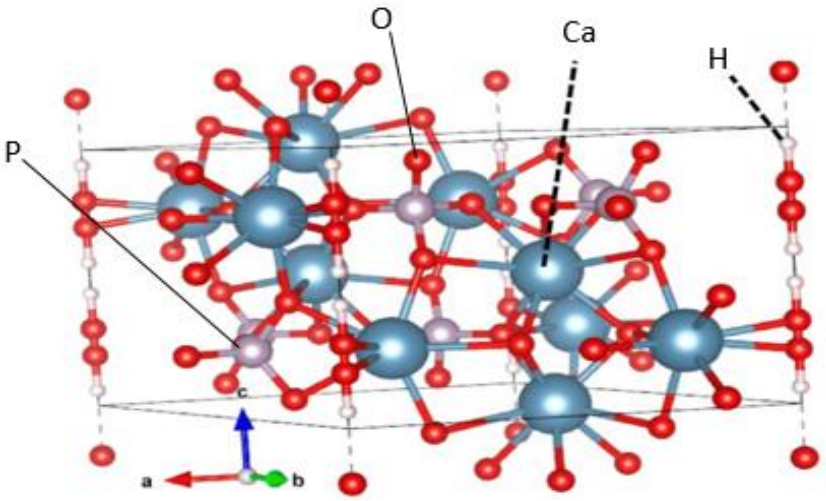

Figure 2. *Hexagonal crystal structure of HAp [12] (CC BY 4.0 Attribution)*

Antibacterial efficacy

The ability of a substance or material to effectively suppress or eliminate germs is referred to as antibacterial effectiveness. The antibacterial qualities of hydroxyapatite, a biocompatible substance that is frequently utilised in dentistry and medicinal applications, have drawn interest.

Research indicates that the antibacterial activity of HAp can be markedly increased by doping it with components. It has been discovered that some elements, including cerium, magnesium, zinc, and silver, significantly improve HAp's antibacterial capabilities. Several previous investigations have shown the strong antibacterial activity of doped HAp against a range of human pathogenic microorganisms. For instance, Ag/Mg and Ag/Zn doped HAp showed strong antibacterial activity.

Using techniques like microwave-assisted combustion, it has been possible to synthesise HAp with antibacterial qualities, demonstrating its promising potential. Moreover, dopant compounds can modify HAp, which does not naturally possess antibacterial capabilities and can demonstrate antibacterial activity. The creation of sophisticated antibacterial materials with HAp is made possible by these discoveries [13,14].

Adhesive strength

The main issue that arises when coating HAp on a metallic surface is inadequate HAp binding. This results from the low adhesive bond between the HAp layer and metallic load-bearing locations. Because of HAp's poor crystalline structure, HAp film connection on the metallic surface begins to decrease and eventually fails.

As the metal surface begins to expose itself to the body's environment, this failure causes the release of metallic ions. Surface modifying chemicals help produce a strong layer over the metallic surface and are necessary to improve the adherence of HAp films [15]. Figure 3 illustrates the bonding mechanism of thermal sprayed coating.

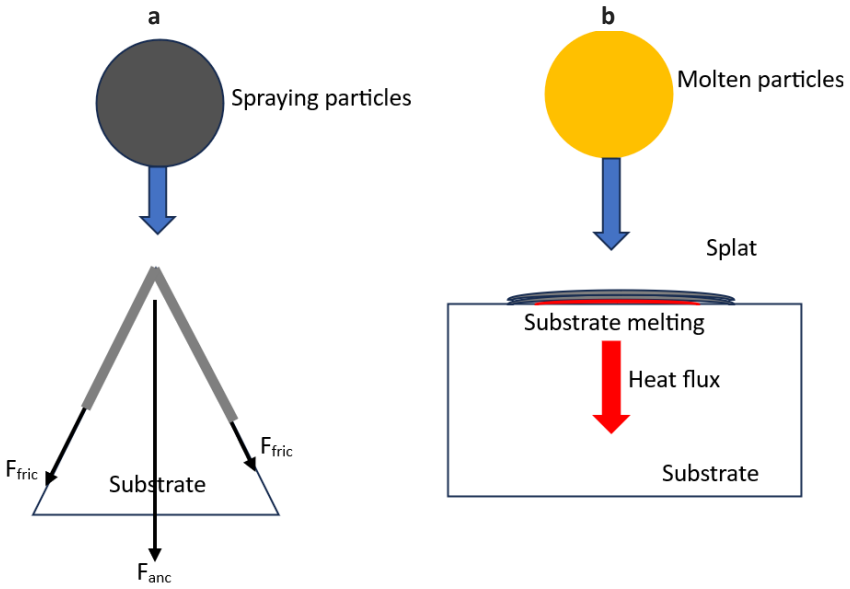

Figure 3. *Thermally sprayed coating mechanism: (a) mechanical anchor, (b) metallurgical bonding [16] (CC BY 4.0 Attribution)*

Adhesion and cohesion

An attractive force holding the two surfaces together is called adhesion between different layers. To keep the two surfaces apart, this force opposes the imposed stress. Adhesives are non-metallic substances applied to two surfaces to prevent their separation by binding them together. Applying adhesive has several benefits, such as stress distributions, processing simplicity, aesthetic appeal, and reduced processing costs. This glue connects the two surfaces with a significant binding force by penetrating the substrate's microchannels. Numerous additional forces operate on the layers when adhesives bind disparate surfaces. These forces consist of chemical forces, mechanical interlocking, and physical adsorption.

The substrate and adhesive form hydrogen bonds, which cause the adhesive layer to adhere to the substrate's surface. There is a chemical bond between the substrate and the coated substance. These chemical connections have a very high strength, which helps the coating resist deterioration from the outside environment.

For improved adhesion between the adhesive and substrate, the rough surface increases the interfacial area. To fully wet the surface, adhesive needs to have wetting capabilities to provide the best outcomes. It dries out and becomes stronger after application, sharing and transmitting the load amongst the neighboring layers [17].

The intrinsic force of attraction between molecules in a coated film is known as cohesiveness. It is essential to guarantee the coating's efficacy and longevity. Because it keeps the coating from

flaking off or delaminating over time, especially in harsh environments or when the coated surface is subjected to mechanical stress, high cohesiveness is very significant. It takes a variety of criteria, including coating material formulation, surface preparation, and application technique, to successfully establish high cohesion in HAp coatings.

The cohesiveness of the coating is essential to guaranteeing the long-term efficacy and stability of the medical implants since HAp coatings aim to stimulate bone formation and facilitate implant integration [18].

Metallic biomaterials

Biomaterials that closely resemble the original material they intend to replace are frequently the most successful. High strength, Young's modulus compatible with bone-to-load wearing, porosity, low density and resistance to corrosion and wear are necessary for biomaterials intended for use in orthopaedics and load-bearing applications [19].

Metallic biomaterials are widely used in orthopaedic implants, dental implants, and cardiovascular devices. They are mostly composed of metals like titanium, stainless steel, and cobalt-chromium alloys [20]. The various metal implants used in the human body are shown in Figure 4.

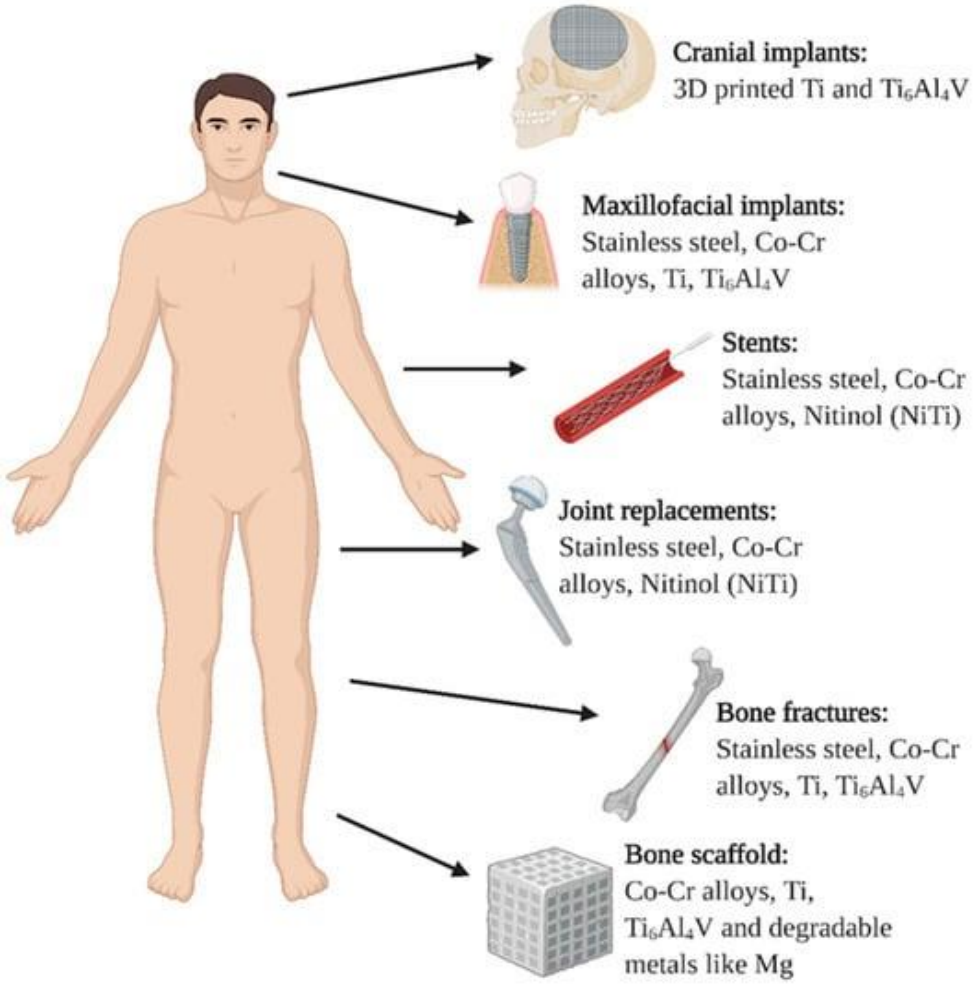

Figure 4. *Metal implants used in the human body [21] (CC BY 4.0 Attribution)*

Bone engineering, a method to regenerate injured bone tissue, focuses on creating a bionic system that combines cells, scaffolds, and bioactive substances to enable repair [22]. The n-HAp composite scaffolds with added bioactive substances and therapeutics exhibit a high capacity to promote the

growth and repair of bone tissues. Usually utilized bioactive chemicals are lipids, flavonoids, hormones, peptides, amino acids, and protein growth factors. Furthermore, drugs including alendronate, deferoxamine, dexamethasone, simvastatin, and antibiotics like ciprofloxacin, moxifloxacin, and gentamicin have been used to promote bone regrowth and prevent infections [23].

Bioactive agents for bone defects are placed into an n-HAp composite scaffold as shown in Figure 5.

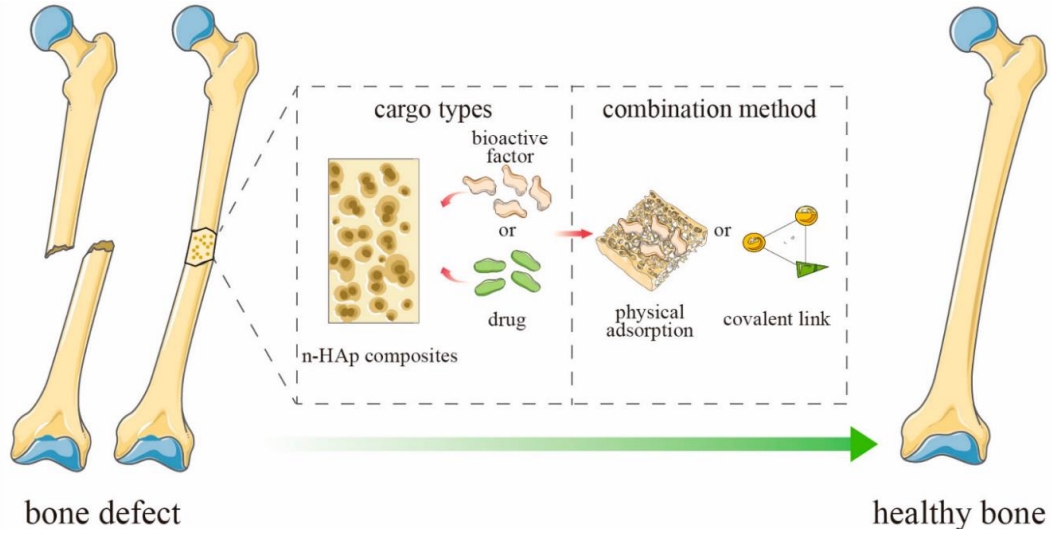

Figure 5. *n-HAp composite scaffold for a bone deficiency filled with bioactive substances or medications [27] (CC BY 4.0 Attribution)*

Deposition by thermal spraying

Thermal spraying is useful for biomedical applications, including orthopedic and dental implants, for applying HAp coatings on substrates. There are certain unique issues and difficulties with the adherence, crystallinity, and biocompatibility of the coatings when HAp is deposited using thermal spraying techniques [24].

Flame spraying

The flame spray coating for biomedical implants has various advantages. It generates coatings that are resilient to corrosion, less poisonous, and capable of establishing a bond between bone and implants. This cost-effective process improves the wear-resistant, biocompatibility of implants and protects them from electromagnetic and radiofrequency interference. It will also enhance adhesion strength, microstructure, thickness modification, and phase structure control [25].

However, flame spray coating has several drawbacks, especially when applied to biomedical implants. Because of the extreme heat, strong UV light, and vapors containing potentially hazardous ingredients, there are dangers to one's health and safety throughout this operation [26]. Figure 5 shows the n-HAp composite scaffold for a bone deficiency filled with bioactive substances or medications.

Plasma spraying

Orthopaedics have made extensive use of metallic implants coated with plasma-sprayed HAp. The fundamentals behind plasma spraying are the use of electrical discharge between electrodes to create a plasma flame, which is then used to heat HAp particles to extremely high temperatures.

It is commonly known that throughout this thermal process, once the coating cools, there is partial apatite disintegration and the creation of numerous secondary phases, all of which can be succinctly summed up by the thermal stability of apatite. The plasma spray coating to biomedical metallic implants has been the subject of numerous studies [28].

The HAp and β-TCP coating on Ti using plasma spraying for orthopaedic and dental applications. It was discovered that a tuneable solubility of the composite coatings could be achieved for orthopaedic applications by choosing a particular composition and applying various heat treatments [29].

The correlation between the spray constraint, the frequency of dissolution, and the surface properties of coatings was found, and as the plasma power and spraying distance increased, the HAp's phase purity and crystallinity gradually declined. They demonstrated that significantly better particle melting occurred on coated surfaces sprayed at higher power and greater distances. It has also been observed that coatings sprayed at a greater power exhibited a pattern resembling bone apatite, while coatings sprayed at a lesser power had a crystalline HAp structure. The thick, adherent, and bioactive coatings can be produced using plasma spraying techniques, according to numerous studies [30].

Vacuum plasma spraying

One innovative technique used to apply highly functional coatings on biomedical implants is vacuum plasma spraying (VPS). Other advantages of the VPS techniques for deposition in biomedical implants are that the coating deposition is very rapid, coatings may be vacillatingly thin or thick, and the slow solidification of the coating allows the residual stresses to be contained. Lastly, it helps in new bone formation around the implant, which is critical to improving long-term efficiency. Biomedical implants thus benefit from VPS in terms of osseointegration, hardness, antimicrobial properties, coefficient of friction, wear resistance, and other mechanical and biofunctional properties of vacuum plasma sintering coatings [31].

High-velocity oxy-fuel (HVOF) spraying

HVOF spraying is an effective technique for coating deposition on biomedical implants. This intricate procedure produces thick coatings that are very wear-resistant, have a low porosity, and a strong binding strength [32].

Since the improvement in deposition efficiency and the consistency of the coatings made, the second method is now the most often mentioned way to alter the surface of biocompatible materials that come into touch with live tissue. The FDA has authorized atmospheric plasma spray (APS) as a thermal spray technique for the fabrication of bioactive coatings for medical devices. Several studies have used HVOF to limit the pace of HAp degradation by fabricating coatings. A HAp-based coating's corrosion resistance and bioactive behavior were both enhanced by this method [33].

Detonation spraying (or detonation gun)

The high-velocity thermal spray technique is widely used to provide medical implants with protective coatings, enhancing the devices' mechanical and biological properties. The ability to create coatings using detonation gun spray methods results from HAp's aptitude for easy deformation at elevated temperatures [34].

HAp-oriented crystals: a comparable droplet deposition technique reveals the same features. It is crucial to differentiate between the two phases inside the coatings because an amorphous phase might be produced by quickly cooling melts with a composition like HAp. Applying cathodoluminescence microscopy to the coated surface allows for the differentiation of crystalline zones [35]

Cold spraying

As a thermal spray technique, cold spraying involves forcing a compressed gas to expand at supersonic speeds through a converging-diverging nozzle. This extension enables the rapid production of coatings using powdered ingredients. High-pressure inert gas nitrogen is used in cold spraying (HPCGS),

whereas compressed air is used in low-pressure cold spraying (LPCGS). Powder fusion does not occur when solid-state bonding is used to cling the sprayed powder particles to the substrate surface [36].

Therefore, when the deformation rates are 10^8 s^{-1} or higher, the particles' impact kinetic energy in the interfacial region between the substrate and the surface leads to the formation of viscoelastic or, with increasing speed, elastoplastic energy. In the future, the production of cold spray coatings arwill be based on the compaction of the material, causing the particles to stack due to solid-state impacts; thus, the characteristics of the form-dense coatings will be formed. It is possible to create cold spray coatings only because the sprayed powder has a certain ductility. Solid-phase powders of ceramic materials, particularly hydroxyapatite, have a brittle mechanical behaviour in the solid state and fall apart if it exceeds the elastic limit. So, the model and physical-mathematical predictions are not always true, and the established critical velocity in cold spraying for metals and other materials cannot be used to create coatings on ceramics [37].

However, Khlifi *et al.* [38] have specifically conducted a study on the hydroxyapatite of the HAp coatings' nanomechanical properties, adhesion, and corrosion resistance. Indeed, the HAp coatings on the Ti6Al4V alloy were deposited with the use of the electrodeposition technique. It was prepared at various concentrations of H_2O_2, which influenced the electrolyte and, shortly afterward, after the heat treatment. Furthermore, the surface of HAp coatings' morphologies before and after treatment and the subsequent cross-sections were analyzed with the help of scanning electron microscopy coupled with X-ray microanalysis for the identification of the phase and evaluate the composition via X-ray diffractometer. At the same time, corrosion resistance via electrochemical testing evaluated the uncoated, as-deposited, and heat-treated coatings with three concentrations of hydrogen peroxide 0, 6, and 9 % was conducted as well. Figures 6 and 7 illustrate the SEM-EDXS and XRD study results.

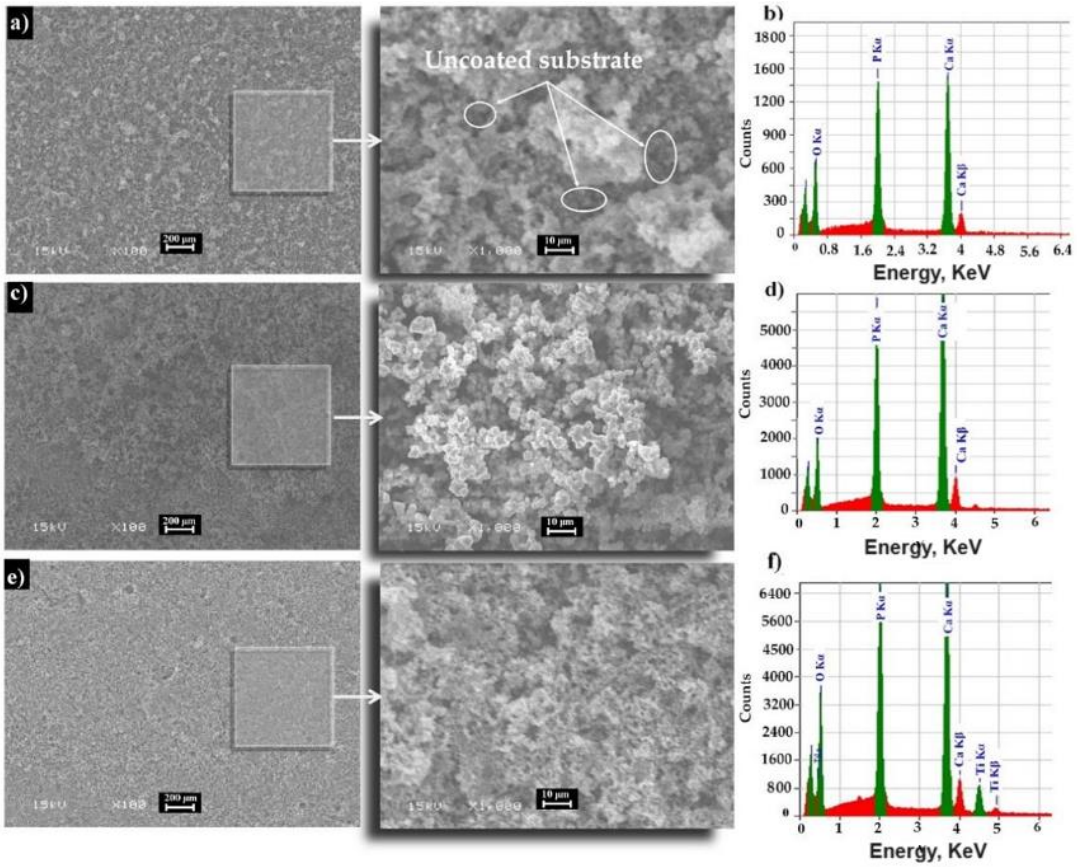

Figure 6. *HAp coatings with varying H_2O_2 contents were analyzed by SEM-EDXS: (a,b) 0 %, (c,d) 6 %, and (e,f) 9 %. for corrosion resistance of coatings [38](CC BY 4.0 Attribution)*

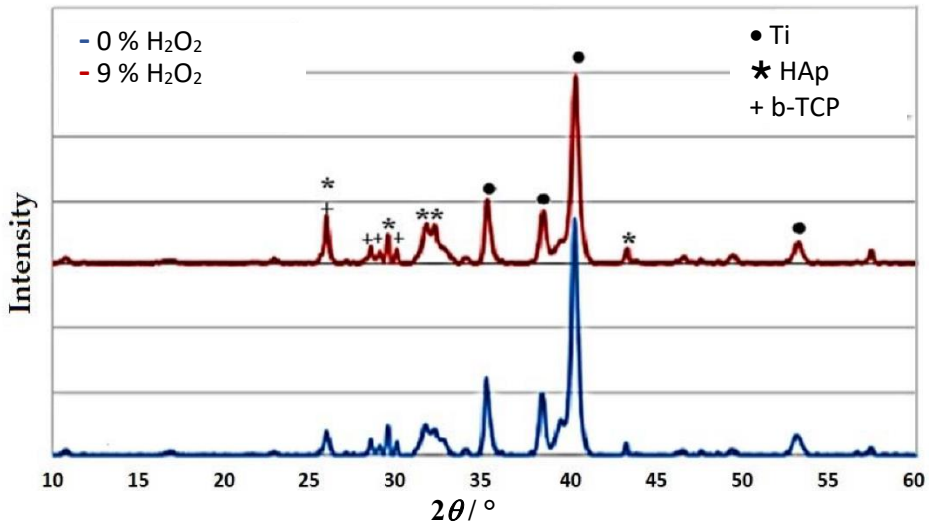

Figure 7. *X-ray diffraction patterns of HAp coating applied with 0 % and 9 % H_2O_2[38] (CC BY 4.0 Attribution)*

Bioactivity analysis

The most recent generation of functionalized bioactive bone substitute materials encourages the growth of new bone, catalyzes the body's regenerative process because of their exceptional mechanical strength, replaces the skeleton's supporting role, and allows for full regeneration of the original tissue because they are resorbable. However, the interaction of components to produce measurable biological reactions is the aim of the bioactivity analysis. It includes many things, such as how biological effects are measured, what influences bioactivity, and possible uses. Bioactivity is measured using a variety of techniques, including as functional metabolomics, *in vivo* and *in vitro* procedures, and methods in simulated body fluids (SBF) to test their biocompatibility. The potential for apatite production on the surfaces can be examined in these model fluids. The only constituents of most SBFs present in the same concentration as the natural fluids are the inorganic ions of blood plasma; no proteins, amino acids, or vitamins are present. There are two possible types of tests: dynamic and static. Given the continuous movement of body fluids, the dynamic approach may be a more accurate means of assessing biocompatibility. Static tests, on the other hand, are more commonly used and less complex in the literature. However, the outcomes of these tests do not always align with the findings of the *in vivo* tests, indicating that the *in vitro* trials are insufficient to accurately assess the bioactivity of the artificial materials [39]. Biocompatibility can also be determined by using stem cells. Cell investigations can produce more accurate evidence of bioactivity than SBF tests, but they are far more expensive and need sterile laboratory conditions and suitable microscope equipment [40]. Table 1 shows the bioactivity analysis of various materials coated with HAp.

Blum *et al.* [41] have used the simulated bodily fluid (SBF) solution in the *in vitro* bioactivity test. The HAp-coated Ti rod was immersed in the 100 mL SBF solution for 28 days, whose pH value was adjusted to 7.4, and during the test, the temperature was maintained at 37 °C. After the test, the coated rod was dried at 100 °C for 1 day and was examined using an SEM and XRD.

Patty *et.al.* [43] examined the titanium coating's mechanical properties and bioactivity using hydroxyapatite and bovine collagen. Based on the supposition that the surface apatite's nucleation capacity is connected to its bioactivity, the SBF test is the sole chemical model offered as a gauge of the implant surface's biological activity.

Figure 9 shows the SEM images of Ti/HAp-1, Ti/HAp-3, and Ti/HAp-coll before SBF immersion. Ti/HAp-3's solid-agglomerate surface results from the high HAp content (3 %), although Ti/HAp-1

and Ti/HAp-coll exhibit porous surfaces following calcination. During the ten days of SBF immersion, every sample exhibited a compact HAp block and a fully enclosed surface shape. On Ti/HAp-1 and Ti/HAp-3, the HAp block diameter was 1-2 µm, but on Ti/Hap-coll, it was 3 to 5 µm.

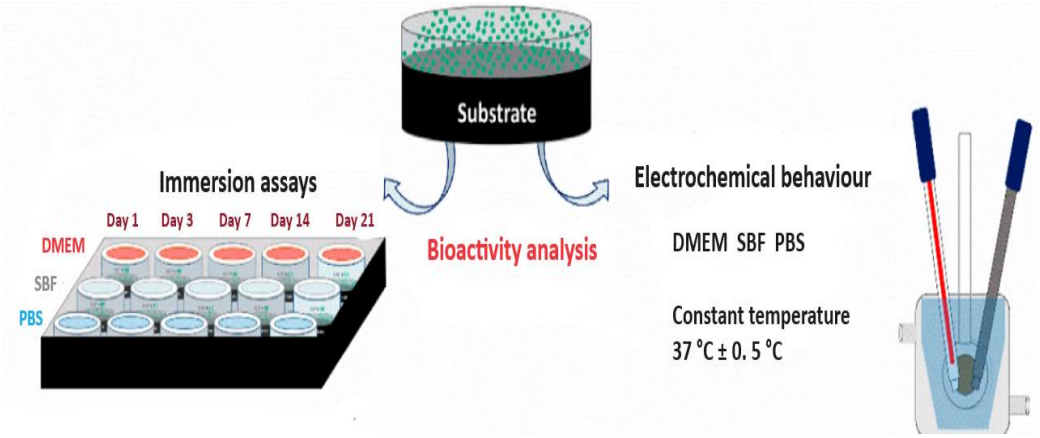

Figure 8. *Schematic illustration of the experimental setup of bioactivity analysis [42] (CC BY 4.0 Attribution)*

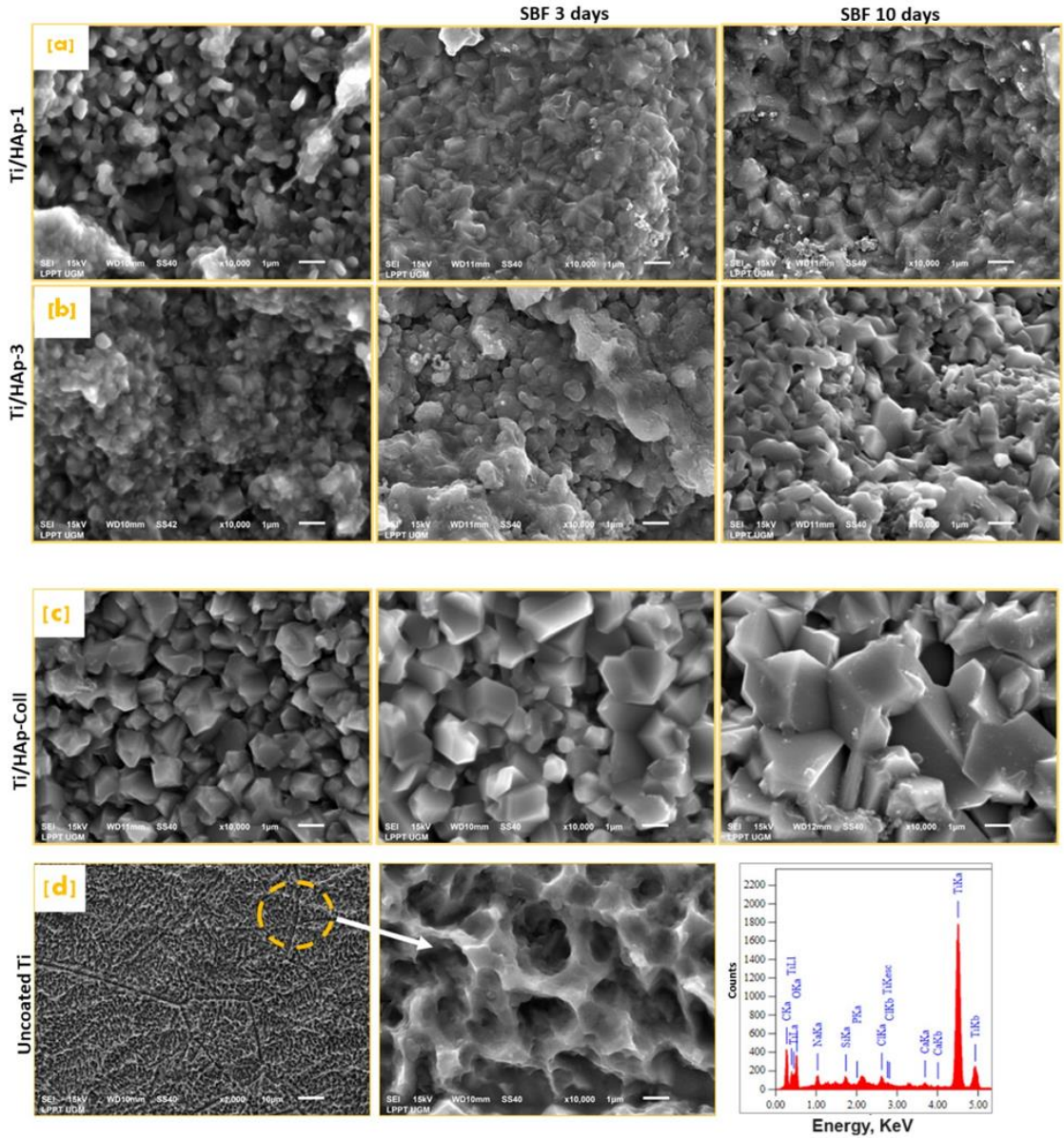

Figure 9. *Ti substrates' surface morphology both before and after SBF immersion, Ti/HAp-1 (a); Ti/HAp-3 (b), Ti/HAp-coll (c), and uncoated Ti after 3 days SBF immersion with EDS spectra (d) [43] (CC BY 4.0 Attribution)*

Table 1. *Bioactivity analysis of various materials coated with HAp*

V_{SBF} / ml*	SBF condition	Day of immersion in SBF	t_I / °C**	Materials / Powders	SBF	Ref.
50	Static	21	-	316 L / HAp	Solution used for 3-10 days	[43]
40	Dynamic	14	36.5 ± 1	254SS / HAp	Solution used for 14 days	[44]
-	-	14	37 ± 0.5	316 L SS / HAp	Freshly solution is used every 48 hours	[45]
700	Dynamic	-	37	SS - 316 L / HAp		[46,47]
-	Dynamic	3-10	37	Ti/ HAp	Freshly solution is used every two days	[48]
150	Dynamic	7	37	HAp-C nano-composites	-	[49]

*Volume of SBF; **Incubator temperature

Electrochemical corrosion analysis

The oxidation and wear of implant materials can cause HAp coated components to corrode and produce particle debris. Irreversible material degradation from chemical reactions characterizes this electrochemical process, which can be made worse by various elements, including mechanical forces, inflammation, and constrained geometries resembling crevices. Several elements contribute to the deterioration and wear of the underlying substrate and protective layer in the case of HAp-coated materials. Thus, for efficient analysis and mitigation methods, it is crucial to comprehend the corrosive behaviour of HAp-coated materials and the factors causing this phenomenon [50].

Electrochemical impedance spectroscopy (EIS) and linear sweep voltammetry (LSV) have been acknowledged as two of the most dependable quantitative methods to investigate the mechanism of electrochemical reactions at interfaces and diagnose corrosion for biomedical applications [51]. Figure 10 shows the schematic setup of the electrochemical corrosion test.

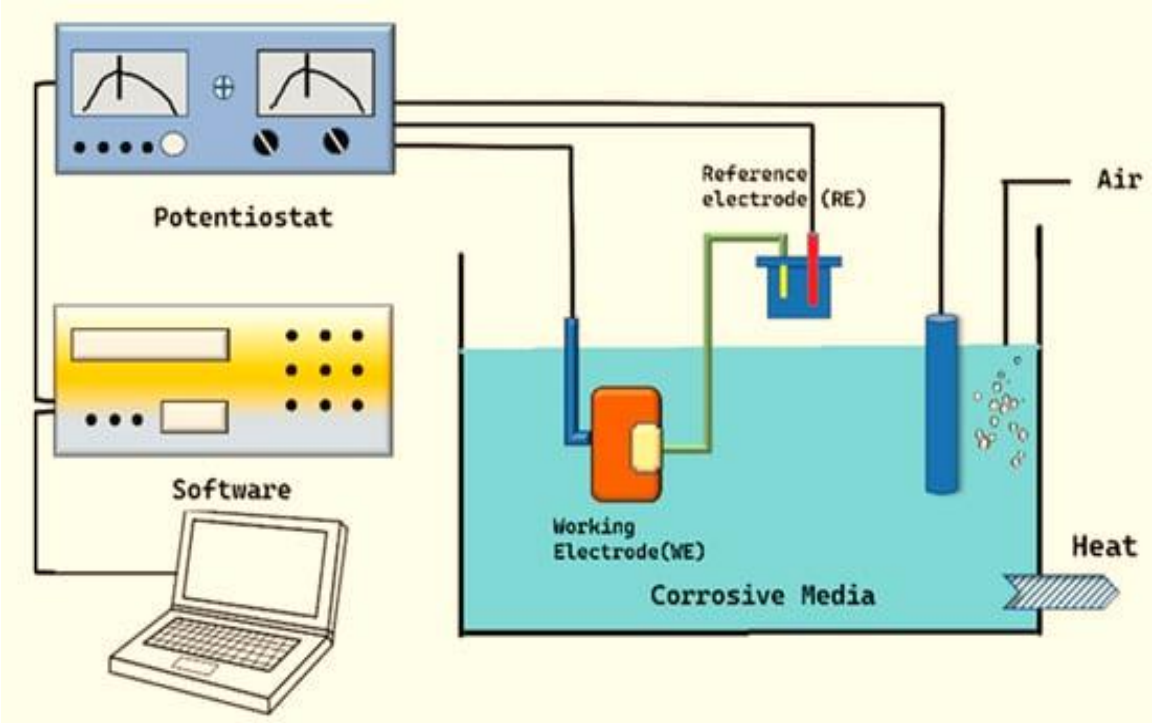

Figure 10. *Schematic diagram of the electrochemical corrosion test [52](CC BY 4.0 Attribution)*

Corrosion behaviour

The corrosion resistance of HAp coatings is an important factor to consider, especially for metallic substrates in physiological settings, even if they offer high biocompatibility and bioactivity. In

addition to causing unfavorable biological reactions, corrosion can weaken the mechanical integrity of the implant. Numerous parameters, including coating thickness, porosity, and microstructure, have been shown to influence the corrosion behavior of HAp coatings. As opposed to partly melted coatings, dense and uniform coatings show higher corrosion resistance. Implants coated with HAp may behave differently in terms of corrosion depending on the substrate type and surface pretreatment used [53]. The electrochemical behavior of different materials is shown in Table 2.

Table 2. *The electrochemical analysis of various materials.*

Biomaterial	Key features	Electrochemical corrosion analysis	Ref.
Titanium	Outstanding mechanical characteristics, frequently utilized in implants	Corrosion resistance is frequently evaluated using electro-chemical methods including electrochemical impedance spectroscopy (EIS) and potentiodynamic polarization.	[54]
Stainless steel	High strength and corrosion resistance	The corrosion behavior under physiological settings may be assessed with the use of electrochemical techniques. Studies using potentiodynamic polarization show how resistant coatings are to corrosion.	[55]
Cobalt-Chromium	Superior resistance to wear, frequently found in orthopedic implants	The evaluation of HAp coatings' ability to withstand hostile conditions using an electrochemical corrosion study contributes to the longevity of implants.	[56]
Magnesium	Biodegradable and appropriate for transient implantation	For transient implant applications, electrochemical testing shed light on how HAp coatings on magnesium substrates corrode.	[57]
Polymers	Adaptable and appropriate for soft tissue engineering	The durability of HAp coatings on polymer substrates is crucial for biocompatibility and long-term performance, and an electrochemical corrosion study helps to understand this.	[58]

Corrosion analysis of sprayed HAp coatings

Thermally sprayed HAp coatings, including those applied by atmospheric plasma spraying (APS) techniques, have improved the biomaterials' corrosion performance with encouraging results.

The substrate material, surface preparation, and coating thickness are three important aspects that affect the corrosion resistance of thermally sprayed HAp coatings [59]. The selected substrate material, whether Ti-20%Co alloy, ASTM A36 steel, AZ31B Mg alloy, NiTi alloys, substantially affects the HAp coating-substrate corrosion behavior [60]. The corrosion resistance of the coatings in various conditions, such as saltwater and simulated bodily fluid, can also be influenced by surface roughness and the presence of nanoparticles like ZnO or TiO_2 inside the HAp coating. Critical factors influencing the coating's overall effectiveness and ability to withstand corrosion are the HAp layer's thickness and sintering temperature. Improved corrosion protection has been proven by thicker and denser sintered HAp coatings [61].

The corrosion resistance of thermally sprayed HAp coatings is commonly assessed using standard testing techniques such as polarization resistance measurements, electrochemical impedance spectroscopy (EIS), and salt spray testing (ASTM B117). These techniques offer a thorough evaluation of the coating's functionality in many settings [62].

Influence of corrosion behavior on biomaterial performance

Because of the chemical processes between the material and its surroundings, corrosion is an electrochemical process defined as irreversible material degradation. Because metallic biomaterials' corrosion behaviour affects their functioning, sustainability, and biocompatibility, it is frequently evaluated for quality control and failure analysis. It has been proposed that biocompatibility increases with corrosion resistance.

Although metallic biomaterials have a strong corrosion resistance, it has recently been suggested that implanted biomaterials will begin to physically deteriorate after 12 to 15 years due to electrochemical processes. Consequently, when designing and choosing biomaterials for biomedical purposes, corrosion is thought to be a significant consideration. Because of the body's aqueous liquids, the implants that have been inserted have difficulties with corrosion behaviour because of electrochemical reactions. The most important elements of bodily fluids that influence how metallic implants corrode are chloride, pH, and dissolved oxygen. Sulphur, hydrogen, potassium, sodium, magnesium, and calcium ions are among the major cations found in bodily fluids. However, significant anions consist of phosphate, hydroxide, chloride, sulphate, and bio-carbonate. As far as metallic implants are concerned, the dissolved salts have the greatest impact on how they corrode [63].

Mechanical integrity of coated implants

The hydroxyapatite (HAp) coating considerably improves the mechanical integrity of implants when compared to those that are not coated. Mechanical integrity is favored by the coating's ability to lower the rate of corrosion, strengthen bonds, and slow down decomposition. The localized corrosion of the alloy is greatly reduced by HAp coatings, which improves the mechanical integrity of the alloy while it is in use. Coated implants have better qualities than bare metallic implants as well. Additionally, the coating enhances osteogenesis and exhibits improved osteoinductive and osseointegration activities by promoting hard-tissue differentiation, macrophage polarisation, and the production of new bone. Moreover, quick osseointegration and long-term stability have been linked to HAp coating, which has produced encouraging clinical outcomes like higher implant stability and improved survival rates. It is imperative to consider plausible reasons for the failure of HAp-coated implants, such as inadequate adhesion between the coating and the metal, HAp coating deterioration due to bodily fluid contact, fatigue cracks, delamination, fretting wear, and instability of the HAp film. Complications include implant loosening, non-union, bacterial infections, and material deterioration from mechanical pressures can result from these failure types [64].

Strategies for enhancing bioactivity and corrosion resistance

To increase the bioactivity and corrosion resistance of thermally sprayed HAp coatings, several tactics have been investigated. These include adding bioactive chemicals, changing coating compositions, improving spray settings, and post-treatment methods, including surface modification and heat treatment. Furthermore, research has been conducted on sophisticated coating designs, including gradient and multilevel structures, to enhance the mechanical and biological performance of HAp coatings [65].

A wide range of implant applications have significantly used metallic biomaterials, including titanium alloys, cobalt-based alloys, and stainless steel, in the medical profession because of their superior mechanical qualities and compatibility with physiological environments. The main issue with these metallic implants is that their chemical makeup does not exactly match human bone, which might result in poor bone-implant integration and implant failure.

HAp coatings have been widely applied to metallic implants via thermal spraying techniques, such as plasma spraying, among other coating methods. Using these methods, a coating layer is created by melting and rapidly moving HAp powder particles in the direction of the substrate. However, weak adhesion strength, large porosity, and the possibility of phase breakdown during the high-temperature deposition procedure frequently restrict the performance of these thermally sprayed HAp coatings [66].

Improving adhesion strength

The strength of adhesion between the hydroxyapatite and the metallic substrate plays an integral role in the lifespan of an implant. In this case, the application of coupling chemicals, including titanium, proves to be an efficient way to enhance the bonds.

Moreover, these chemicals cause the chemical composition of the coating and substrate to realize a more potent chemical bond. When working with titanium, the element contributes to the development of a durable interfacial layer, which significantly improves mechanical interlocking and increases adhesion strength overall. This is a requirement for implant parts to remain strong and intact under physiological conditions. The result is the elimination or reduction of the coating's risks of falling off or peeling, which keeps HAp attached to the substrate. This ensures the maintained composure of the formation throughout its life cycle. This, in turn, is necessary for the implant's high performance and reliability. Thus, coupling chemicals, where titanium can be named as an example, is a viable method of designing durable implants [67].

Controlling coating microstructure

The HAp coatings are the most important factor in determining their bioactivity and corrosion resistance in the microstructure. Thus, the HAp microstructural characteristics also include some attributes that have a notable effect on the behavior of these coatings on orthopedic and dental implants at the porosity, crystallinity, and phase composition of HAp. As low porosity is desirable for HAp coatings in terms of strength, high porosity levels may cause a mechanical failure of the coating and increase the chances of its corrosion, as the porous structure supports (PSS) fracture. In the case of HAp crystallinity, on the other hand, higher levels have been observed to be more conducive to the bioactivity and structural stability of the coating. Among the methods to improve the quality of HAp coatings produced with PSS, modifying the deposition methods commonly used on a wide scale makes them ready for utilization in advanced deposition methods such as suspension plasma spraying (SPS) and high-velocity suspension plasma spraying(HVSPS). SPS and HVSPS both involve the injection of a suspension of fine HAp powder in a liquid medium into a plasma jet [68].

These techniques provide a controlled environment for deposition, leading to a decreased porosity in the coatings due to inadequate sintering. The rapid solidification and high kinetic energy associated with SPS and HVSPS resulted in a more homogeneous, crystalline structure. The improved crystallinity exhibited by the SPS and HVSPS coatings makes them more bioactive. They have a more favorable surface topography for bone-forming cell attachment and a slower rate of dissolution in the biological environment. Moreover, because they are less porous, they are more resistant to fluid infiltration, making them more resistant to corrosive action on the metallic substrate [69].

Incorporation of reinforcing materials

Coatings with such reinforcing components have already been widely explored. Although TiO_2 has not been substantially utilized in coatings, some authors suggest that, by increasing the hardness and wear resistance, TiO_2 can dramatically improve coating durability. Carbon nanotubes increase the strength and flexibility of coatings, making them more durable and tougher. ZrO_2 makes the structure of the coating more rigid by enhancing its heat resistance and increasing the hardness. These materials strengthen membranes and improve them in terms of environmental resistance along with several other beneficial properties. For difficult conditions, oxide systems can provide coatings resistant to chemical attack and corrosion. Additionally, CNTs can enhance a coating's ability to withstand mechanical stress and delamination. These substances also contribute to the

adhesion of the coating to the substrate. This is crucial for adhesion-seeking applications since the film may peel off or collapse under working stress without high adherence [70].

Post-deposition treatment

Post-deposition treatments, annealing, and sintering play a vital role in optimizing the properties of thermally sprayed hydroxyapatite coatings. These processes increase crystallinity, which is essential for enhancing the bioactivity of coatings because better-crystallized hydroxyapatite provides a surface that is more suitable for bone cell adherence and proliferation. Furthermore, increased crystallinity also increases the adhesion strength, such that the coatings are more firmly attached to the substrate in physiological conditions. Annealing involves heating the coatings to a specific temperature below the melting point at which atoms diffuse and internal stresses are relieved. This process refines the microstructure in such a way that porosity is reduced and density is increased. Sintering is done at higher temperatures, at which the bonding between particles is facilitated by densifying the coatings, where atom diffusion promotes the elimination of voids and density is further increased. Better crystallinity, adhesion strength, and density collectively result in better bioactivity and corrosion resistance. Hence, enhanced bioactivity ensures that the HAp coatings adequately allow bone integration, while better corrosion resistance ensures that the aluminum substrate does not degrade in the biological environment. Therefore, post-deposition treatments significantly enhance the performance and service life of thermally sprayed HAp coatings [71]

Future scope

In the biomedical field, thermally sprayed HAp-based coatings are valued for their bioactive qualities and resistance to corrosion. To further progress in various fields, such as biomedical engineering, aerospace, automotive, and marine industries, researchers are actively looking for ways to improve these coatings [72].

Future research endeavors might focus on enhancing the bioactivity of HAp coatings to enhance the longevity and functionality of biomedical implants. Increased integration with biological systems will be made possible by this. Investigating how to modify and adjust these coatings to meet specific industrial needs, whether related to mechanical strength or corrosion resistance [73].

Due to the advent of sophisticated characterization techniques, researchers are now able to investigate the intricate relationships between structure and property at the nanoscale, providing valuable insights for the optimization of coating performance. Additionally, the quest for multifunctional coatings is an exciting area for future study because they offer corrosion resistance and bioactivity in addition to other characteristics like antibacterial or drug transport properties.

The application of these coatings in various industries will rise with the incorporation of sustainability and eco-friendliness into the synthesis processes and the assessment of their environmental impact. Cutting-edge technologies like additive manufacturing and nanotechnology can be combined by researchers to push the frontiers of innovation and open new potential for HAp-based coatings. In summary, there are numerous opportunities to advance our understanding and use of thermally sprayed HAp in the future [74].

Conclusion

The evaluation of the bioactivity and corrosion analysis of HAp-based coatings includes a detailed investigation of the behavior of corrosion and thermal spray coating features. The observation by other studies that HAp coatings increase the material's resistance to corrosion validates the results.

Studies on the development of HAp coatings, particularly for orthopedic applications, have shown how important it is to understand cold spray techniques to carry out HAp deposition. The potential applications of these coatings in biomedical implants are increasing continuously due to ongoing research activities. The chemical face and surface topology, as well as their phase stabilities of thermally sprayed HAp coatings, significantly affect bioactivity. Osteogenic and bone-bonding properties can be improved by adding more bioactive elements such as Sr, Mg, and Zn. The essential elements for the enduring integration of bioimplants in the human body are advised to be the biological functions and the properties of the transformed surface. To guarantee the Biocompatibility and biofunctions of biomaterials, HAp-based coatings are necessary. This leads to superior osseointegration and quicker formation of the hard tissues.

References

[1] M.W. Archunan and S. Petronis, Bone grafts in trauma and orthopaedics, *Cureus* **13** (2021) 17705. https://doi.org/10.7759/cureus.17705

[2] R. B. Heimann, Plasma-Sprayed Hydroxylapatite Coatings as Biocompatible Intermediaries Between Inorganic Implant Surfaces and Living Tissue, *Journal of Thermal Spray Technology* **27** (2018) 1212-1237. https://doi.org/10.1007/s11666-018-0737-8

[3] P. Gkomoza a , M. Vardavoulias a , D.I. Pantelis b , Ch. Sarafoglou b., Comparative study of structure and properties of thermal spray coatings using conventional and nanostructured hydroxyapatite powder, for applications in medical implants, *Surface & Coatings Technology* **357** (2019) 748-758. https://doi.org/10.1016/j.surfcoat.2018.10.044

[4] Seisho Take, Tusyoshi Otabe, Wataru Ohgake, Taro Atsumi, Effect of Ti intermediate layer on properties of HAP plasma sprayed biocompatible coatings, *Corrosion Science and Technology* **19** (2020) 51-56. https://doi.org/10.14773/CST.2020.19.2.51

[5] Xuanyong Liu, Paul K. Chu, Chuanxian Ding, Surface modification of titanium, titanium alloys, and related materials for biomedical applications, *Materials Science and Engineering R: Reports* **47** (2004) 49-121. https://doi.org/10.1016/j.mser.2004.11.001

[6] C. C. Berndt, Fahad Hasan, U. Tietz, K.-P. Schmitz, A review of hydroxyapatite coatings manufactured by thermal spray. *Advances in Calcium Phosphate Biomaterials* **2** (2014) 267-329. https://doi.org/10.1007/978-3-642-53980-0_9

[7] J.F. Kay, Plasma sprayed hydroxyapatite coatings for enhanced biocompatibility, *Materials Technology* **8** (1993) 26-29. https://doi.org/10.1080/10667857.1993.11784929

[8] K. Bijapur, V. Molahalli, A. Shetty, A. Toghan, P. De Padova, and G. Hegde, Recent Trends and Progress in Corrosion Inhibitors and Electrochemical Evaluation, *Applied Sciences (Switzerland)* **13** (2023) 1017. https://doi.org/10.3390/app131810107

[9] N. Donkov, A. Zykova, V. Safonov, D. Kolesnikov, I. Goncharov, S. Yakovin, and V. Georgieva, Modification of the structure and composition of $Ca_{10}(PO_4)_6(OH)_2$ ceramic coatings by changing the deposition conditions in O_2 and Ar, *Journal of Physics: Conference Series, Institute of Physics Publishing,* **514** (2014) 012017. https://doi.org/10.1088/1742-6596/514/1/012017

[10] K. Balani, R. Anderson, T. Laha, M. Andara, J. Tercero, E. Crumpler, A. Agarwal, Plasma-sprayed carbon nanotube reinforced hydroxyapatite coatings and their interaction with human osteoblasts *in vitro*, *Biomaterials* **28** (2007) 618-624. https://doi.org/10.1016/j.biomaterials.2006.09.013

[11] M. C. Bautista, J. H. Bedoya, B. O. Bautista, J. C. Castuera, A. L. Giraldo-Betancur, D. G. Espinosa-Arbelaez, J. M. Alvarado-Orozco, G. A. Clavijo-Mejía, L. G. Trapaga-Martínez, C. A. Poblano-Salas, HVOF Hydroxyapatite/Titania-Graded Coatings: Microstructural, Mechanical,

and In Vitro Characterization, *Journal of Thermal Spray Technology* **27** (2018) 1302-1321. https://doi.org/10.1007/s11666-018-0811-2

[12] M. Ammar, S. Ashraf, and J. Baltrusaitis, Nutrient-Doped Hydroxyapatite: Structure, Synthesis and Properties, *Ceramics* **6** (2023) 1799-1825. https://doi.org/10.3390/ceramics6030110

[13] S. Sutha, K. Kavitha, G. Karunakaran,V. Rajendran, In-vitro bioactivity, biocorrosion and antibacterial activity of silicon integrated hydroxyapatite/chitosan composite coating on 316 L stainless steel implants, *Materials Science and Engineering* **33** (2013) 4046-4054. https://doi.org/10.1016/j.msec.2013.05.047

[14] Poblano-Salas, Carlos A., John Henao, Astrid L. Giraldo-Betancur, Paola Forero-Sossa, Diego German Espinosa-Arbelaez, Jorge A. González-Sánchez, Luis R. Dzib-Pérez, Susana T. Estrada-Moo, and Idelfonso E. Pech-Pech, HVOF-sprayed HAp/S53P4 BG composite coatings on an AZ31 alloy for potential applications in temporary implants, *Journal of Magnesium and Alloys* **12** (2024) 345-360. https://doi.org/10.1016/j.jma.2023.12.010

[15] M. Meischel, J. Eichler, Martinelli, U. Karr, J. Weigel, G. Schmöller, E.K. Tschegg, S. Fischerauer, A.M. Weinberg, S.E. Stanzl-Tschegg, Adhesive strength of bone-implant interfaces and in-vivo degradation of PHB composites for load-bearing applications, *Journal of the Mechanical Behavior of Biomedical Materials* **53** (2016) 104-118. https://doi.org/10.1016/j.jmbbm.2015.08.004

[16] Z. Song, H. Li, Plasma Spraying with Wire Feeding: A Facile Route to Enhance the Coating/Substrate Interfacial Metallurgical Bonding, *Coatings* **12** (2022) 615. https://doi.org/10.3390/coatings12050615

[17] W.S. Lei, K. Mittal, Z. Yu, Adhesion measurement of coatings on biodevices/implants: A critical review, *Reviews of Adhesion and Adhesives* **4** (2016) 367-396. https://doi.org/10.7569/RAA.2016.09713

[18] K. K. A. Mosas, A. R. Chandrasekar, A. Dasan, A. Pakseresht, D. Galusek, Recent Advancements in Materials and Coatings for Biomedical Implants, *Gels* **8** (2022) 323. https://doi.org/10.3390/gels8050323

[19] Y. Oshida and Y. Guven, 10 - Biocompatible coatings for metallic biomaterials, *Surface Coating and Modification of Metallic Biomaterials* **10** (2015) 287-343. https://doi.org/10.1016/B978-1-78242-303-4.00010-7

[20] S. Kaur, S. Sharma, and N. Bala, A comparative study of corrosion resistance of biocompatible coating on titanium alloy and stainless steel, *Material Chemistry and Physics* **238** (2019). https://doi.org/10.1016/j.matchemphys.2019.121923

[21] M. Bencina, M. Resnik, P. Staric, I. Junkar, Use of plasma technologies for antibacterial surface properties of metals, *Molecules* **26** (2021) 1418. https://doi.org/10.3390/molecules26051418

[22] Md Al-Amin,A. M. Abdul-Rani, M. Danish, S. Rubaiee, A. b. Mahfouz, H. M. Thompson,S. Ali, D. Rajendra Unune, M. H. Sulaiman, Investigation of coatings, corrosion and wear characteristics of machined biomaterials through hydroxyapatite mixed-EDM process: A review, *Materials* **14** (2021) 3597. https://doi.org/10.3390/ma14133597

[23] W.S.W. Harun, R.I.M. Asri, J. Alias, F.H. Zulkifli, K. Kadirgama, S.A.C. Ghani, J.H.M. Shariffuddin, A comprehensive review of hydroxyapatite-based coatings adhesion on metallic biomaterials, *Ceramics International* **44** (2018) 1250-1268. https://doi.org/10.1016/j.ceramint.2017.10.162

[24] R. K. Guduru, U. Dixit, A. Kumar, A critical review on thermal spray based manufacturing technologies, *Materials Today: Proceedings* **62** (2022) 7265-7269. https://doi.org/10.1016/j.matpr.2022.04.107

[25] A. Killinger, R. Gadow, Thermally Sprayed Materials for Biomedical Applications, in *Encyclopedia of Materials: Technical Ceramics and Glasses* **3** (2021) 732-749. https://doi.org/10.1016/B978-0-12-803581-8.12111-3

[26] P. K. Verma, A. S. Minhas, P. Singh, S. Kumar, Slurry Erosion Behaviour of Thermal Sprayed Al_2O_3 and Cr_2O_3 Coatings for Turbine Steels, *AIP Conference Proceedings*, American Institute of Physics **2986** (2024) 020012. https://doi.org/10.1063/5.0192589

[27] X. Mo, D. Zhang, K. Liu, X. Zhao, X. Li, Wei Wang, Nano-Hydroxyapatite Composite Scaffolds Loaded with Bioactive Factors and Drugs for Bone Tissue Engineering. *International Journal of Molecular Sciences* **24** (2023) 1291. https://doi.org/10.3390/ijms24021291

[28] N.Aebli, J.Krebs, H. Stich, P. Schawalder, M. Walton, D. Schwenke, H. Gruner, B. Gasser, J. C. Theis, In vivo comparison of the osseointegration of vacuum plasma sprayed titanium-and hydroxyapatite-coated implants, *Journal of Biomedical Materials Research A* **66** (2003) 356-363. https://doi.org/10.1002/jbm.a.10508

[29] R. S. Pillai, M. Frasnelli, V. M. Sglavo, HA/β-TCP plasma sprayed coatings on Ti substrate for biomedical applications. *Ceramics International* **44** (2018) 1328-1333. https://doi.org/10.1016/j.ceramint.2017.08.113

[30] A. Ganvir, S. Nagar, N. Markocsan, K. Balani, Deposition of hydroxyapatite coatings by axial plasma spraying: Influence of feedstock characteristics on coating microstructure, phase content and mechanical properties. *Journal of the European Ceramic Society* **41** (2021) 4637-4649. https://doi.org/10.1016/j.jeurceramsoc.2021.02.050

[31] S. Kowalski, W. Gonciarz, R.Belka, A. Góral, M. Chmiela,Ł.Lechowicz, W. Kaca, W. Żórawski, Plasma-sprayed hydroxyapatite coatings and their biological properties. *Coatings* **12** (2022) 1317. https://doi.org/10.3390/coatings12091317

[32] J. Henao, O. S. Mazon, A. L. G. Betancur, J. H. Bedoya, D. G. E. Arbelaez, C. P. Salas, C. C. Arteaga, J. C. Castuera, L. M. Gomez, Study of HVOF-sprayed hydroxyapatite/titania graded coatings under in-vitro conditions, *Journal of Electrochemical Science and Engineering* **9** (2020) 14002-14016. https://doi.org/10.1016/j.jmrt.2020.10.005

[33] H.C. Melero, R.T. Sakai, Vignatti, C.A. Benedetti, A.V., J. Fernández, J.M. Guilemany, Suegama, Corrosion resistance evaluation of HVOF produced hydroxyapatite and TiO2-hydroxyapatite coatings in hanks' solution, *Materials Research* **21** (2018) 20170210. https://doi.org/10.1590/1980-5373-MR-2017-0210

[34] D. Shankar, K. Jayaganesh, N. Gowda, K. S. Lakshmi, K. J. Jayanthi, S. C. Jambagi, Thermal spray processes influencing surface chemistry and in-vitro hemocompatibility of hydroxyapatite-based orthopedic implants, *Biomaterials Advances* **158** (2024) 213791. https://doi.org/10.1016/j.bioadv.2024.213791

[35] L. Singh, V. Chawla, J. S. Grewal, A review on detonation gun sprayed coatings. *Journal of Minerals and Materials Characterization and Engineering* **11** (2012) 243-265. https://doi.org/10.4236/jmmce.2012.113019

[36] F. Taherkhani, A. List, S. Keller, N. Kashaev, F. Gärtner, T. Klassen, The Influence of Spraying Parameters and Powder Sizes on the Microstructure and Mechanical Behavior of Cold-Sprayed Inconel®625 Deposits, *Journal of Thermal Spray Technology* **33** (2024) 652-665. https://doi.org/10.1007/s11666-024-01712-8

[37] N. Hutasoit, M. A. Khalik, S. Palanisamy, 9.03 - Cold spray additive manufacturing, *Comprehensive Materials Processing (Second Edition)* **9** (2024) 25-56. https://doi.org/10.1016/b978-0-323-96020-5.00232-6

[38] K. Khlifi, H. Dhiflaoui, A. Ben Rhouma, J. Faure, H. Benhayoune, and A. B. C. Laarbi, Nanomechanical behavior, adhesion and corrosion resistance of hydroxyapatite coatings for orthopedic implant applications, *Coatings* **11** (2021) 477. https://doi.org/10.3390/coatings11040477

[39] A. Das, M. Shukla, Surface morphology and in vitro bioactivity of biocompatible hydroxyapatite coatings on medical grade S31254 steel by RF magnetron sputtering deposition, *Transactions of the Institute of Metal Finishing* **95** (2017) 276-281. https://doi.org/10.1080/00202967.2017.1323675
[40] S. Mohandesnezhad, M. Etminanfar, S. Mahdavi, and M. S. Safavi, Enhanced bioactivity of 316L stainless steel with deposition of polypyrrole/hydroxyapatite layered hybrid coating: Orthopedic applications, *Surfaces and Interfaces* **28** (2022) 101604. https://doi.org/10.1016/j.surfin.2021.101604
[41] M. Blum, M. Sayed, E. M. Mahmoud, A. Killinger, R. Gadow, S. M. Naga. In vitro evaluation of biologically derived hydroxyapatite coatings manufactured by high-velocity suspension spraying. *Journal of Thermal Spray Technology* ***30*** (2021) 1891-1904. https://doi.org/10.1007/s11666-021-01265-0
[42] A. Vlădescu, A. Pârâu, I. Pană, C. M. Cotruț, L. R. Constantin, V. Braic, D. M. Vrânceanu, In vitro activity assays of sputtered HAp coatings with SiC addition in various simulated biological fluids. *Coatings* **9** (2019) 389. https://doi.org/10.3390/coatings9060389
[43] D.J. Patty, A.D. Nugraheni, I. Dewi Ana, Y. Yusuf, Mechanical characteristics and bioactivity of nanocomposite hydroxyapatite/collagen coated titanium for bone tissue engineering, *Bioengineering* ***9*** (2022) 784. https://doi.org/10.3390/bioengineering9120784
[44] S. Tiwari, S. B. Mishra, Post annealing effect on corrosion behavior, bacterial adhesion, and bioactivity of LVOF sprayed hydroxyapatite coating, *Surface Coating and Technology* **405** (2021) 126500. https://doi.org./10.1016/j.surfcoat.2020.126500
[45] P. Singh, A. Bansal, H. Vasudev, and P. Singh, In situ surface modification of stainless steel with hydroxyapatite using microwave heating, *Surface Topography* **9** (2021) 035053. https://doi.org/10.1088/2051-672X/ac28a9
[46] E. A. Ofudje, J. A. Akande, E. F. Sodiya, G. O. Ajayi, A. J. Ademoyegun, A. G. Al-Sehemi, Yasar N. Kavil, Ammar M. Bakheet, Bioactivity properties of hydroxyapatite/clay nanocomposites, *Scientific Reports* **13** (2023). 19896 https://doi.org/10.1038/s41598-023-45646-7
[47] N. K. Mishra, S. B. Mishra, R. Kumar, Characterisation and oxidation of LVOF sprayed Al_2O_3-40TiO_2 coating on Superalloys, *Surface Engineering* **31** (2015) 349-353. https://doi.org/10.1179/1743294414Y.0000000348
[48] D. Qiu, A. Wang, Y. Yin, Characterization and corrosion behavior of hydroxyapatite/zirconia composite coating on NiTi fabricated by electrochemical deposition, *Applied Surface Science* **257** (2010) 1774-1778. https://doi.org/10.1016/j.apsusc.2010.09.014
[49] A. M. Ribeiro, A. C. Alves, F. S. Silva, F. Toptan, Electrochemical characterization of hot pressed CoCrMo-HAP biocomposite in a physiological solution, *Materials and Corrosion* **66** (2015) 790-795. https://doi.org/10.1002/maco.201407885
[50] T. S. Bedi, S. Kumar, R. Kumar, Corrosion performance of hydroxyapaite and hydroxyapaite/titania bond coating for biomedical applications, *Materials Research Express* **7** (2019) 015402. https://doi.org/10.1088/2053-1591/ab5cc5
[51] G. Manivasagam, Geetha, Durgalakshmi Dhinasekaran, Asokamani Rajamanickam, Biomedical implants: corrosion and its prevention-a review, *Recent Patents on corrosion Science* **2** (2010) 40-54. https://doi.org/10.2174/1877610801002010040
[52] K. Bijapur, V. Molahalli, A. Shetty, A. Toghan, P. D. Padova, G. Hegde, Recent trends and progress in corrosion inhibitors and electrochemical evaluation. *Applied Sciences* ***13*** (2023) 10107. https://doi.org/10.3390/app131810107
[53] P. K. Verma, S. Singh, M. Kapoor, and S. Singh, A review on the surface topography and corrosion behavior of Mg-alloy coatings for biomedical implants, *Results in Surfaces and Interfaces* **15** (2024) 100227. https://doi.org/10.1016/j.rsurfi.2024.100227

[54] B. Tian, D. B. Xie, and F. H. Wang, Corrosion behavior of TiN and TiN/Ti composite films on Ti6Al4V alloy in Hank's solution, *Journal of Applied Electrochemistry* **39** (2009) 447-453. https://doi.org/10.1007/s10800-008-9690-4

[55] M. Nabeel, A. Farooq, S. Miraj, U. Yahya, K. Hamad, and K. M. Deen, Comparison of the Properties of Additively Manufactured 316L Stainless Steel for Orthopedic Applications: A Review, *World Scientific Annual Review of Functional Materials* **01** (2023) 2810-9228. https://doi.org/10.1142/s281092282230001x

[56] B. G. Pound, Electrochemical behavior of cobalt - Chromium alloys in a simulated physiological solution, *Journal of Biomedical Materials Research Part A* **94 (**2010) 93-102. https://doi.org/10.1002/jbm.a.32684

[57] R. Kumar, P. Katyal, M. Gupta, V. Singh, Electrochemical Corrosion Behaviour Analysis of Mg-Alloys Used for Orthopaedics and Vascular Implants, *IOP Conference Series: Materials Science and Engineering* **1225** (2022) 012063. https://doi.org/10.1088/1757-899x/1225/1/012063

[58] D. Runsewe, T. Betancourt, J. A. Irvin, Biomedical application of electroactive polymers in electrochemical sensors, *Materials* **12** (2019) 2629. https://doi.org/10.3390/ma12162629

[59] E. Anees, M. Riaz, H. Imtiaz, T. Hussain, Electrochemical corrosion study of chitosan-hydroxyapatite coated dental implant, *Journal Mechechanical Behaviour Biomedical Materials* **150** (2024) 106268 https://doi.org/10.1016/j.jmbbm.2023.106268

[60] C. T. Kwok, P. K. Wong, F. T. Cheng, H. C. Man, Characterization and corrosion behavior of hydroxyapatite coatings on Ti6Al4V fabricated by electrophoretic deposition, *Applied Surface Science* **255** (2009) 6736-6744. https://doi.org/10.1016/j.apsusc.2009.02.086

[61] D. Snihirova, L. Liphardt, G. Grundmeier, F. Montemor, Electrochemical study of the corrosion inhibition ability of 'smart' coatings applied on AA2024, *Journal of Solid State Electrochemistry* **17** (2013) 2183-2192. https://doi.org/10.1007/s10008-013-2078-3

[62] L. De Micheli, C. A. Barbosa, A. H. P. Andrade, S. M. L. Agostinho, "Electrochemical behaviour of 254SMO stainless steel in comparison with 316L stainless steel and Hastelloy C276 in HCl media, *British Corrosion Journal* **35** (2000) 297-300. https://doi.org/10.1179/000705900101501371

[63] G. Manivasagam, D. Dhinasekaran, A. Rajamanickam, Biomedical Implants: Corrosion and its Prevention, *Recent Patents on Corrosion Science* **2** (2010) 1877-6108. https://doi.org/10.2174/1877610801002010040

[64] Shemtov-Yona, Keren, Daniel Rittel, An overview of the mechanical integrity of dental implants, *Biomedical Research International* **2015** (2015) 2314-6141 https://doi.org/10.1155/2015/547384

[65] Y. Huang, H. Qiao, X. Nian, X. Zhang, X. Zhang, G. Song, Z. Xu, H. Zhang, S. Han, Improving the bioactivity and corrosion resistance properties of electrodeposited hydroxyapatite coating by dual doping of bivalent strontium and manganese ion, *Surface and Coatings Technology* ***291*** (2016) 205-215. https://doi.org/10.1016/j.surfcoat.2016.02.042

[66] S. Y. Kim, Y. K. Kim, M. H. Ryu, T. S. Bae, M. H. Lee, Corrosion resistance and bioactivity enhancement of MAO coated Mg alloy depending on the time of hydrothermal treatment in Ca-EDTA solution, *Scientific Reports* **7** (2017) 9061. https://doi.org/10.1038/s41598-017-08242-0

[67] D. Shikha, M. Shahid, S. K. Sinha, Improvement in adhesion of HAP deposited on alumina after Ar+ ions implantation and its physiochemical properties, *Surfaces and Interfaces* **19** (2020) https://doi.org/10.1016/j.surfin.2020.100485

[68] A. Singh, G. Singh, V. Chawla, Mechanical properties of vacuum plasma sprayed reinforced hydroxyapatite coatings on Ti-6Al-4V alloy, *Journal of the Australian Ceramic Society* **53** (2017) 795-810. https://doi.org/10.1007/s41779-017-0093-z

[69] S. Tailor, N. Vashishtha, A. Modi, S. C. Modi, High-Performance Al_2O_3 Coating by Hybrid-LVOF (Low-Velocity Oxyfuel) Process, *Journal of Thermal Spray Technology* **29** (2020) 1134-1143. https://doi.org/10.1007/s11666-020-01033-6

[70] D. Dey, K. S. Bal, A. K. Singh, A. Roy Choudhury, Hardness and wear behaviour of multiple component coating on Ti-6Al-4V substrate by laser application, *Optik (Stuttg)* **202** (2020) 163555. https://doi.org/10.1016/j.ijleo.2019.163555

[71] M. L. Vera, M. R. Rosenberger, C. E. Schvezov, and A. E. Ares, Fabrication of TiO2 crystalline coatings by combining Ti-6Al-4V anodic oxidation and heat treatments, *International Journal of Biomaterial* **2015** (2015) https://doi.org/10.1155/2015/395657

[72] A. Ganvir, S. Nagar, N. Markocsan, K. Balani, Deposition of hydroxyapatite coatings by axial plasma spraying: Influence of feedstock characteristics on coating microstructure, phase content, and mechanical properties, *Journal of the European Ceramic Society* **41** (2021) 4637-4649. https://doi.org/10.1016/j.jeurceramsoc.2021.02.050

[73] V. Dutta, L. Thakur, B. Singh, H. Vasudev, A Study of Erosion-Corrosion Behaviour of Friction Stir-Processed Chromium-Reinforced NiAl Bronze Composite, *Materials* **15** (2022). https://doi.org/10.3390/ma15155401

[74] I. Gotman, Characteristics of metals used in implants, *Journal of Endourology* **11** (1997) 383-389. https://doi.org/10.1089/end.1997.11.383

J. Electrochem. Sci. Eng. **14(4)** (2024) 441-457; http://dx.doi.org/10.5599/jese.2259

Open Access : : ISSN 1847-9286
www.jESE-online.org

Review paper

Zirconia based hydrophobic coatings exhibiting excellent durability for versatile use

Sanjay Kumar Awasthi✉, Kamal Sharma and Aayush Gupta

Department of Mechanical Engineering, GLA University, Mathura-281406, India

Corresponding authors: ✉sanjay.mech.jmi@gmail.com

Received: January 29, 2024; Accepted: June 13, 2024; Published: July 21, 2024

Abstract

Understanding how to manage the hydrophilicity and hydrophobicity of a surface has been the focus of a lot of research in recent years. The surface's energy often controls its hydrophobic state. There are numerous techniques to realize a change in the surface energy. Smart nano-based materials are being used to create super hydrophobic coatings that will serve as layers of defence against mechanical abrasion, corrosion, and fouling agents on the surface of metallic components. These coatings, which have recently gained popularity, have shown to be excellent choices for protecting steel pipelines. The recently created super hydrophobic coatings for glass surfaces, papers, cotton, steel pipes, etc., are examined in-depth and critically in this review study, emphasizing their use in different industries. It explains how to create super hydrophobic coatings on glass substrates using various techniques and the most recent research results on various coating production techniques. An in-depth discussion is also given to the recent applications of these created super hydrophobic coatings for treatments, including anti-bio fouling, dicing, and corrosion prevention over the past five years. According to the literature, spraying is the most adaptable and popular technique for creating super hydrophobic coatings for any substrate.

Keywords

Zirconium oxide; surface modification; coating methods; superhydrophobic coatings

Introduction

Superhydrophobic surfaces have progressively come to the public's attention. Superhydrophobic surfaces are super wetting surfaces with a sliding angle (SA) of less than 10° and a water contact angle (WCA) of more than 150°. Since that time, scientists have worked very hard to comprehend the physical makeup of living things and have developed a growing fascination with mimicking the characteristics of natural surfaces that are exceptionally hydrophobic [1]. In addition, more artificial materials are being produced that mimic natural structures. Nature's lead offers a desirable method for creating sophisticated materials. Using a binary structure, we discussed how super hydrophobic combines many features. For instance, a wear-resistant structure paired with a self-cleaning coating

can result in valuable material used in various circumstances [2,3]. There are reasonable grounds to think that creating appropriate and flexible materials involves combining binary structures with multiple scales and features. The wettability condition on the surface is represented in Figure 1, and the wettability condition on the surface with angle is shown in Figure 2.

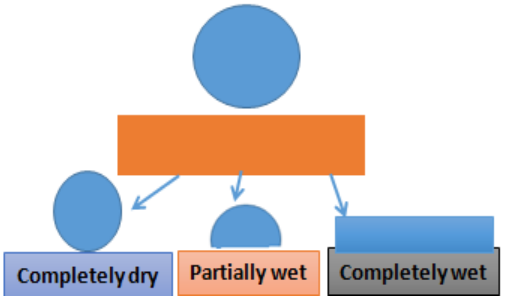

***Figure 1**. Wettability conditions on the surface*

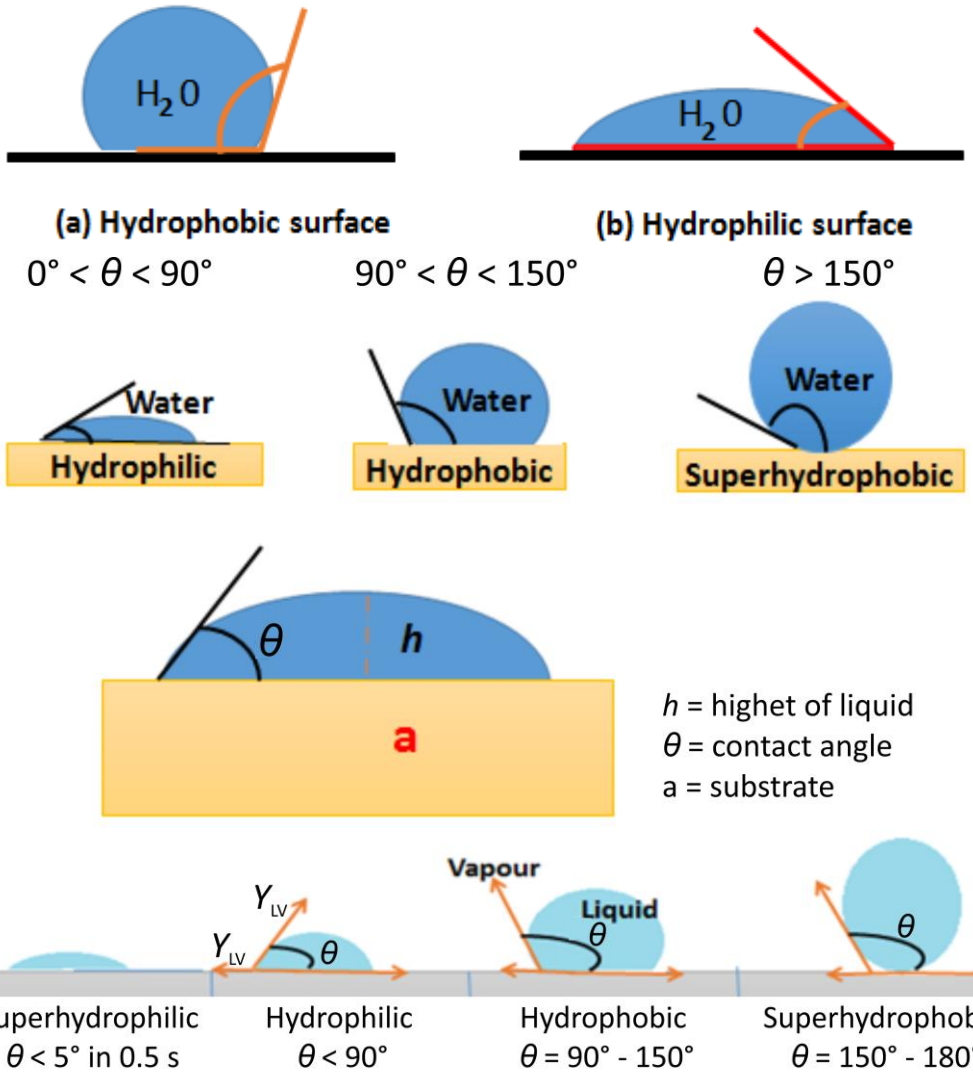

***Figure 2.** Wettability condition on a surface with an angle less than 90°*

The range of angles for the various wetting degrees in water and oil is represented in Table 1.

***Table 1**. The range of angles for the various wetting degrees in water and oil.*

The contact angle	Wettability
$0° < \theta < 90°$	Hydrophilic
$90° < \theta < 180°$	Hydrophobic
θ is less 10°	Superhydrophilic
θ is greater than 150°	Superhydrophobic

A coating is a product used to alter the colour, gloss, damage resistance, or surface of other materials, such as antibiotics, or change permeability without altering the product's volume. For specific purposes, mechanical structures and parts are created. Several strict criteria for material selection must be satisfied before making these pieces. Physical qualities, mechanical properties (such as stress, compression, yield, torsion, fatigue, bending, and penetration), performance demands (such as wear resistance, hydrophobicity, and frictional strength), and thermal stability (such as thermal expansion) are all impacted by these restrictions. After the coating of ZrO_2, the various properties of substrates, such as electrical conductivity, corrosion resistance, dynamic stress (such as vibration and high-speed spinning), and conduction heat flow, are improved. Further consideration must be given to material availability, price, safety, and toxicity. For instance, it is well known that silver has excellent electrical conductivity values, but producing significant amounts of silver for such uses is prohibitively expensive [3]. Copper has high heat and electrical conductivities, making it a good material for brazing complex materials, but it also has low stiffness and wear resistance. NiTi alloys are recognized for their superelasticity (SE) and shape memory effect (SME), which can be utilized to develop innovative actuators.

In the case of rotating copper fins, the reliance on mechanical components is significantly decreased because of copper's resistance to wear mechanisms. Various methods have been used to solve these issues and enhance qualities, such as coating, alloying procedures, and heat treatment. In the literature, coating technology has the best percentage for this process since it can save costs and disregard flaws, rarely thicker than a micron. As a result, only a few materials must be created on various substrates. Several advantages may result from the method's ability to harden, change roughness, and enhance wettability and hydrophobicity [4]. There are numerous layers due to various uses and needs in multiple sectors. However, depending on the performance needed, coating technology is effective in several applications, notably corrosion prevention and wear protection [5]. Degradation of equipment material occurs when corrosion is developed in ways that make the environment more hostile to corrosion or negatively affect specific applications [6]. The benefits and drawbacks of the various deposition techniques for layered data will be demonstrated by examining these techniques. There are numerous techniques, but just a handful are significant and efficient. These techniques include micro-arc oxidation, chemical vapour deposition, PVD, thermal spray, sol-gel and the polymer layer.

Mechanical stability, corrosion resistance, and biocompatibility are crucial factors for specific coating types, biomedical applications, and careful trade-offs because of their variety of deposits, materials, densities and thicknesses [7]. The most crucial factor in developing a successful procedure is the choice of material, as it is with all forms of protection. Materials that can create a protective layer include metals, ceramics, and polymers. However, choosing the suitable composition for the deposited layer could be challenging because of the different coating techniques and fabric characteristics. BeO, Al, Ti, Hf, Zr, Ni, Co, Pt, MgO, ZrO_2, Al_2O_3, Y_2O_3, and N and PTFE are all used in the examples with attention paid to all the underutilized possibilities to consider the most popular solutions to prevent hydrophilic properties of the substrate [8]. Each feedstock material exhibits

resistance to corrosion or wear, yet they all have unique melting points, mechanical characteristics, and chemical compositions. These models restrict the variety of materials that can be utilized in addition to the variety of powders, sticks, paper, and metal shapes they have in some projects. This evaluation does not cover all preservation techniques, including thermal treatment, mechanical treatment, and mechanical/chemical wrapping, and cleaning [9,10]. The review skims through the materials, their surface modification, and the coating method.

Techniques for dependable coating

In several industries, from the automotive and aviation sectors to microscopic biomedical devices embedded within the human body, the coating method protects specific levels or zones of structures subjected to dangerous circumstances [11,12]. Any process in which gaseous components solidify via condensation, reaction, or transformation is called vapour deposition. This technique can modify the substrate's mechanical, electrical, thermal, optical, corrosion, and wear properties. Techniques for vapour deposition can be separated into two categories: Physical vapour deposition passes a stream of impartial or ionized metal particles through the physical vapour deposition (PVD) setup, and the coating is held in place, as represented in Figure 3(a). It is possible to testify about the challenging coating using various PVD forms [13,14]. The most often used techniques are combined magnetron and bend forms, magnetron sputtering (or sputter particle plating), and cathodic bend vapour (plasma or circular segment particle plating).

In the process of chemical vapour deposition, a volatile precursor is introduced into a chamber and allowed to react (usually under vacuum). The precursor gas reacts or breaks down into the desired coating and bonds to the material surface when the chamber is heated to a reaction temperature.

The semiconductor industry extensively creates a robust, effective, high-performance layer on any substrate using high vacuum [15,16]. When mechanical components are placed close to one another, the CVD technique can be utilized to shield them from corrosion and wear, as shown in Figure 3 (b). In this procedure, a mixture of volatile material precursors is exposed to a wafer-shaped substrate, where the reaction results in the deposition of a material layer [17].

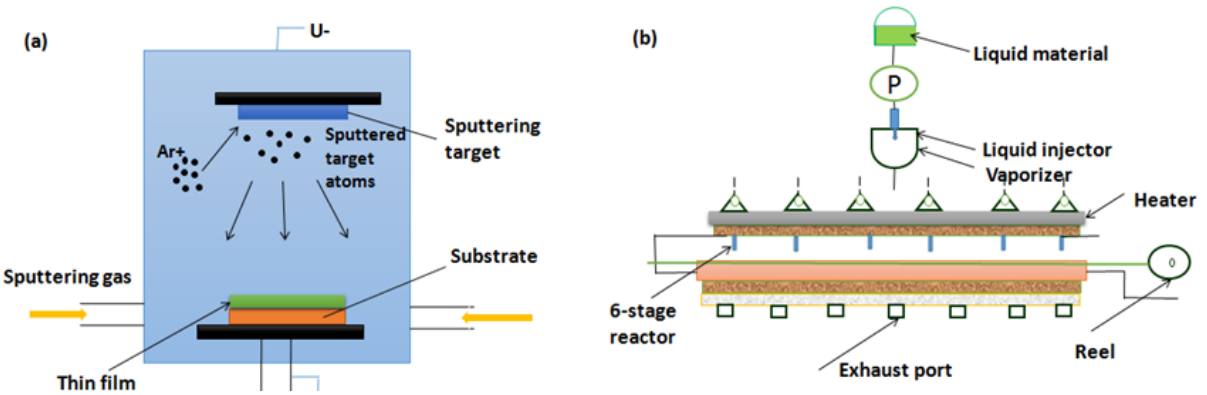

***Figure 3**. A schematic presentation of (a) physical vapour deposition (b) chemical vapour deposition CVD arrangement*

New materials are being developed for electronics, medicine, battery technology, and other vital fields. These materials should also be resistant to corrosion and wear [17,18]. Die-cast zinc and steel components are protected against cathodic corrosion by galvanic zinc coatings. The zinc coating shields the component from corrosive attacks, which degrades first. Targeted post-treatments can significantly slow down corrosive attacks on the zinc surface. Electroless coatings are represented

in Figure 4(a). One of the methods for biomedical equipment is a sol-gel coating, shown in Figure 4(b). By conducting an in-depth study on its methods and uses, it is possible to facilitate the design and execution of experiments while maintaining confidence in the results [19-21]. Sol-gels, on the other hand, can enhance ion release and corrosion in current systems. Due to their liquid permeability, sol-gels can quickly and readily cover porous and damaged layers. Sol is made by dissolving a precursor to calcium phosphate (CaP) in distilled water or ethanol [22].

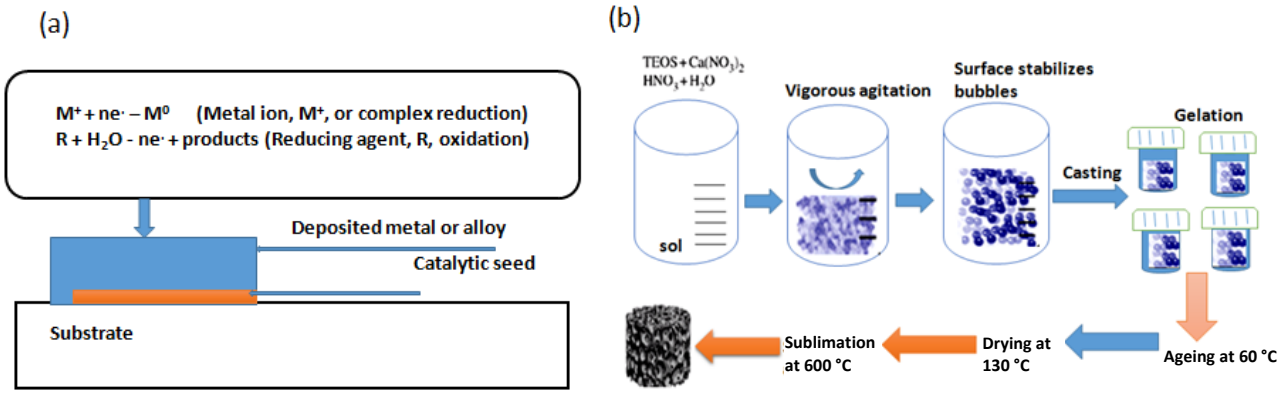

Figure 4*. (a) Electro-less coatings, (b) schematic diagram of sol-gel coating*

The term "warm sputtering" refers to processes that use heat to supply plasma, power, or chemicals to liquefy various electronic materials and spray the resulting liquid fabric over the edges of surfaces to provide a barrier covering [23]. These coatings offer reliable resistance to corrosion and wear. In this procedure, the materials are heated to a liquid or semi-finished condition by the warm medium; it is frequently produced by plasma release or chemical combustion and is subsequently sprayed with a tall, broad exposure on the substrate. The thicknesses obtained by heated sputtering preparation might vary from 20 µm to a few ml compared to galvanic coating, chemical vapour deposition (CVD), or PVD preparation. The most common varieties include plasma, blast, hot/cold, high-velocity air fuel (HVAF), high-velocity oxygen fuel (HVOF) and wire spraying [24,25]. The flow diagram of various thermal spraying processes is in Figure 5.

Table 2 shows various coating methods and their advantages and disadvantages, and Table 3 shows certain uses for nanoparticles in coatings and their purposes.

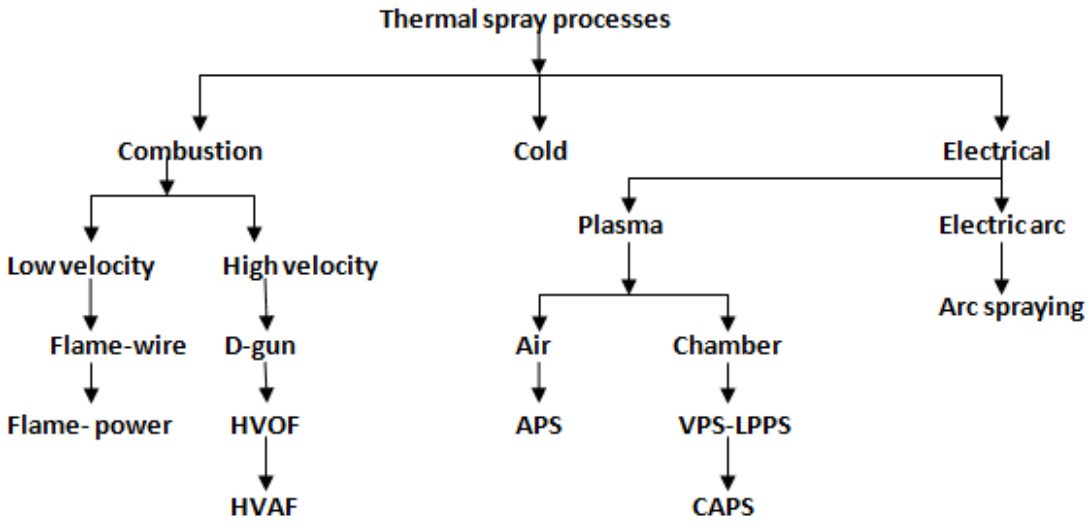

Figure 5. *Flow diagram of thermal spraying process*

***Table 2**. Various coating methods and their advantages and disadvantages with references.*

Deposition process	Advantages	Disadvantages	Ref.
PVD	Mechanical, erosion and tastefully satisfying highlights are possible/ /adjustable lean film testimony, erosion resistance	High speed is necessary for polymer deposition, wear impacts corrosion protection, and control deterioration is challenging	[26-29]
MAO	Improved High hardness, resistance to corrosion, biological applications-friendly porous structure, and a variety of porosity scales across the thickness	Mostly applicable to valve metals	[30-32]
Cold spray	This method is less complicated and more reasonably priced when considering alternative thermal spray techniques	Limited operating temperature range; mainly used for soft and hard metal surfaces; ineffective in extremely cold temperatures; low efficiency and durability due to low temperatures demanding situations	[33-36]
Warm spray	Suitable for heat-sensitive materials or materials that are susceptible to oxidation at high temperatures	Settings that are severe and have impurity issues	[37-39]
ELD	Less wear, low-corrosion, use in high-temperature and decorative applications	It is applicable to conductive substrates	[40-43]
Sol-gel	Thick and multilayered coatings, strong adhesion in biomedical applications for corrosion and ion release avoidance	Coating thickness control, a slow cycle time, and the potential for coating failure on multilayered coating systems during heat treatment	[44,45]
Arc wire spray	Coatings provide resistance to wear and corrosion on the internal engine surface	Only conductive materials and wires can be used as the coating layer	[46]
CVD	Operation at low and ambient pressure, deposition of multiple materials with varied microstates, and protection against corrosion and wear	There should be a lot of electricity, heat-resistant equipment and minimal waste of coating	[47]
HVOC	Compatibility with non-conductive surfaces, excellent substrate adhesion, high coating layer density, as well as resistance to wear and corrosion	Needs a heat source, a wide range of powder sizes (5 to 60 μm), numerous process variables, and a restricted size distribution	[48]

***Table 3.** Certain uses for nanoparticles in coatings and their purposes*

Illustrations of nanomaterials	Merits/effect	Application in industry	Function	Ref.
Zinc or aluminium can be coated using nano-TiO_2 and nano-clay(Hydrotalcite $Mg_4Al_2(OH)12CO_3{\times}H_2O$).	Wood fading (caused by the bleeding of complex compounds like tannins) is slowed down by nanoclay coatings.	Construction wood fire protection, glass, plastic	Wood preservation and corrosion prevention	[49]
Zinc oxide polystyrene (ZnO/PS)	Wood fadingis slowed down by nanoclay coatings.	Automobile, preser-vation of wood, and construction	Wood presser-vation and cor-rosion prevention	[50]
Oxides on mica flakes or SiO_2 spheres, carbon black, with metal pigments (TiO_2, Fe_2O_3, Fe_3O_4, SiO_2, and Cr_2O_3) ZnO.	The effects of metal pigments will be enhanced, the pigments and fillers will be stabilized, and dispersion paints will perform better. Phyllosilicates and sheet silicates prevent crack formation and improve fade resistance	Construction, consumer products (furniture), and the automotive industry	Repeatable paints, easily dispersible paints, colour effects (flip-flop effect), and colour brilliance and shade	[51]
SiO_2	A layer of heat-insulating carbon foam and then a coating of flame-resistant ceramic is produced on the surface of the wood when a specific temperature is reached.	Construction protection wood against fire	Fire retardant	[52]

Illustrations of nanomaterials	Merits/effect	Application in industry	Function	Ref.
Specifically, polymer gel and organic-inorganic hybrid polymers	Self-healing materials	Automotive	Switchable (electrochromic, photochromic, thermochromic)	[53]
Organically modified ceramics (organic-inorganic hybrid polymers) are created when nanosilica or colloidal silica is encased in resin particles and polymerizes.	Protection from algae and fungi, resistance to water and dirt, and anti-graffiti protection.	Automobiles, facade construction, and glass	Self-cleaning or readily cleaned	[54,55]
Transparent iron oxide, needle-shaped particles with a length of 50-100 nm and a width of 2 nm; TiO_2, ZnO, CeO_2, iron oxide pigments	Enhanced UV protection, IR and visible light blocking, and climate control inside	Building (facades), preservation of wood, glass and plastics	UV defence, IR reflection, or IR absorption	[56]
Synthetic amorphous silica Oxide	Create fresh rheological qualities, such as elasticity and thixotropy.	Various	Optimized flow characteristics	[57]
Transparent iron oxide, needle-shaped particles with a length of 50-100 nm and a width of 2 nm; TiO_2, ZnO, CeO_2, iron oxide pigments	Enhanced UV protection, IR and visible light blocking, and climate control inside	Building (facades), preservation of wood, glass and plastics	UV defence, IR reflection, or IR absorption	[58]
Fullerenes, carbon nanotubes (CNT), etc.	Improved spraying techniques	Automotive	Conductive paint coats for electrostatic spray painting	[58]
ZnO_6, TiO_2, and Ag	Grease, filth, bacteria, fungi, algae, odours, and other pollutants are eliminated, and NOx and ozone are converted into harmless chemicals in the atmosphere.	Road surface, vehicles, wood privation glass	Photocatalytic effect, antimicrobial effect	[59]

Deposition of zirconium oxide films

Thin film deposition processes fall into two categories: chemical and physical. Atoms from chemical precursors are deposited on the substrate through the liquid and gaseous phases in the chemical deposition process. Still, the physical deposition process transfers atoms directly onto the substrate using a solid source and a gaseous phase.

High-tech tools and equipment are needed for physical approaches. Chemical approaches provide ease of functioning and excellent product quality. The ZrO_2 layers have become very popular due to the films made using diverse methodologies that demonstrate varied physical and chemical features related to electricity [60]. The sol-gel method has long been the most widely used traditional method for synthesising zirconium oxide. Hydrated zirconium oxide's macro dispersed powder product is not preferred for large-scale industrial sorptive and catalytic operations. A translucent solid gel of zirconium oxide material offers several practical applications if created using sol-gel synthesis. Only a few studies have been published on the electrolysis of zirconium chloride salts, the preparation of zirconium oxide gels using zirconium alkoxides, hazardous ammonium-generating reagents [60], and mineral zirconium salts. Sol-gel formation is seen schematically in Figure 6.

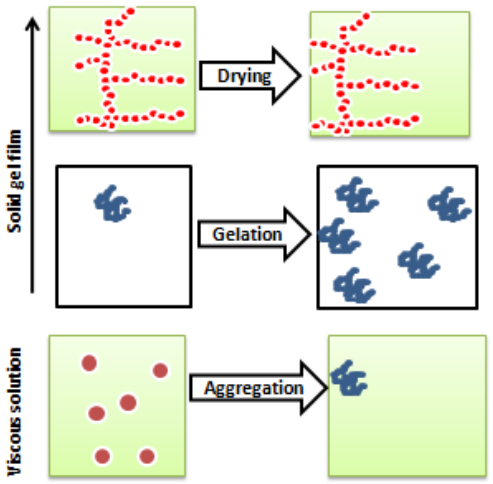

***Figure 6**. Sol-gel formations*

The electrochemical process used to grow ZrO_2 films produced during the anodization of zirconium was examined. Zirconium anodic oxidation was reported. For the oxidation process, a KOH and K_2SiO_3 solution were employed. Three different voltages were used for the anodization process: 100, 200, and 400 V. The investigation demonstrated that between 100 and 200 V, the surface shape of zirconium did not change during oxidation. Significant surface morphological alteration and silicon incorporation into the generated oxide layer were reported at 400 V. In the presence of Ringer's physiological solution, anodic oxidation of zirconium resulted in a notable improvement in corrosion resistance [61].

Sputtering is the method most frequently employed for ZrO_2 thin film deposition. Sputtering can be done in two ways: directly utilizing ZrO_2 as a source material or directly using the Zr target (see Fig. 7(a)). Zr thin films were created on silicon nitride substrates using an ultrahigh vacuum and a Zr metal target [62]. Moreover, ZrO_2 films were produced at ambient temperature using plasma oxidation. ZrO_2 thin films with a thickness range of 2.5 to 8 nm were formed on Si (001) substrate through reactive sputtering. M-ZrO_2 thin films were created using reactive DC magnetron sputtering from a Zr metal target at an ambient temperature of 400 °C with 100 to 400 W power. ZrO_2 as a target and reactive radiofrequency (RF) magnetron sputtering to build ZrO_2 films at 200 to 300 °C.

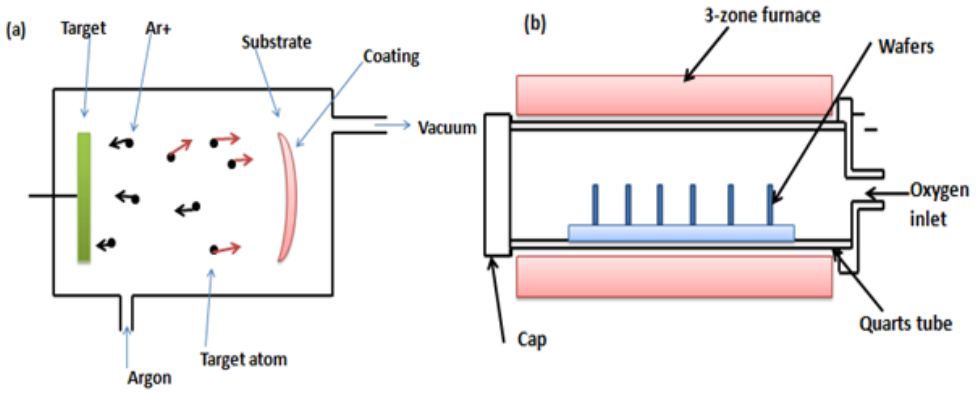

***Figure 7**. Schematic diagram of (a) sputtering method and (b) thermal oxidation method*

Synchrotron X-ray diffraction is used to study the amorphous-to-cubic (a-c) crystallization of nano ZrO_2. The alterations in lattice parameters and crystallite size as the cubic phase was detected were examined using Rietveld analysis. Utilizing a reverse Monte Carlo (RMC) simulation, the specifics of the local structure during the crystallization process and the partial pair distribution functions (PDFs)

of Zr-Zr and Zr-O during the crystallization were computed. The investigation demonstrated that the amorphous phase crystallizes into tetragonal and monoclinic ZrO_2 during oxidation. Figure 7(b) displays the thermal oxidation schematic diagram [62].

One of the more advanced deposition methods is atom layer deposition (ALD). ALD provides high thickness uniformity over a wide substrate area and accurate thickness control. In ALD, surface saturation reactions govern film growth, while the quantity of deposition cycles governs film thickness. Figure 8 shows the schematic of the ALD technique. A partial monolayer of the material is deposited on the substrate with each surface reaction cycle. Synthesized crystallinity-controlled zirconium oxide coatings on nitrogen-doped carbon nanotubes by ALD using tetrakis(dimethyl-amido) zirconium(IV) and water as a precursor. Scanning and transmission electron microscopy (TEM) revealed that the 100-cycle ZrO_2 tubular films were uniformly produced on NCNTs. The TEM, Raman spectroscopy, and X-ray diffraction showed that the crystallinity of the formed ZrO_2 films could be regulated by adjusting the deposition temperatures within the range of 100 to 250 °C [63].

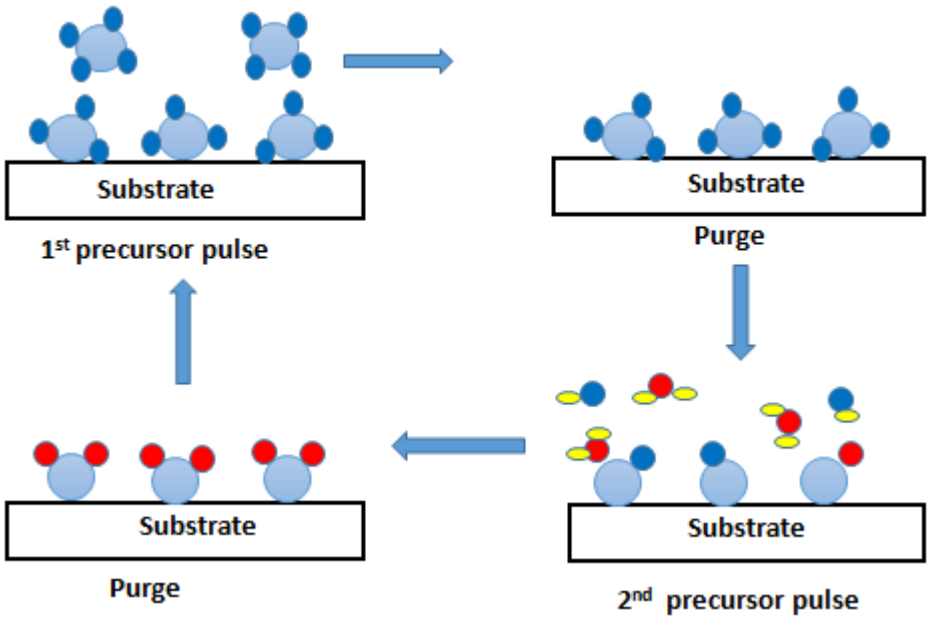

***Figure 8**. Atomic layer depositions*

In the microwave combustion method**,** ZrO_2 nanocrystals were synthesized by several researchers utilising the microwave combustion technique (MCM) using urea as fuel in the absence of surfactant, catalyst, or template. Figure 9 provides a diagrammatic illustration of MCW. ZrO_2 nanocrystals produced by microwave combustion have been used to study the photocatalytic degradation (PCD) of vital endocrine and 4-chlorophenol (4-CP) disrupting chemicals in aqueous medium [63]. The investigation proved that ZrO_2 exhibited photocatalytic activity, and ZrO_2-TiO_2 mixed oxide catalysts were tested for 4-CP PCD. To create zirconium oxide, the anticipated combustion reaction is shown in Equation (1).

$$ZrO(NO_3)_2{\times}2H_2O + CO(NH_2)_2(s) + O_2(g) \rightarrow ZrO_2(g)+4\ H_2O(g) + CO_2(g) + O_2(g) + 2\ NH_2(g) \quad (1)$$

Chemical techniques such as meniscus, spray, spin, dip, pulsed laser, and electrochemical deposition are employed to create mesoporous metal oxides. Mesoporous films with pore sizes ranging from 2 to 50 nm are helpful for catalysis and sorption. Promising uses for mesoporous thin films include photonic materials, selective permeation, sensors, sorption membranes, and photonic materials. Numerous studies have been published on developing novel synthesis techniques and characterizing mesoporous thin films with different pore sizes and chemical compositions.

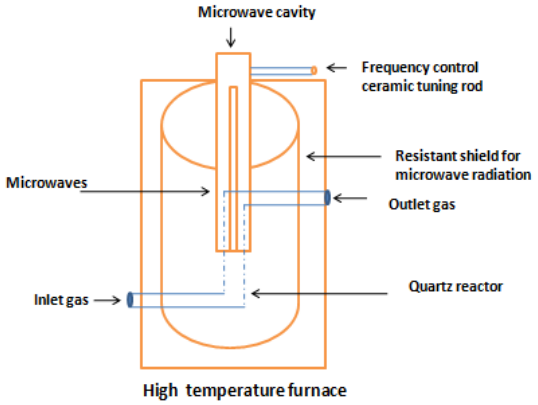

***Figure 9**. Setup of microwave combustion method*

Compared to SiO_2-derived films, zirconia is an exceptional material as determined by its physical and chemical characteristics. Because zirconia can tolerate extreme oxidising and alkaline conditions, it can be utilised to alter the surface characteristics of materials. Its refractive index, thermal resistance, and thermal expansion coefficient are all relatively high. These properties make it suitable for metal coating [63].

Required properties of ZrO_2 and their effect on different substrates

Properties of ZrO_2

With its high melting point (2680 °C), broad oxidation resistance, high refractive index, and wide region of low absorption from the near-UV (above 240 nm) to the mid-IR (below 8 mm) range, zirconium oxide (ZrO_2) is a significant material for innovation [64]. Numerous applications, including laser mirrors, broadband interference filters, and ionic conductors, find this combination of features attractive. For usage in optical and microelectronic devices, an amorphous ZrO_2 film is always favoured over a polycrystalline one, even though ZrO_2 thin films frequently condense in a partly crystalline condition. Scattering from these crystallites and grain boundaries in ZrO_2 films can lead to the degradation of optical components when subjected to high temperatures or laser intensities. Moreover, non-uniformities in the film's *k* values and film thickness will arise from distinct anisotropic crystalline phases, and grain boundaries may negatively impact the leakage current properties of crystalline ZrO_2 thin films. Table 4 discusses the different materials and their contact angle below.

***Table 4.** The angle of contact of different surfaces*

Materials name	Contact angle, °	Materials name	Contact angle, °
Hepta decafluorode cyltrim ethoxy silane	115	Diamond	87
(Heptafluoroisopropoxy) propyltrichlorosilane	109-111	Graphite	86
Poly(tetrafluoroethylene)	108-111	Talc	50-55
Poly(propylene)	108	Steel	70-75
Octadecyldimethylchlorosilane	110	Gold, typical (see gold, clean)	66
Poly(ethylene)	88-103	Kaolin	42-46
Poly(styrene)	94	Platinum	40
Poly(chlorotrifluoroethylene)	90	Silicon nitride	28-30
Human skin	75-90	Gold, clean	<10

Different properties and contents of the test materials of ZrO_2

This work assesses the water sorption/solubility, hardness, elastic modulus, and transverse strength of zirconium oxide nanoparticles (nano-ZrO_2) added to heat-cured poly methyl meth-acrylate (PMMA). Based on the amount of nano Added to heat-cured PMMA, the specimens were

split into four groups: group 1 received 5% nano-ZrO_2, group 2 received 10 % nano-ZrO_2, group 3 received 20 % nano-ZrO_2, and Group 4 received controls [64]. Table 5 shows the results of the specimens with different quantities of ZrO_2 added in PMMC.

Table 5. *Results of the tested specimens*

Sample	Transverse strength, MPa	Modulus of elasticity	Microhardness values, g
ZrO_2(5 %) + PMMC	0.739	0.481	0.529
ZrO_2(10 %) + PMMC	0.579	0.684	0.029
ZrO_2(20 %) + PMMC	0.853	0.353	0.009
ZrO_2(RC) + PMMC	0.579	0.529	0.353

The magnetron sputtering method will be used in this work to deposit zirconium oxide films at argon partial pressures of 45, 55, 62 and 67 %. This work explores the impact of argon partial pressure on the optical, wettability, and structural characteristics of zirconium oxide coatings [65,66]. Table 6 shows the variation of pressure with different film parameters.

Table 6. ZrO_2 thin film parameters (properties) calculated on the basis of variation in pressure

Change in pressure, %	Band gap, eV	Index of refraction	Thickness, nm	Surface roughness, nm
45	4.28	1.53	433	1.75
55	4.34	1.53	408	1.42
62	4.44	1.52	391	1.24
67	4.46	1.52	385	1.07

Properties of ZrO_2 using the low-temperature atomic layer deposition

This study characterized ZrO_2 films made using the atomic layer deposition technique as the encapsulating layer for organic electronics devices. The impacts of oxidants such as water (H_2O) and ozone (O_3), as well as tetrakis(dimethylamido) zirconium(IV) growth temperature, were investigated. The X-ray diffraction study shows that the 80 nm-thick films formed at 80 °C had a significantly lower amorphous nature than those grown at 140 and 200 °C. SEM analysis showed that the films' crystallinity significantly impacts the surface morphology [67]. The water vapour transmission rate of the 80 nm thick ZrO_2 films may be reduced from 3.74103 to 6.09104 g m^{-2} day^{-1} (using 80° H_2O as the oxidant) in a controlled environment with 20 °C and 60 % relative humidity. Moreover, the brightness decay time of the organic light-emitting diodes combined with ZrO_2 films produced from O_3 at 80 °C was dramatically changed without causing harm. This was ascribed to the enhanced barrier property of the lower-temperature ZrO_2 layer to the almost homogeneous microscopic surface and amorphous microscopic bulk. The average height of crystallites in H_2O and O_3-based ZrO_2 films deposited at various temperatures is shown in Table 7 [68].

Table 7. Low-temperature ZrO_2 film deposition range

Temperature of deposition, °C	Height of H_2O based ZrO_2 film, nm	Height of O_3-based ZrO_2 film based on O_3, nm
80	8.4±0.13	3.8±0.1
140	14.7±0.2	10.7±0.1
200	21.2±0.2	15.2±0.2

Conclusion and future scope

First of all, numerous methodological angles are presented in this review. This article aims to promote an understanding of the usage of several types of coatings techniques of zirconium oxide, wear-reduction procedures, advantages, disadvantages, and properties of zirconium oxide used for different substrates and quantities. If the coatings process and techniques are increased, the

membrane's sealing will also be improved, and it will have less porosity and better corrosion resistance. Aerospace, ground turbines, car production, ceramics and glass, printing, pulp and paper, metallurgy, medical, nuclear power, cement plant spray, and waste treatment are just a few industries that frequently use anti-corrosion coatings. Chemical/physical vapour deposition (CVD/PVD), micro-arc oxidation (MAO), electrode position (for example, galvanic coating), electrophoretic deposition (EPD), sol-gel, and various thermal sputtering procedures (for example, HVOF, plasma, cold, thermal, and arc sputtering) are the most effective thermal sputtering techniques. Since the teaching process employs various strategies to position certain items on the website, selecting the appropriate materials is crucial to achieving a good process. Heat can be used in some procedures to transform food into liquids and semi-solids as clumps, droplets, and particles.

In conclusion, thermal operations such as various types of thermal spraying are made more efficient by using high-temperature and high-speed plasma jets. This method enables the processing of the raw material at low temperatures and fast speeds while removing the detrimental impacts of the high melting points of ceramics and superalloys. In these situations, layers that might be hundreds of microns thick are created. Depending on the process, the layered microstructure may contain oxide and carbide inclusions and porosity. The only applications for deposition coatings based on evaporation technology are the coating of equipment and the protection of sliding mechanical parts. These thin films have good corrosion/wear resistance. Biomaterials for use in bone implants and medical equipment usually use micro-arc oxidation, a high conversion of randomization. The metals Al, Ti, Zr, Hf, V, and Nb are frequently used as substrates for valves. Strong substrate/layer adhesion and porosity are provided by the coating created by MAO during bone development, which is crucial for biomaterial coatings. According to the pace or duration of plant degradation, The porous microstructure also improves corrosion resistance and makes it easier to estimate plant longevity using engineering models. Another tested substance, sol-gel, has numerous nutritional advantages, and since an aqueous solution serves as the process' carrier, the process' quality is unaffected by the geometry's intricacy. Sol-gel deposits are utilized as a sealant to strengthen the corrosion resistance of porous substrates and coatings. Despite the versatility and layering capabilities of the sol-gel technique, the fabrication could be faster and more efficient. Another type of water purification technology uses electrochemical processes that rely on the charge difference between the chemical cell's anode and cathode.

Superhydrophobic coatings offer much potential for industrial applications; therefore, they're getting much attention. Because of its special characteristics, which include self-cleaning, antifogging, drag reduction, corrosion resistance, anti-icing, and ice-phobic capabilities, it is anticipated that their fields of application will grow in the future. This study thoroughly examines super hydrophobic coatings in the application domains of vehicles, marine, aircraft, solar energy, and architecture buildings based on the requirement for significant functionalities and performance conformities. The thickness of zirconium oxide sheets reduces from 433 to 385 nm with increasing argon partial pressure. The band gap rises from 4.28 to 4.46 eV as the thickness of the zirconium oxide sheet decreases, yet the gearbox increases. The coats of zirconium oxide dissipate water with a 45% partial argon pressure and a maximum contact angle of 101°. The maximum aniline contact angle for zirconium oxide sheets is 52° at a partial pressure of 67 % argon. The paper overviews the various operating materials and the importance of zirconium oxide in hydrophobic coating for ultra hydrophobic applications.

References

1. G. Frommeyer, G. Wassermann, Anomalous properties of in situ-produced silver copper composite wires I. Electrical conductivity, *Physica Status Solidi* **27** (1975) 99-105. https://doi.org/10.1002/pssa.2210270112
2. H. Ibrahim, A. R. Jahadakbar, A. Dehghan, N. S. Moghaddam, A. Amerinatanzi, M. Elahinia, In vitro corrosion assessment of additively manufactured porous NiTi structures for bone fixation applications, *Metals* **8** (2018) 164. https://doi.org/10.3390/met8030164
3. S. Mirzababaei, P. Filip, Impact of humidity on wear of automotive friction materials, *Wear* **376** (2017) 717-726. https://doi.org/10.1016/j.wear.2017.02.020
4. B. Bhushan, B. K. Gupta, *Handbook of Tribology: Materials, coatings, and surface treatments.* United States, 1991. https://www.osti.gov/biblio/441774
5. A. Dehghanghadikolaei, B. Mohammadian, N. Namdari, B. Fotovvatiet, Abrasive machining techniques for biomedical device applications*, Journal of Material Science* **5(1)** (2018) 555654. https://juniperpublishers.com/jojms/pdf/JOJMS.MS.ID.555654.pdf
6. L. J. Casarett, M. O. Amdur, C. D. Klaassen, J. Doull (Editor) *Casarett and Doull's Toxicology: The Basic Science of Poisons, 5th Edition.* McGraw-Hill, New York, USA, 1996. ISBN 978-0071054768
7. M. R. Thakare, J. A. Wharton, R. J. K. Wood, C. Menger, Exposure effects of alkaline drilling fluid on the microscale abrasion-corrosion of WC-based hard metals, *Wear **263*** (2007) 125-136. https://doi.org/10.1016/j.wear.2006.12.047
8. J. T. DeMasi-Marcin, D. K. Gupta, Protective coatings in the gas turbine engine, *Surface and Coatings Technology* **68** (1994) 1-9. https://doi.org/10.1016/0257-8972(94)90129-5
9. R. K. Annavarapu, S. Kim, M. Wang, A. J. Hart, H. Sojoudi, Explaining evaporation-triggered wetting transition using local force balance model and contact line-fraction, *Scientific Reports* **9** (2019) 405. https://doi.org/10.1038/s41598-018-37093-6
10. N. Gao, Y. Yan, Modeling superhydrophobic contact angles and wetting transition,*Journal of Bionic Engineering* **6** (2009) 335-340. https://doi.org/10.1016/S1672-6529(08)60135-3
11. N. Kumar, V. K. Choubey, Comparative evaluation of oxidation resistance of detonation gun-sprayed Al2O3-40% TiO2 coating on nickel-based super alloys at 800 °C and 900 °C, *High Temperature Corrosion of Materials* **99** (2023) 359-373. https://doi.org/10.1007/s11085-023-10157-3
12. N. Kumar, V. K. Choubey, Effect of WC-Co and 86WC-10Co-4Cr coatings on type-II hot corrosion behavior & microstructure characteristics at 650 °C, *Surface and Coatings Technology* **469** (2023) 129812. https://doi.org/10.1016/j.surfcoat.2023.129812
13. K. K. Gleason, Overview of chemically vapor deposited (CVD) polymers, *CVD Polymers: Fabrication of Organic Surfaces and Devices* (2015) 1-11. https://doi.org/10.1002/9783527690275.ch1
14. N. Kumar, V. K. Choubey, Recent trends in coating processes on various AISI steel substrates, *Journal of Materials Science* **59** (2023) 1-28. https://doi.org/10.1007/s10853-023-09239-z
15. N. Kumar, V. K. Choubey, Experimental investigation on hot corrosion, oxidation and microstructure of WC based cermet HVOF coating, *High Temperature Corrosion of Materials* **101** (2023) 1-20. https://doi.org/10.1007/s11085-023-10179-x
16. Y. Li, D. Mann, M. Rolandi, W. Kim, A. Ural, S. Hung, A. Javey, J. Cao, D. Wang, E. Yenilmez, Q. Wang, J. F. Gibbons,Y . Nishi, H. Dai, Preferential growth of semiconducting single-walled carbon nanotubes by a plasma enhanced CVD method, *Nano Letters* **4** (2004) 317-321. https://doi.org/10.1021/nl035097c
17. B. Fotovvati, A. Dehghanghadikolaei, N. Namdari, Laser-Assisted coating techniques and surface modifications: A short review, *Particulate Science and Technology* **39** (2021) 738-747. https://doi.org/10.1080/02726351.2020.1812778

18. B. Fotovvati, S. F. Wayne, G. Lewis, E. Asadi, A review on melt-pool characteristics in laser welding of metals, *Advances in Materials Science and Engineering* **2018** (2018) 4920718. https://doi.org/10.1155/2018/4920718
19. A. Dehghanghadikolaei, J. Ansary, R. Ghoreishi, Sol-gel process applications: A mini-review, *Proceedings of the Nature Research Society* **2** (2018) 02008-02029. https://doi.org/10.11605/j.pnrs.201802008
20. L. Pawlowski, *The science and engineering of thermal spray coatings*. John Wiley & Sons, West Sussex, England, 2008, p.85.
21. R. J. Davis, ed. *Handbook of Thermal Spray Technology*. ASM international, 2004.
22. A. Rabiei, D. R. Mumm, J. W. Hutchinson, R. Schweinfest, M. Ruhle, A. G. Evans, Microstructure, deformation and cracking characteristics of thermal spray ferrous coatings, *Materials Science and Engineering* **269** (1999) 152-165. https://doi.org/10.1016/S0921-5093(99)00132-X
23. J. Karthikeyan, C. C. Berndt, J. Tikkanen, S. Reddy, H. Herman, Plasma spray synthesis of nanomaterial powders and deposits, *Materials Science and Engineering*: **238** (1997) 275-286. https://doi.org/10.1016/S0921-5093(96)10568-2
24. N. Kumar, V. K. Choubey, Investigation of microstructure and Isothermal oxidation resistance of cermet HVOF coated on AISI316L at 900°C, *Results in Surfaces and Interfaces* **14** (2024) 100173. https://doi.org/10.1016/j.rsurfi.2023.100173
25. N. K Mishra, N. Kumar, S. B. Mishra, Hot Corrosion Behaviour of Detonation Gun Sprayed Al2O3-40TiO2 Coating on Nickel Based Superalloys at 900° C, *Indian Journal of Materials Science* **2014** (2014) 453607. https://doi.org/10.1155/2014/453607
26. E. Petrovicova, L. S. Schadler, Thermal spraying of polymers, *International Materials Review* **47** (2002) 169-190. https://doi.org/10.1179/095066002225006566
27. S. K. Nemani, R.K. Annavarapu, B. Mohammadian, A. Raiyan, J. Heil, M. A. Haque, A. Abdelaal, H. Sojoudi, Surface modification of polymers: methods and applications, *Advanced Materials Interfaces* **5** (2018) 1801247. https://doi.org/10.1002/admi.201801247
28. L. C. Betancourt-Dougherty, R. W. Smith, Effects of load and sliding speed on the wear behavior of plasma sprayed TiCNiCrBSi coatings, *Wear* **217** (1998) 147-154. https://doi.org/10.1016/S0043-1648(97)00212-3
29. N. P. Padture, M.Gell, E. H. Jordan, Thermal barrier coatings for gas-turbine engine applications, *Science* **296** (2002) 280-284. https://doi.org/10.1126/science.1068609
30. V. K. Champagne, The cold materials spray deposition process,*Woodhead Publishing Series in Metals and Surface Engineering* **5** (2007). https://doi.org/10.1533/9781845693787
31. C. J. Li, H. T. Wang, Q. Zhang, G. J. Yang, W. Y. Li, H. L.Liao, Influence of spray materials and their surface oxidation on the critical velocity in cold spraying, *Journal of Thermal Spray Technology* **19** (2010) 95-101. https://doi.org/10.1007/s11666-009-9427-x
32. W. Y. Li, H. Liao, C. J. Li, H.S.Bang, C. Coddet, Numerical simulation of deformation behavior of Al particles impacting on Al substrate and effect of surface oxide films on interfacial bonding in cold spraying, *Applied Surface Science* **253** (2007) 5084-509. https://doi.org/10.1016/j.apsusc.2006.11.020
33. Y. C. Tsui, C. Doyle, T. W. Clyne, Plasma sprayed hydroxyapatite coatings on titanium substrates Part 1: Mechanical properties and residual stress levels, *Biomaterials* **19** (1998) 2015-2029. https://doi.org/10.1016/S0142-9612(98)00103-3
34. T. Schmidt, H. Assadi, F. Gartner, H. Richter, T.Stoltenhoff, H.Kreye, T.Klassen, From particle acceleration to impact and bonding in cold spraying, *Journal of Thermal Spray Technology* **18** (2009) 794-808. https://doi.org/10.1007/s11666-009-9357-7

35. J. Kawakita, H. Katanoda, M. Watanabe, K. Yokoyama, S. Kuroda, Warm Spraying: An improved spray process to deposit novel coatings, *Surface and Coatings Technology* **202** (2008) 4369-4373. https://doi.org/10.1016/j.surfcoat.2008.04.011
36. I. Gedzevicius, A.V. Valiulis, Analysis of wire arc spraying process variables on coatings properties, *Journal of Materials Processing Technology* **175** (2006) 206-211. https://doi.org/10.1016/j.jmatprotec.2005.04.019
37. J. Kawakita, N. Maruyama, S. Kuroda, S. Hiromoto, A. Yamamoto, Fabrication and mechanical properties of composite structure by warm spraying of Zr-base metallic glass, *Materials Transactions* **49** (2008) 317-323. https://doi.org/10.2320/matertrans.T-MRA2007882
38. Y. C. Tsui, C. Doyle, T. W. Clyne, Plasma sprayed hydroxyapatite coatings on titanium substrates Part 2: optimisation of coating, *Biomaterials* **19** (1998) 2031-2043. https://doi.org/10.1016/S0142-9612(98)00104-5
39. K. H. Kim, M. Watanabe, J. Kawakita, S. Kuroda, Grain refinement in a single titanium powder particle impacted at high velocity, *Scripta Materialia* **59** (2008) 768-771. https://doi.org/10.1016/j.scriptamat.2008.06.020
40. P. Chivavibul, M. Watanabe, S. Kuroda, J. Kawakita, M. Komatsu, K. Sato, J. Kitamura, Development of WC-Co coatings deposited by warm spray process, *Journal of Thermal Spray Technology* **17** (2008) 750-756. https://doi.org/10.1007/s11666-008-9271-4
41. P. Skarvelis, G. D. Papadimitriou, Plasma transferred arc composite coatings with self lubricating properties, based on Fe and Ti sulfides: Microstructure and tribological behavior, *Surface and Coatings Technology* **203** (2009) 1384-1394. https://doi.org/10.1016/j.surfcoat.2008.11.010
42. T. Watanabe, T. Sato, A. Nezu, Electrode phenomena investigation of wire arc spraying for preparation of Ti-Al intermetallic compounds, *Thin Solid Films* **407** (2002) 98-103. https://doi.org/10.1016/S0040-6090(02)00019-6
43. H. Sojoudi, S. Kim, H. Zhao, R.K. Annavarapu, D. Mariappan, A. J. Hart, G. H. McKinley, K. K. Gleason, Stable wettability control of nanoporous microstructures by iCVD coating of carbon nanotubes, *ACS Applied Materials & Interfaces* **9** (2017) 43287-43299. https://doi.org/10.1021/acsami.7b13713
44. S. K. Nemani, H. Sojoudi, Barrier performance of CVD graphene films using a facile P_3HT thin film optical transmission test, *Journal of Nanomaterials* **2018** (2018) 681432. https://doi.org/10.1155/2018/9681432
45. A. Joukar, J. Mehta, D. Marks, V. K. Goel, Lumbar-sacral destruction fixation biomechanics: a finite element study, *The Spine Journal* **17** (2017) S335. https://doi.org/10.1016/j.spinee.2017.10.062
46. A. Moridi, S. M. Hassani-Gangaraj ,M. Guagliano, M. Dao, Cold spray coating: review of material systems and future perspectives, *Surface Engineering* **30** (2014) 369-395. https://doi.org/10.1179/1743294414Y.0000000270
47. A. Sabard, H. L. de Villiers Lovelock, T. Hussain, Microstructural evolution in solution heat treatment of gas-atomized Al alloy (7075) powder for cold spray, *Journal of Thermal Spray Technology* **27** (2018) 145-158. https://doi.org/10.1007/s11666-017-0662-2
48. S. W. Dean, J. K. Potte, R. A. Yetter, T. J. Eden, V. K. Champegne, M. Trexler, Energetic intermetallic materials formed by cold spray, *Intermetallics* **43** (2013) 121-130. https://doi.org/10.1016/j.intermet.2013.07.019
49. W. Bao, Z. Deng, S. Zhang, Z. Ji, H. Zhang, Next-generation composite coating system: nanocoating, *Frontiers in Materials* **6** (2019) 456324. https://doi.org/10.3389/fmats.2019.00072
50. Q. Zhu, M. H. Chua, P. J. Ong, J. J. C. Lee, K. L. O. Chin, S. Wang, D. Kai, R. Ji, J. Kong, Z. Dong, J. Xu, X. J. Loh, Recent advances in nanotechnology-based functional coatings for the built

environment, *Materials Today Advances* **15** (2022) 100270. https://doi.org/10.1016/j.mtadv.2022.100270
51. Y. Bai, H. Zhang, Y. Shao, H. Zhang, J. Zhu, Recent progresses of superhydrophobic coatings in different application fields: An overview, *Coatings* **11** (2021) 116. https://doi.org/10.3390/coatings11020116
52. I. Das, G. De, Zirconia based superhydrophobic coatings on cotton fabrics exhibiting excellent durability for versatile use, *Scientific Reports* **5** (2015) 18503. https://doi.org/10.1038/srep18503
53. S. Venkataraj, J. Geurts, H. Weis, O. Kappertz, W. K. Njoroge, R. Jayavel, M. Wuttig, Structural and optical properties of thin lead oxide films produced by reactive direct current magnetron sputtering, *Journal of Vacuum Science & Technology A* **19** (2001) 2870-2878. https://doi.org/10.1116/1.1410948
54. P. Gao,L. J. Meng, M. P. dos Santos, V. Teixeira, M. Andritschky, Characterisation of ZrO_2 films prepared by RF reactive sputtering at different O_2 concentrations in the sputtering gases, *Vacuum* **56** (2000) 143-148. https://doi.org/10.1016/S0042-207X(99)00199-2
55. C. M. Lopez, N. A. Suvorova, E. A. Irene, A. A. Suvorova, M. Saunders, ZrO2 film interfaces with Si and SiO2, *Journal of Applied Physics* **98** (2005) 033506. https://doi.org/10.1063/1.1994938
56. H. H. Zhang, C. Y. Ma, Q. Y. Zhang, Scaling behavior and structure transition of ZrO_2 films deposited by RF magnetron sputtering, *Vacuum* **83** (2009) 1311-1316. https://doi.org/10.1016/j.vacuum.2009.04.041
57. K. Khojier, H. Savaloni, F. Jafari, Structural, electrical, and decorative properties of sputtered zirconium thin films during post-annealing process, *Journal of Theoretical and Applied Physics* **7** (2013) 55. http://www.jtaphys.com/content/7/1/55
58. S. G. Wu, H. Y. Zhang, G. L. Tian, Z. L. Xia, J. D. Shao, Z. X. Fan, Y2O3 stabilized ZrO2 thin films deposited by electron-beam evaporation: Optical properties, structure and residual stresses, *Vacuum* **83** (2008) 366-371. https://doi.org/10.1016/j.apsusc.2006.02.044
59. M. Matsuoka, S. Isotani, J. F. D. Chubaci, S. Miyake, Y. Setsuhara, K. Ogata, N. Kuratani, Influence of ion energy and arrival rate on x-ray crystallographic properties of thin ZrOx films prepared on Si (111) substrate by ion-beam assisted deposition, *Journal of Applied Physics* **88** (2000) 3773-3775. https://doi.org/10.1063/1.1286108
60. W. J. Qi, R. Nieh, H. H. Lee, L. Kang , Y. Jeon , J. C. Lee, Electrical and reliability characteristics of ZrO2 deposited directly on Si for gate dielectric application, *Applied Physics Letters* **77** (2000) 3269-3271. https://doi.org/10.1063/1.1326482
61. S. W. Nam, J. H. Yoo, H. Y. Kim, S. K. Kang, D. H. Ko, C. W. Yang, H. J. Lee, M. H. Cho, J. H. Ku, Study of ZrO_2 thin films for gate oxide applications, *Journal of Vacuum Science & Technology A* **19** (2001)172-1724. https://doi.org/10.1116/1.1351802
62. J. Koo, Y. Kim, H. Jeon, ZrO2 Gate Dielectric Deposited by Plasma-Enhanced Atomic Layer Deposition Method, *Japanese Journal of Applied Physics* **41** (2002) 3043. https://doi.org/10.1143/JJAP.41.3043
63. T. Suntola, Atomic Layer Epitaxy, *Thin Solid Films* **216** (1992) 84-89. https://doi.org/10.1016/0040-6090(92)90874-B
64. R. G. Gordon, J. Becker, D. Hausmann, S. Suh, Vapor deposition of metal oxides and silicates: Possible gate insulators for future microelectronics, *Chemistry of Materials* **13** (2001) 2463-2464. https://doi.org/10.1021/cm010145k
65. J. Gottmann, E. W. Kreutz, Pulsed laser deposition of alumina and zirconia thin films on polymers and glass as optical and protective coatings, *Surface and Coatings Technology* **116** (1999) 1189-1194. https://doi.org/10.1016/S0257-8972(99)00191-7

66. D. A. Neumayer, E. Cartier, Materials characterization of ZrO2-SiO2 and HfO2-SiO2 binary oxides deposited by chemical solution deposition, *Journal of Applied Physics* **90** (2001) 1801-1808. https://doi.org/10.1063/1.1382851
67. S. Manakasettharn, T .H. Hsu, G. Myhre, S. Pau, J. A. Taylor, T. Krupenkin, Transparent and superhydrophobic Ta_2O_5 nanostructured thin films, *Optical Materials Express* **2(2)** (2012) 214-221. https://doi.org/10.1364/OME.2.000214
68. D. Tulli, P. Mazumder, D. Infante, A. Carrilero, V. Pruneri, Superhydrophobic sputtered Al_2O_3 coating films with high transparencym, *2013 Conference on Lasers & Electro-Optics Europe & International Quantum Electronics Conference CLEO EUROPE/EQEC. IEEE,2013 1-1.* https://doi.org/10.1109/CLEOE-IQEC.2013.6800938

J. Electrochem. Sci. Eng. **14(4)** (2024) 459-472; http://dx.doi.org/10.5599/jese.2324

Open Access : : ISSN 1847-9286
www.jESE-online.org

Review paper

Behaviour of thermally sprayed coating for hot corrosion applications

Md Sarfaraz Alam[1,✉], Naveen Kumar[2] and Anil Kumar Das[3]

[1]*Department of Mechanical Engineering, Sershah Engineering College Sasaram, Bihar 821113, India*
[2]*Department of Mechanical Engineering, United College of Engineering & Research, Prayagraj, Uttar Pradesh (211010), India*
[3]*Department of Mechanical Engineering, National Institute of Technology Patna, Bihar 800005, India*

Corresponding authors: ✉ *mda.phd19.me@nitp.ac.In*

Received: March 16, 2024; Accepted: April 24, 2024; Published: June 16, 2024

Abstract

As modern air engines' working temperatures are increasing, materials and coatings' hot corrosion resistance characteristics gain significant attention. Hot corrosion is a type of degradation at high temperatures that involves oxidizing or sulphidation of the substrate behind a layer of salt melt deposit, which either causes the development of a thick layer of sulphide scale or the penetration of sulphur via grain boundaries into the matrix to a deeper depth. It may notably change the microstructure, phase composition, and characteristics of the thermally sprayed coating. In recent years, thermally sprayed cermet coatings on steel have been more well-liked as a possible method for enhancing hot corrosion resistance. This review paper qualitatively summarizes the recent development of thermal sprayed coatings to improve hot corrosion performance.

Keywords

Sulphidation; tribology; wear resistance; cermet coatings

Introduction

Hot corrosion is a type of degradation at high temperatures that involves oxidizing or sulfidation of the substrate behind a layer of salt melt deposit, which either causes the development of a thick layer of sulphide scale or the penetration of sulphur via grain boundaries into the matrix to a deeper depth. The typical morphology of hot corrosion products consists of a low-chromium metal matrix, a dense, porous oxide layer, and chromium-rich sulphides inside the oxides. The consensus among specialists is that initiating a hot-corrosion attack requires liquid Na sulphate. Generally, hot corrosion attack occurs between 800 and 950 °C, though this varies depending on the alloy.

If the melting point for salt deposits is at a lower temperature but the dew point is at higher temperatures, the corrosion is referred to as type I hot corrosion [1]. On the other hand, type II hot

corrosion happens at lower temperatures (generally from 670 to 750 °C). Type II hot corrosion behind a protective layer with minimal to no interior attack indicates a pitting attack [2].

Some metals, such as zirconium, titanium, chromium, and others, form shielding nitride scales when exposed to nitrogen-rich environments. Carburization and decarburization problems that weaken or embrittle the component occasionally occur in carbon dioxide and carbon monoxide environments.

When fireside boiler tubes in coal-fired steam-generating plants started to deteriorate, high-temperature corrosion was first identified as a severe issue in the 1940s. Since then, fluidized bed combustion, gas turbines, I. C. engines, boilers, and industrial waste incinerators have all experienced the issue. In the late 1960s, turbine makers and users learned about hot corrosion due to the severe corrosive assault that occurred in the engines of rescue planes and helicopters operating over and near seawater during the Vietnam War [3,4]. The primary factor contributing to hot corrosion is the breakdown of ash and fuel compounds, which include Na, S, V and Cl, which are present in burning coal or fuel oil. When marine atmospheres are contaminated with NaCl, these pollutants may occasionally be consumed from the service environment. It is well acknowledged that hot corrosion requires condensed alkali metal salts, especially Na_2SO_4 [5]. A typical high-temperature corrosion promoter in these applications, besides Na_2SO_4, is V_2O_5.

In most cases, using these low-grade fuels is acceptable due to the significant expense of eliminating these contaminants. According to research, the most frequent salt buildup in boiler superheaters is sodium vanadyl vanadate (Na_2O x V_2O_4 x $5V_2O_5$), which fuses at a comparably lesser temperature of 550 °C [6]. Na_2SO_4, V_2O_5, and $Na_2V_2O_6$ are also anticipated to be the main species in salt deposits accumulating on gas turbine surfaces [7].

Due to molten salts in the fuel, such as KCl, $NaVO_3$, Na_2SO_4, V_2O_5, and NaCl, hot corrosion is the primary cause of failure in gas turbines [8-11]. This corrosion causes surface spalling by accelerating the oxidation and sulphidation of thermo-resistant materials. When contaminants like sulphur and/or chlorine are present in an oxidizing atmosphere, the rate of attack frequently increases in the sequence as first oxidation only, after that internal sulphidation, then after internal chlorination, then (sulphate salts) hot corrosion then (sulphate and chloride salts) hot corrosion. To compare other, more aggressive kinds of corrosion, oxidation in air or O_2 is typically employed as a baseline. Molten salt deposits can bring on rapid oxidation and hot corrosion. Internal chlorides, oxides, and/or internal sulphides are examples of corrosion products [12-14]. Gas turbine parts that work in the heated gas stream, such as vanes, blades and combustor cans, are exposed to severe corrosive conditions [15]. These types of corrosion can significantly reduce the lifespan of gas turbine parts. Type I hot corrosion (sulphidation and internal damage) takes place between 800 and 900 °C, whereas Type II hot corrosion (pitting) takes place between 600 and 750 °C [16]. Hot corrosion damage can be divided into two phases. First, in the incubation phase, during which the developed protective scale may be heeled by materials in the underlying substrate, metal loss rate is low. Second, in the propagation phase, during which the protective scale has been irreparably damaged, sulphides and oxides advance quickly into the surface of the substrate, and the metal loss rate is high [17].

Residual oil (fuel) is used in energy-generating systems, which is widely recognized due to the exhaustion of high-quality fuels and for financial reasons. Salt contamination from entrained brine and contaminants such as sodium, vanadium, and sulphur are present in residual fuel oil. The combustion system reacts with sodium and sulphur to produce Na_2SO_4 (melting point 884 °C). Vanadium and oxygen combine to generate the oxide V_2O_5 (melting point 670 °C) during fuel combustion. At the working temperatures of a gas turbine, V_2O_5 is a liquid in energy-generating

systems. These substances (also referred to as ash) cause rapid oxidation (also known as hot corrosion) and accumulate on the surface of the materials.

Hot corrosion is anticipated to be a concern when contemplating coal-gasification procedures since the feedstock also contains a significant quantity of salts, and the gas environment often contains sulphur and chloride compounds and low oxygen activity [18].

Gas turbines typically operate at relatively high temperatures. This trend is anticipated to continue when cooling technologies and new materials are developed for gas turbine engines of the next generation. Hot corrosion requires particular consideration due to the coupling of such elevated temperatures with an aviation condition that contains pollutants, including sodium, vanadium, sulphur, and several halides [7].

Therefore, power plants are one of the key industries affected by severe corrosion issues that cause significant losses. For example, the boiler and turbine thermal efficiency is affected by the creep and corrosion resistance of boiler and turbine elements, which limits the steam/gas temperature. The rate of power production is then lowered as a result of the decreased thermal efficiency [19].

Iron base alloys containing significant amounts of chromium and nickel are most frequently used in coal-fired power plants and oil refineries. The use of these alloys often results in their corrosion due to the attack of gaseous elements such as O_2, H_2S, SO_2, CO, and CO_2, as well as the deposition of meltable ash or salts. Numerous researchers have examined the corrosion caused by the deposit at the fireside. Alkali sulphates, which accumulate on the surface of alloy components and promote hot corrosion degradation because of less melting eutectics between $Fe_2(SO_4)_3$ and Na_2SO_4 and or K_2SO_4 or both, happen at relatively low temperatures [20-23], are the most prevalent forms of sulphates. Studies on cobalt, nickel, and Fe base alloys have shown that hot corrosion may initiate as low as 550 °C. Thus, the creation of low melting eutectics such as Na_2SO_4 + $CoSO_4$ (565 °C) and Na_2SO_4 + $NiSO_4$ (667 °C) appears to be the main cause.

Most of the time, high-temperature alloys subjected to corrosion displayed oxidation and sulphidation degradation. Type II hot corrosion is uncommon in aero engines since the blades are often operated at higher temperatures [24]. On the other hand, industrial and marine gas turbines operating at low temperatures may experience type II high-temperature corrosion at moderate temperatures.

High-temperature corrosion occurs when molten salt is applied to alloys and metals. In boilers that burn coal, corrosion arises at high temperatures due to low-emission combustion and low-quality fuel. When low-quality fuels burn, they release ash due to the presence of sulphur, salt, vanadium, chlorine, and other contaminants. On boiler parts, fly ash may create a layer of molten salt. Severe high-temperature corrosion is caused by the complex salt deposit's attack on the developed protective oxide scale of the material [25-28].

Research progress in hot corrosion

Guo *et al.* [29] deposited an Al and Cr gradient NiCoCrAlYSiB coatings on to Ni based superalloy substrate and oxidised them at 900 °C for 20 hours in 0.5 mg cm^{-2} of 20 % K_2SO_4 80 % Na_2SO_4 salt mixture to examine the effects of Al and Cr on the hot corrosion of coatings. XRD and EDS results show that there are only the alumina formed on the NiCoCrAlYSiB coatings, so the basic fluxing of Al_2O_3 occurred, which caused an accelerated hot corrosion after 10 h. The gradient coatings resulted from Al_2O_3 and Cr_2O_3 formed in the first stage of hot corrosion. Na_2SO_4's oxygen ion activity is lowered by Cr_2O_3, which reacts with Al_2O_3 more readily than Al_2O_3, protecting Al_2O_3. Similar to

oxidation kinetics, gradient coatings show hot corrosion kinetics due to the development of continuous and protective layer of Cr_2O_3 and Al_2O_3.

The hot corrosion and oxidation behaviour of the Ni and Fe-based superalloys Superni75 and Superfer 800H were investigated by Sidhu *et al.* [30]. The superalloy samples underwent cycle conditions, including exposure to air and a corrosive molten salt environment (75 % Na_2SO_4 + 25 % NaCl) at 800 °C. Superni75, a superalloy based on nickel, is more resistant to oxidation and heat corrosion than Superfer800H, a superalloy based on iron, in the given environment at 800 °C. Due to its tendency to produce protective spinel and chromium-nickel oxides, Superni 75 has performed better in both circumstances.

In a related investigation, Sidhu *et al.* [31] came to the conclusion that the oxides of the coatings' active components, which developed on the scale's surface and at the edges of Ni and W-rich splats, were responsible for the hot corrosion and resistance against oxidation of WC-NiCrFeSiB coatings. Developed oxides served as barriers to prevent the corrosive species from diffusing and penetrating through the coatings.

After being exposed to 950 °C for 20 hours, the DZ68 superalloy surface formed a protective scale, according to Liu *et al.* [32]. The procedure improved the alloy's first incubation period at 900 °C in the slurry. According to their research, it may provide a special defence against corrosive salt and dramatically slow down the rate of deterioration.

Liu *et al.* [33] examined the effects of the hot corrosion behaviours of the M38G superalloy in a combination of Na_2SO_4-NaCl salt melts. Results indicated that the treatment could, in combination with melts at 850 and 800 °C, somewhat boost the M38G alloy's resistance to hot corrosion. The protection provided by the oxide layer decreased with temperature, but the treatment at 875 °C had no effect on the hot corrosion of the M38G superalloy.

Kamal *et al.* [34] investigated the oxidation and hot corrosion behaviour of Ni-based superalloys exposed to ambient air and a corrosive fused salt environment (Na_2SO_4 - 60 % V_2O_5) at 900 °C. Weight change observation and calculation on the superalloys during the entire cycle are used to develop hot corrosion and oxidation kinetics. The enhanced hot corrosion and oxidation resistance of Superni75 was attributed to the scale's richness in NiO, Cr_2O_3, and spinel $NiCr_2O_4$. On the other hand, non-protective iron oxides and nickel and iron sulphides cause Superfer800H to have a comparatively lower level of hot corrosion resistance. The parabolic rate constants computed for these materials indicate that the hot corrosion rate for superalloys is lowest in ambient air with respect to a fused salt condition.

According to Wang *et al.* [35], The Nb solid solution / Nb_5Si_3 alloys oxidised more quickly and left the porous surface when NaCl and Na_2SO_4 were present.

According to the research of Sidhu *et al.* [36], WC-Co and WC-CoCr coatings on steel alloys T22 and T91 proved to be corrosion resistant in the boiler's superheater area after ten cycles (each lasting 100 hours) at 900 °C. The following order of coating corrosion resistance demonstrations was observed: T22 coating with 86WC-10Co4Cr > T22 coating with WC-17Co > T91 coating with WC-10Co4Cr > T91 coating with WC-17Co

The Cr_3C_2-NiCrMoNbAl coating made by HVOF on P91 steel and its hot corrosion behaviour was described by Zhou *et al.* [37]. Compared to P91 steel, the Cr_3C_2-25(NiCr) coating showed better corrosion resistance at 650 °C.

According to Qiao *et al.* [38], Nb-Si-Ti alloy and its silicide covering were subjected to a heated corrosion process that was exacerbated by NaCl.

Wei *et al.* [39] deposited the Mo-62Si-5B alloy using the SPS method. When an alloy is coated with molten salts, more significant mass changes occur compared to when exposed to dry air. The alloy's mass changes in the Na_2SO_4+NaCl combination and Na_2SO_4 following 100 hours of hot corrosion at 900 °C are 0. 50 and 0. 24 mg cm^{-2}. There is a loss of mass when SiO_2 is created because more MoO_3 evaporates than is gained in weight. Most loose oxide scales on the alloy are made up of SiO_2 and amorphous borosilicate. The oxide scales become porous due to the mixture of Na_2SO_4 and NaCl, accelerating the oxidation process.

The corrosion behaviour of WC-CoCr coatings by HVOF spraying in 0. 1 M HCl solution at 25 °C was investigated by Picas *et al.* [40] using the electrochemical polarisation method. In contrast to the steel base and thin electrolytic hard chromium coating, HVOF sprayed WC-CoCr coatings can provide better corrosion protection in the extremely corrosive 0. 1 M HCl solution.

A significant improvement in corrosion resistance to both 1 mol/L HCl and 3. 5 wt.% NaCl solutions was seen by Zhang *et al.* [41] when they investigated the corrosion characteristics of HVOF-sprayed nano-structured WC-10Co4Cr coating in two corrosive salt environments.

The hot corrosion performance of the austenitic steel weld metal was examined by Xu *et al.* [42]. It was established that the surface of the weld metal developed an outer face rich in iron and a protective layer of Cr_2O_3 after being exposed to temperatures of 700 and 800 °C for 100 hours in a fused salt environment. Yet, because the molten salt dissolves the oxide film in a 650 °C KCl-NaCl-Na_2SO_4 salt environment, significant oxidation still happens in the weld metal.

A general methodology adopted for hot corrosion includes the following steps, as shown in Figure 1. The sample is first cut to the suitable size. Before the development of the coating, the samples are prepared using sandblasting or emery paper, followed by cleaning with acetone to remove small debris. The coatings were developed by thermal spraying to the targeted substrate using prepared/available feedstock powder.

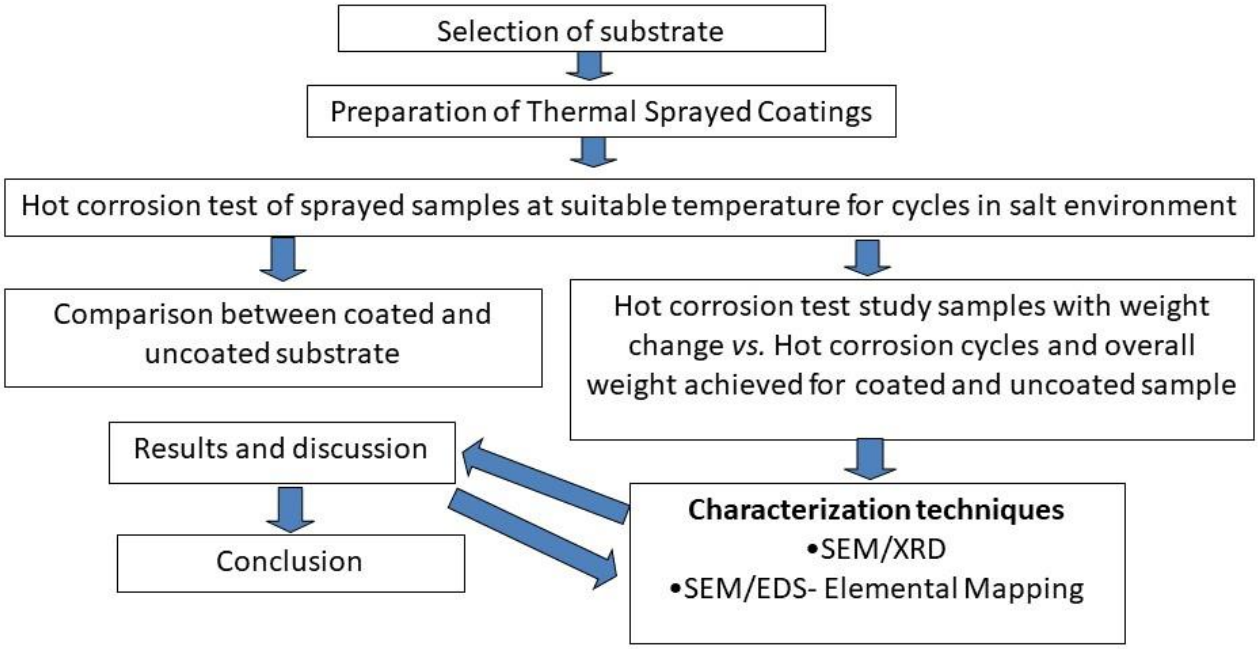

***Figure 1**. A General process flow chart for hot corrosion study*

Then, under cyclic conditions, hot-corrosion experiments were carried out in a highly corrosive salt environment of Na_2SO_4 or Na_2SO_4-NaCl or $Fe_2(SO_4)_3$ or $Fe_2(SO_4)_3$-NaCl or other corrosive salt and their combinations layered over the surface of the substrate for certain cycles. Each cycle consists

of a still-air cooling period after a high-temperature heating period around a certain temperature in a furnace. Following each hot corrosion cycle, the crucible and samples were mixed and weighed using an electronic weighing device. The spalled scales were also considered for calculating the overall corrosion rate during the weight change measurement. Surface area/weight growth was utilized to create corrosion kinetics.

X-ray diffraction analysis of the hot corroded scales

Before heat corrosion, the XRD pattern of the WC-CoCr coated surface (Figure 2) exhibits clear, sharp peaks for both WC and W_2C. The WC phase has been dissolved and decarburized, as shown by the rise in the height of the WC and W_2C peaks. The high surface area to volume ratio of feedstock powder, which made it easy for the WC atoms to interact with spraying temperature, is the primary source of decarburization in coatings [43].

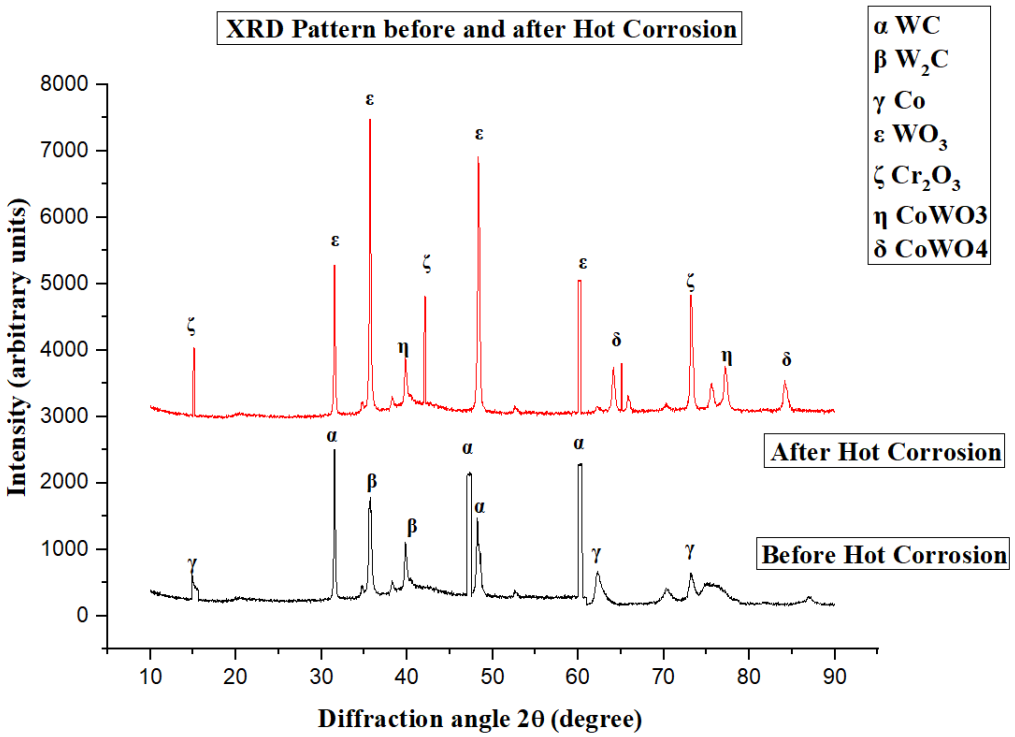

Figure 2. *XRD plot for WC-CoCr coatings and coated hot corroded scales. Reproduced from [44] with permission from Springer Nature*

Following fifty hot corrosion cycles, the XRD analysis of the WC-CoCr coated 316L steel substrate (Figure 3) revealed the formation of WO_3, CoW_3C, and $CoWO_4$ as the main phases. The intermediate phase, Cr_2O_3 and its spinel $CoCr_2O_4$, was caused by the chromium content and also contributed to the coating's ability to resist corrosion in a Na_2SO_4 25 % NaCl salt environment. Notable oxides were Fe_2O_3, $CoSO_4$, and $FeCr_2O_4$. There were also some Na traces found. A sizable number of oxide phases occurred after fifty cycles in a fused corrosive salt environment, indicating fast oxidation.

Figure 3 depicts the identified phases subjected to a salty environment $12Na_2SO_4$-$88Fe_2(SO_4)_3$ at 800 °C. XRD reveals that after hot corrosion, the specimen mainly consists of the following phases $FeSCr_2S_3$, Na_2FeO_2, $NiCr_2O_4$, and FeS phase.

A fused state of $NaFe(SO_4)_2$ is thought to develop (Equation (1)) when Na_2SO_4 and $Fe_2(SO_4)_3$ are mixed:

$$Na_2SO_4 + Fe_2(SO_4)_3 \rightarrow 2NaFe(SO_4)_2 \quad (1)$$

The Cr_2O_3 coating on the 316L steel is degraded (Equation (2)) when the alloy and this fused phase interact:

$$3Cr_2O_3 + 4NaFe(SO_4)_2 \rightarrow 2Na_2CrO_4 + 2FeS + 2Cr_2S_3 + 2Fe_2O_3 + 15O_2 \quad (2)$$

As a result, the oxide scale will be destroyed and sulphides and fluxing products will appear, as shown by Equations (3) and (4). The liquid phase further deteriorates the alloy:

$$3Fe + 2NaFe(SO_4)_2 \rightarrow 4FeS + Na_2FeO_2 + 7O_2 \quad (3)$$

$$3Ni + 2NaFe(SO_4)_2 \rightarrow 2FeS + 2NiS + Na_2NiO_2 + 7O_2 \quad (4)$$

The entire corrosion attack is controlled by the liquidus $NaFe(SO_4)_2$, and corrosion will likely be less severe because there isn't any Na_2SO_4 emission. The oxide scales on an alloy that corrodes at 800 °C are thicker than those that form at lesser temperatures. The fluxing products Na_2CrO_4, Na_2FeO_2, and Na_2NiO_2 and the development of gases cause the scales to crack or become disrupted. This causes the fused salt to contact metal and initiate a potent oxidation attack. The steel oxidizes and fluxes more quickly due to its easy oxygen availability.

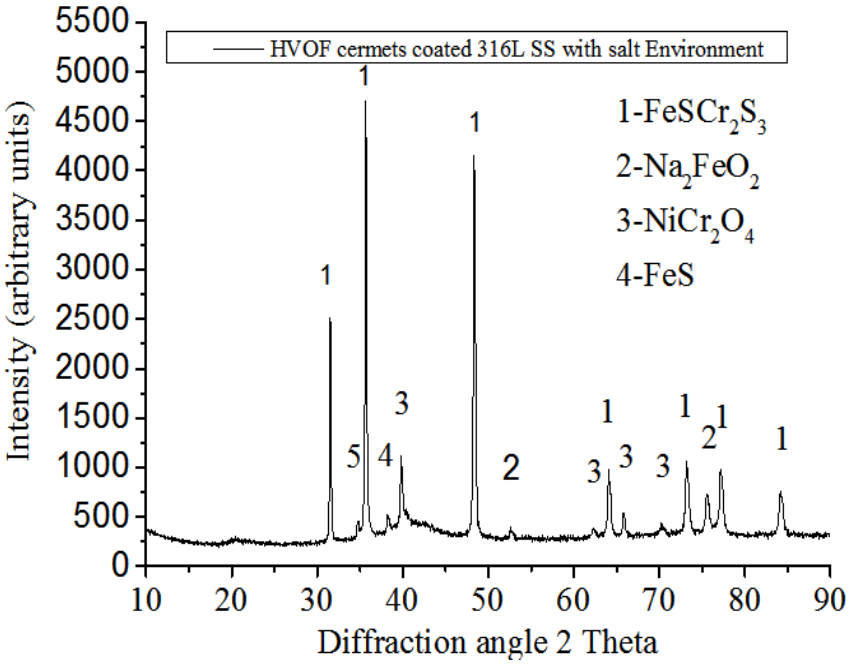

Figure 3. *XRD pattern of WC-CoCr coatings by HVOF spraying on 316L steel substrate in corrosive salt Environment. Reproduced from [45] with permission from Springer Nature*

Scanning electron microscopy analysis of the hot corroded scales

When exposed to a Na_2SO_4 + 25% NaCl salt environment, the unprotective oxide (Fe_2O_3) is generated as the surface scale of the uncoated steel substrate, allowing corrosive elements to penetrate the surface. Hot corrosion of an uncoated steel substrate results in unprotective Fe_2O_3 scales. Fe and Cl are shown as active elements in Figure 4's SEM image of the bare hot corroded sample. Fe creates an unprotective Fe_2O_3 oxide layer that is loosely retained after oxidation. Melted salt diffuses slits and cracks when it interacts with a steel substrate over 628 °C. This causes oxide scale development and oxidation to occur first.

Through the process of dissolution (Equations (5) to (10)), the fused salt paste's NaCl dissolves into Cl^- and Na^+ ions. The Cl^-ions then enter the substrate and react to form metal chlorides like $FeCl_2$ and $CrCl_2$.

$$NaCl \rightarrow Na^+ + Cl^- \quad (5)$$

$$Fe + Cl_2 \rightarrow FeCl_2 \quad (6)$$

$$4FeCl_2 + 3O_2 \rightarrow 2Fe_2O_3 + 4Cl_2 \quad (7)$$

$$2Cr_2O_3 + 8Cl^- \rightarrow 4CrCl_2 + 3O_2 \quad (8)$$

$$Na_2O + Cr_2O_3 + 1/2\ O_2 \rightarrow 2NaCrO_4 \quad (9)$$

$$4Fe + Na_2SO_4 \rightarrow 3FeO + Fes + Na_2O \quad (10)$$

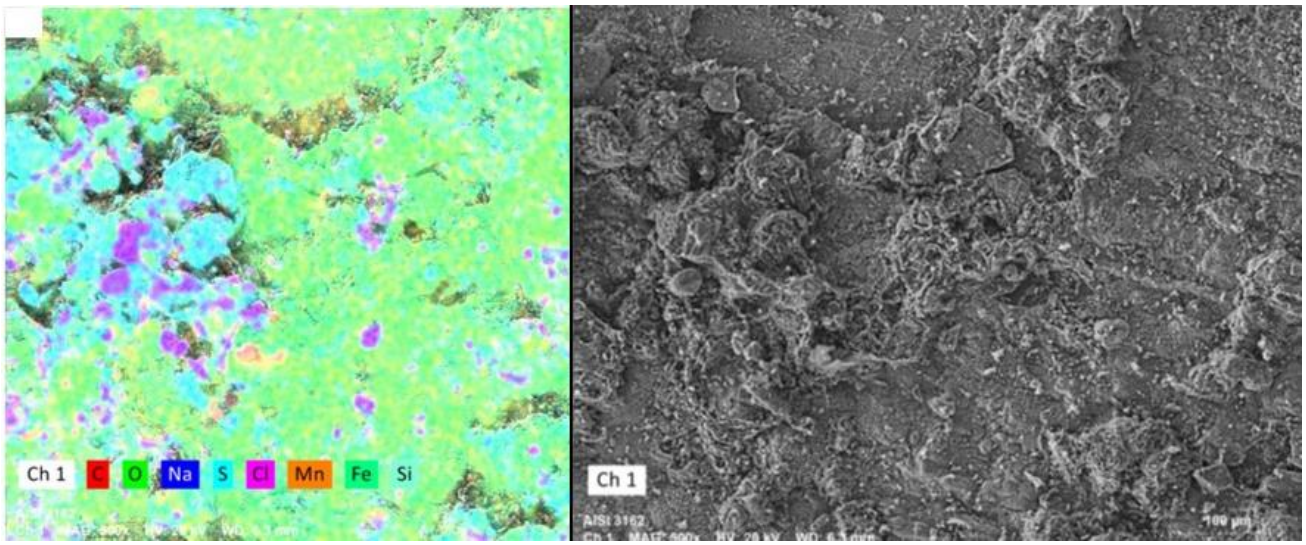

Figure 4. *SEM images of uncoated hot corroded scales. Reproduced from [44] with permission from Springer Nature*

On the top surface of the plasma sprayed WC-CoCr coated steel substrate, an adhering homogenous and continuous globular scale has formed after fifty hot corrosion cycles in a Na_2SO_4-NaCl fused salt environment (Figure 5a). Scales have largely maintained their lamellar structure throughout the investigation, as the SEM micrograph shows. Thermal stress is the cause of the microcracks that form in the scale. Open fissures expedited the entrance of corrosive materials during heating and cooling in hot corrosion cycling testing. This has made the coating's inner surface degradation more severe.

In the SEM image (Figure 5b), the scale appears to have a loose, hairy structure at higher magnifyications. The ensuing interactions between coating elements such as tungsten, cobalt, chromium, iron and the chlorine created by dissociation of NaCl result in highly volatile chlorides, which in turn cause a loose and uneven oxide scale [46]. These chlorides release chlorine when they diffuse from the scale and interact with the surrounding air oxygen.

Figure 6(a-d) shows the SEM evaluation of the cyclic corrosion of 316L steel, both bare and sprayed, in settings with 12 % Na_2SO_4-88 % $Fe_2(SO_4)_3$. The surface of the nude specimen is rather uneven. As demonstrated in Figure 6(a) and (b), the uncoated sample is considerably comparable at higher magnification, revealing some pit and fracture patterns. The SEM analysis suggests that intergranular cracking on the oxide scale may be indicated by certain surface cracks on the scale. Fe_2O_3 may form since oxygen and iron are found in significant concentrations throughout the scale's composition. There are also trace amounts of Mn, Cr, and Co.

SEM image of the hot corroded HVOF WC-CoCr 316L steel at high magnification (Figure 6(c,d)) reveals some visible globules and some unmelted powder.

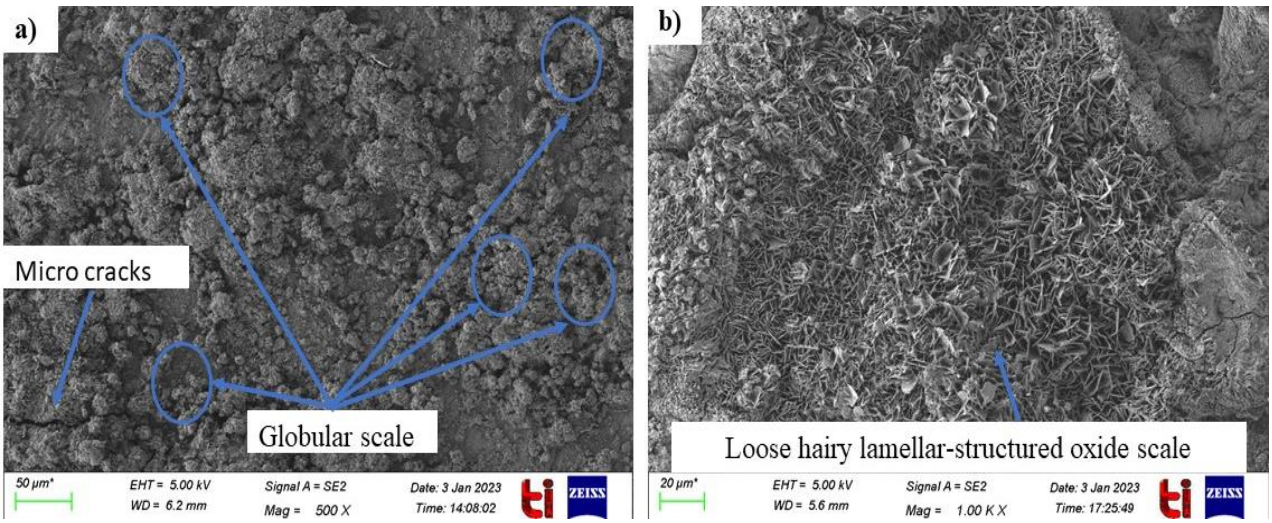

Figure 5. *SEM images of WC-CoCr coated hot corroded scales. Reproduced from Ref. [44] with permission from Springer Nature*

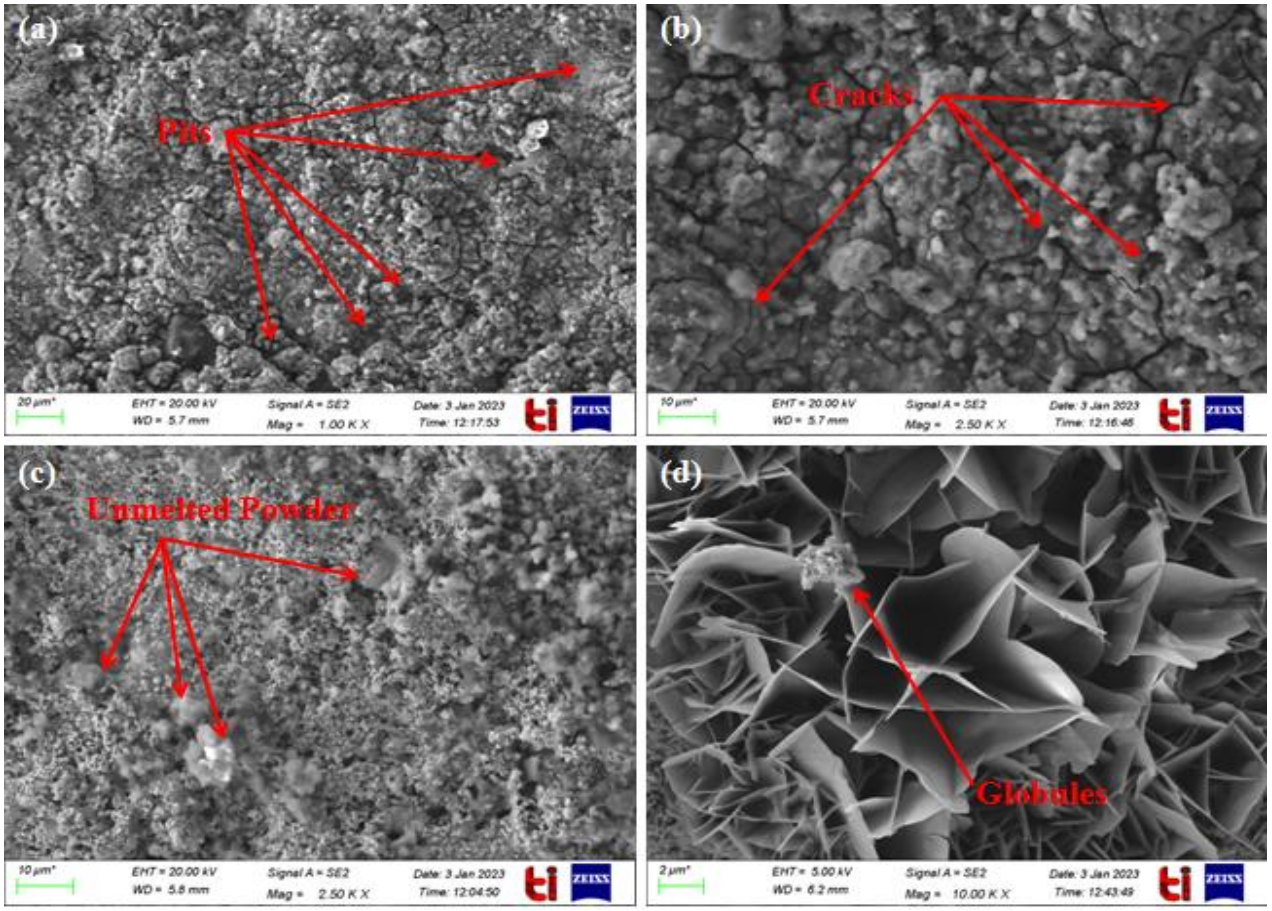

Figure 6. *SEM images (a-b) bare 316L steel (c-d) HVOF sprayed 316L steel in the corrosive salt environment at 800 °C. Reproduced from [45] with permission from Springer Nature*

The cross-sectional SEM images of the coated and bare samples following the hot corrosion test are displayed in Figure 7 (a) and (b). Figure 7(a) displays the surface for spalling and corrosion pits on bare samples when the magnification is increased [47]. Figure 7(b) shows the coated, hot-corroded sample's surface separation and microholes. This is the consequence of high-speed melt and semi-fused particles crossing over the substrate [48].

Some findings have been highlighted in Table 1

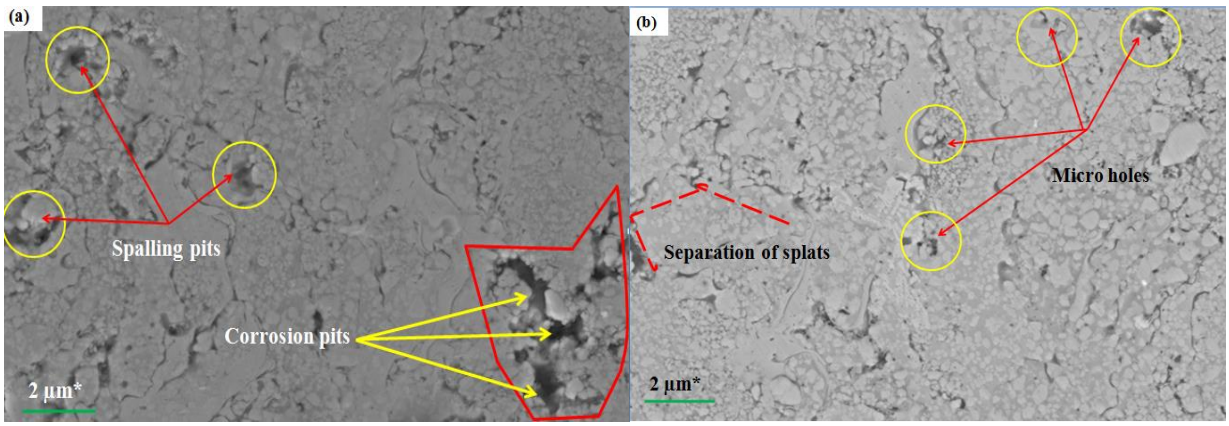

Figure 7. SEM image of cross-section (a) bare hot specimen (b) coated hot corroded specimen after hot corrosion. Reproduced from [45] with permission from Springer Nature

Table 1. *Comparative findings of coating characteristics on steel substrates*

Authors	Coating methods	Substrate	Coating powders	Findings
Alam *et al.* [44]	Plasma spray	AISI 316l	WC-Co-Cr	A significant rise in hot corrosion resistance.
Kumar *et al.* [48]	HVOF	AISI 1010	WC-Co and WC-Co-Cr	Oxidation and corrosion properties enhanced.
Alam *et al.* [49]	TIG	Carbon steel	WC, TiN and TiC,	Wear, corrosion and micro-hardness properties increased.
Hodgkiess *et al.* [50]	HVOF	Austenitic grade steel	Ni-Cr-Si-B-C	Corrosion and erosion characteristics enhanced.
De Souza and Neville [51]	D-Gun	UNS S31603 and UNS S32760	WC-Co-Cr	At liquid-solid impingement, good wear and corrosion resistance was attained.
Kumar *et al.* [52]	HVOF	SAE213 T22 and SA516Grade 70	Nano-structured Ni-20Cr	Increased resistance against erosion and corrosion in real boiler settings.
Hemmati *et al.* [53]	HVOF	carbon steel	Cr_3C_2-25NiCr	The findings demonstrated that the cladding was substantial enough to delay the onset and propagation of cracks.
Thi *et al.* [54]	APS	AISI 304	Cr_3C_2-25NiCr	Outperformed unprotected coating and sealed by traditional impregnation technique in terms of wear and corrosion resistance.
Xie *et al.* [55]	HVAF	AISI 316L	AlFeNiCoCr	Both corrosion and abrasion resistance are superior in the coating compared to the 316L stainless steel substrate.
Li *et al.* [56]	Plasma spray	38CrMoAl	Ni-Cr-Cr_3C_2	The coating's superior corrosion resistance performance is attributed to its substrate and plasma spraying technique, which enables the coating to accomplish metallurgical bonding and a more dense microstructure with high bonding strength, reduced porosity, and fewer cracks.
Jiang *et al.* [57]	Plasma spray	T91 steel	Fe-based amorphous coatings	Tested how the coating would react to heat (700 °C) in hot Na_2SO_4+K_2SO_4 salts. Due in part to the development of protective oxides of chromium and nickel, such as Cr_2O_3, NiO and $NiCr_2O_4$, the amorphous composite micro-structure and high Cr and Ni elemental concentrations produced the maximum hot corrosion resistance.
Zavareh *et al.* [58]	Plasma spray	Carbon steel	Al_2O_3-40TiO_2	The Al_2O_3-TiO_2 chemical composite that was created by the plasma spray method has better chemical and mechanical qualities.
Kannan *et al.* [59]	Plasma spray	Co-Cr-WC alloy(Stellite-21)	AZ91D-Mg alloy (Al-Zn-Mn)	When exposed to an environment that contains a coating of chloride on the binding metals, the AZ91D-Mg alloy covered with stellite cannot provide superior corrosion protection.

Summary and outlook

This article examines the most recent research and breakthroughs in the field of hot corrosion performance of various coatings. The coatings on the substrate exhibited greater hot corrosion resistance due to the protective WO_3/Cr_2O_3, etc. phases. The developed phases serve as a mechanism of transportation across this scale. These are typically slow growth in nature. Thus, an oxide retards/prevents the inward diffusion of gaseous/vapour impurities and the outward diffusion of other alloy elements.

References

[1] J. Stringer, Performance limitations in electric power generating systems imposed by high temperature corrosion, *High Temperature Technology* **3(3)** (1985) 119-141. https://doi.org/10.1080/02619180.1985.11753292

[2] J. Stringer, Coatings in the electricity supply industry: past, present, and opportunities for the future, *Surface and Coatings Technology* **108-109** (1998) 1-9. https://doi.org/10.1016/S0257-8972(98)00642-2

[3] A. R. Rapp, Y. S. Zhang. Hot corrosion of materials: fundamental studies. *JOM* **46** (1994) 47-55. https://doi.org/10.1007/BF03222665

[4] A. R. Rapp, Hot corrosion of materials: a fluxing mechanism?, *Corrosion Science* **44(2)** (2002) 209-221. http://dx.doi.org/10.1016/S0010-938X(01)00057-9

[5] T. S. Sidhu, A. Malik, S. Prakash, R. D. Agrawal, Oxidation and hot corrosion resistance of HVOF WC-NiCrFeSiB coating on Ni-and Fe-based superalloys at 800 C, *Journal of Thermal Spray Technology* **16** (2007) 844-849. https://doi.org/10.1007/s11666-007-9106-8

[6] N. Kumar, V. K. Choubey, Investigation of microstructure and Isothermal oxidation resistance of cermet HVOF coated on AISI316L at 900 °C, *Results in Surfaces and Interfaces* **14** (2024) 100173. https://doi.org/10.1016/j.rsurfi.2023.100173

[7] K. L. Luthra, and H. S. Spacil, Impurity deposits in gas turbines from fuels containing sodium and vanadium, *Journal of the electrochemical society* **129(3)** (1982) 649. https://doi.org/10.1149/1.2123941

[8] S. P. Zhu, H. Z. Huang, W. Peng, H. K. Wang, S. Mahadevan, Probabilistic physics of failure-based framework for fatigue life prediction of aircraft gas turbine discs under uncertainty, *Reliability Engineering & System Safety* **146** (2016) 1-12. https://doi.org/10.1016/j.ress.2015.10.002

[9] B. Salehnasab, E. Poursaeidi, S. A. Mortazavi, G. H. Farokhian, Hot corrosion failure in the first stage nozzle of a gas turbine engine, *Engineering Failure Analysis* **60** (2016) 316-325. https://doi.org/10.1016/j.engfailanal.2015.11.057

[10] S. Madhavan, Rajeev Jain, C. Sujatha, A. S. Sekhar, Vibration based damage detection of rotor blades in a gas turbine engine, *Engineering Failure Analysis* **46** (2014) 26-39. https://doi.org/10.1016/j.engfailanal.2014.07.021

[11] D. Pradhan, G. S. Mahobia, K. Chattopadhyay, V. Singh, Effect of surface roughness on corrosion behavior of the superalloy IN718 in simulated marine environment, *Journal of Alloys and Compounds* **740** (2018) 250-263. https://doi.org/10.1016/j jallcom.2018.01.042

[12] D. J. Baxter, K. Natesan, Breakdown of chromium oxide scales in sulfur-containing environments at elevated temperatures, *Oxidation of metals* **31** (1989) 305-323. https://doi.org/10.1007/BF00846691

[13] B. A. Gordon, V. Nagarajan, Preliminary observations of the thermodynamic predictions of Fe-Cr-Ni alloys in coal gasifier environments, *Oxidation of Metals* **13** (1979) 197-202. https://doi.org/10.1007/BF00611979

[14] M. F. Stroosnijder, W. J. Quadakkers, Review of high temperature corrosion of metals and alloys in sulphidizing/oxidizing environments II. Corrosion of alloys, *High Temperature Technology* **4(3)** (1986) 141-151. https://doi.org/10.1080/02619180.1986.11753329
[15] N. Eliaz, G. Shemesh, R. M. Latanision, Hot corrosion in gas turbine components, *Engineering failure analysis* **9(1)** (2002) 31-43. https://doi.org/10.1016/S1350-6307(00)00035-2
[16] N. Kumar, V. K. Choubey, Recent trends in coating processes on various AISI steel substrates, *Journal of Materials Science* **59(2)** (2024) 395-422. https://doi.org/10.1007/s10853-023-09239-z
[17] F. Pettit, Hot corrosion of metals and alloys, *Oxidation of Metals* **76** (2011) 1-21. https://doi.org/10.1007/s11085-011-9254-6
[18] M. M. Barbooti,, S. H. Al-Madfai, H. J. Nassouri, Thermochemical studies on hot ash corrosion of stainless steel 304 and inhibition by magnesium sulphate, *Thermochimica acta* **126** (1988) 43-49. https://doi.org/10.1016/0040-6031(88)87248-4
[19] K. Natesan, Corrosion-erosion behavior of materials in a coal-gasificationenvironment, *Corrosion* **32(9**) (1976) 364-370. https://doi.org/10.5006/0010-9312-32.9.364
[20] J. Congleton, W. Zheng, H. Hua, Stress corrosion cracking of annealed type 316 stainless steel in high-temperature water, *Corrosion* **46(8)** (1990) 621-627. https://doi.org/10.1016/0010-938X(85)90010-1
[21] A. Hendry, D. J. Lees, Corrosion of austenitic steels in molten sulphate deposits, *Corrosion Science* **20(3)** (1980) 383-404. https://doi.org/10.1016/0010-938X(80)90007-4
[22] N. Kumar, V. K. Choubey, Comparative evaluation of oxidation resistance of detonation gun-sprayed Al_2O_3-40% TiO_2 coating on nickel-based superalloys at 800 °C and 900 °C, *High Temperature Corrosion of Materials* **99(5)** (2023) 359-373. https://doi.org/10.1007/s11085-023-10157-3
[23] N. Kumar, V. K. Choubey, Experimental investigation on hot corrosion, oxidation and microstructure of WC based cermet HVOF coating, *High Temperature Corrosion of Materials* **101** (2023) 413-432. https://doi.org/10.1007/s11085-023-10179-x
[24] A. K. Koul, J. P. Immarigeon, R. V. Dainty, P. C. Patnaik, *Degradation of high performance aero-engine turbine blades,* in *Advanced materials and coatings for combustion turbines*, V. P. Swaminathan, N. S. Cheruvu, Eds., ASM International, Materials Park, OH, USA, 1994, p. 69-74. ISBN 9780871704870. https://books.google.co.in/books?id=19NSAAAAMAAJ
[25] N. K. Mishra, N. Kumar, S. B. Mishra, Hot Corrosion Behaviour of Detonation Gun Sprayed Al_2O_3-40TiO_2 Coating on Nickel Based Superalloys at 900° C. *Indian Journal of Materials Science* **2014** (2014). https://doi.org/10.1155/2014/453607
[26] T. S. Sidhu, S. Prakash, R. D. Agrawal, Hot corrosion and performance of nickel-based coatings, *Current Science* **90(1)** (2006) 41-47. https://www.jstor.org/stable/24089016
[27] S. Topolska, Santina J. Labanowski, Corrosion of evaporator tubes in low emission steam boilers, *Archives of Materials Science and Engineering* **42(2)** (2010) 85-92. http://www.amse.acmsse.h2.pl/vol42_2/4223.pdf
[28] S. Ishigai, *Steam power engineering: Thermal and hydraulic design principles*, Cambridge University Press, 1999. ISBN 9780521135184
[29] M. H. Guo, Q. M. Wang, P. L. Ke, J. Gong, C. Sun, R. F. Huang, L. S. Wen, The preparation and hot corrosion resistance of gradient NiCoCrAlYSiB coatings, *Surface and Coatings Technology* **200(12-13)** (2006) 3942-3949. https://doi.org/10.1016/j.surfcoat.2004.12.005
[30] T. S. Sidhu, S. Prakash, R. D. Agrawal, Hot corrosion studies of HVOF NiCrBSi and Stellite-6 coatings on a Ni-based superalloy in an actual industrial environment of a coal fired boiler, *Surface and Coatings Technology* **201(3-4)** (2006) 1602-1612. https://doi.org/10.1016/j.surfcoat.2006.02.047

[31] T. S. Sidhu, A. Malik, S. Prakash, R. D. Agrawal, Oxidation and hot corrosion resistance of HVOF WC-NiCrFeSiB coating on Ni-and Fe-based superalloys at 800 C, *Journal of Thermal Spray Technology* **16** (2007) 844-849. https://doi.org/10.1007/s11666-007-9106-8

[32] G. M. Liu, F. Yu, J. H. Tian, J. H. Ma, Influence of pre-oxidation on the hot corrosion of M38G superalloy in the mixture of Na_2SO_4-NaCl melts, *Materials Science and Engineering A* **496(1-2)** (2008) 40-44. https://doi.org/10.1016/j. msea. 2008. 04. 046

[33] E. Liu, Z. Zheng, X. Guan, J. Tong, L. Ning, Y. Yu, Influence of Pre-oxidation on the Hot Corrosion of DZ68 Superalloy in the Mixture of Na_2SO_4-NaCl, *Journal of Materials Science & Technology* **26(10)** (2010) 895-899. https://doi.org/10.1016/S1005-0302(10)60143-0

[34] S. Kamal, R. Jayaganthan, S. Prakash, High temperature cyclic oxidation and hot corrosion behaviours of superalloys at 900 C, *Bulletin of Materials Science* **33** (2010) 299-306. https://doi.org/10.1007/s12034-010-0046-4

[35] W. Wang, C. Zhou, Hot corrosion behaviour of Nbss/Nb5Si3 in situ composites in the mixture of Na_2SO_4 and NaCl melts, *Corrosion science* **74** (2013) 345-352. https://doi.org/10.1016/j.corsci.2013.04.057

[36] V. P. S. Sidhu, K. Goyal, R. Goyal, Comparative evaluation of hot corrosion resistance of 83WC-17CO and 86WC-10CO-4Cr coatings on some boiler steels in actual boiler in thermal power plant, *Metallography, Microstructure, and Analysis* **6** (2017) 512-518. https://doi.org/10.1007/s13632-017-0392-3

[37] W. Zhou, K. Zhou, C. Deng, K. Zeng, Y. Li, Hot corrosion behaviour of HVOF-sprayed Cr3C2-NiCrMoNbAl coating, *Surface and Coatings Technology* **309** (2017) 849-859. https://doi.org/10.1016/j.surfcoat.2016. 10.076

[38] Y. Qiao, J. Kong, X. Guo, Hot corrosion phenomena of Nb-Ti-Si based alloy and its silicide coating induced by different corrosive environments at 900° C, *Ceramics International* **44(7)** (2018) 7978-7990. https://doi.org/10.1016/j.ceramint.2018.01.238

[39] L. Wei, W. Shao, M. Li, C. Zhou, Hot corrosion behaviour of Mo-62Si-5B (at.%) alloy in different molten salts at 900 °C, *Corrosion Science* **158** (2019) 108099. https://doi.org/10.1016/j.corsci.2019.108099

[40] J. A. Picas, M. Punset, E. Rupérez, S. Menargues, E. Martin, M. T. Baile, Corrosion mechanism of HVOF thermal sprayed WC-CoCr coatings in acidic chloride media, *Surface and Coatings Technology* **371** (2019) 378-388. https://doi.org/10.1016/j.surfcoat.2018.10.025

[41] Y. Zhang, S. Hong, J. Lin, Y. Zheng, Influence of ultrasonic excitation sealing on the corrosion resistance of HVOF-sprayed nano-structured WC-CoCr coatings under different corrosive environments, *Coatings* **9(11)** (2019) 724. https://doi.org/10.3390/coatings9110724

[42] Z. Xu, W. Jinchu, Y. Zonghui, Z. Hui, P. Cong, C. Yajie, L. Xiaoquan, Hot Corrosion Behavior of Fe-Cr-Ni-Based Austenitic Heat-Resistant Steel Weld Metal in Na_2SO_4-NaCl Molten Salts at Different Temperatures, *HighTemperature Corrosion of Materials* **99(1)** (2023) 117-132. https://doi.org/10.1007/s11085-022-10144-0

[43] Y. S. Hwang, D. B. Lee, High-Temperature Oxidation of WC-20%TiC-10%Co Carbides, *Advanced Materials Research* **811** (2013) 93-97. https://doi.org/10.4028/www.scientific.net/AMR.811.93

[44] M. S. Alam, A. K. Das, Hot corrosion behavior of plasma-sprayed WC-CoCr coatings on AISI 316L steel substrate in Na_2SO_4-25% NaCl salt environment, *High Temperature Corrosion of Materials* **99(5)** (2023) 415-430. https://doi.org/10.1007/s11085-023-10162-6

[45] N. Kumar, M. S. Alam, V. Mishra, H. Vasudev, P. C. Yadav, V. K. Choubey, A comparative investigation of the effects of temperature on the oxidation resistance of high-velocity oxy-fuel coating on AISI316L, *Physica Scripta* **99** (2024) 055031. 10.1088/1402-4896/ad3c7a

[46] I. Gurrappa, Hot Corrosion Behavior of CM 247 LC Alloy in Na_2SO_4 and NaCl Environments, *Oxidation of Metals* **51** (1999) 353-382 https://doi.org/10.1023/A:1018831025272

[47] C. W. Lee, J. H. Han, J. Yoon, M. C. Shin, S. I. Kwun, A study on powder mixing for high fracture toughness and wear resistance of WC-Co-Cr coatings sprayed by HVOF, *Surface and Coatings Technology* **204** (2010) 2223-2229. https://doi.org/10.1016/j.surfcoat.2009.12.014
[48] N. Kumar, V. K. Choubey, Effect of WC-Co and 86WC-10Co-4Cr coatings on type-II hot corrosion behaviour & microstructure characteristics at 650 degree celsius, *Surface and Coatings Technology* **469** (2023) 129812. https://doi.org/10.1016/j.surfcoat.2023.129812
[49] M. S. Alam, A. K. Das, Advancement in cermet based coating on steel substrate, *Materials Today: Proceedings* **56** (2022) 805-810.https://doi.org/10.1016/j.matpr.2022.02.260
[50] T. Hodgkiess, A. Neville, S. Shrestha, Electrochemical and mechanical interactions during erosion-corrosion of a high-velocity oxy-fuel coating and a stainless steel, *Wear* **233** (1999) 623-634. https://doi.org/10.1016/S0043-1648(99)00246-X
[51] V. A. de Souza, A Neville, Corrosion and erosion damage mechanisms during erosion-corrosion of WC-Co-Cr cermet coatings, *Wear* **255(1-6)** (2003) 146-156. https://doi.org/10.1016/S0043-1648(03)00210-2
[52] M. Kumar, H. Singh, N. Singh, Fire side erosion-corrosion protection of boiler tubes by nano-structured coatings, *Materials and Corrosion* **66(7)** (2015) 695-709. https://doi.org/10.1002/maco.201407954
[53] A. R. Hemmati, S. M. Soltanieh, S. M. Masoudpanah, On the interaction between erosion and corrosion in chromium carbide coating, *Journal of Bio-and Tribo-Corrosion* **4** (2018) 10. https://doi.org/10.1007/s40735-018-0128-1
[54] H. P. Thi, T. N. Van, T. A. Nguyen, L. P. Thi, T. D. Bich, C. L. Quoc, Cr_3C_2-25NiCr cermet coating: Preparation, PTFE sealant, wear and corrosion resistances, *Journal of Thermal Spray Technology* **30** (2021) 716-724. https://doi.org/10.1007/s11666-021-01155-5
[55] X. Xie, B. Yin, F. Yin, X. Ouyang, X. Ouyang, Corrosion behavior of FeB-30 wt. % Al0. 25FeNiCoCr cermet coating in liquid zinc, *Coatings* **11(6)** (2021) 622. https://doi.org/10.3390/coatings11060622
[56] S. Q Li, Q. L. Li, S. L. Gong, C. Wang, Researching for corrosion-resistance performance of laser-hybrid plasma spraying NiCr-Cr3C2 coating, *Physics Procedia* **18** (2011) 211-215. https://doi.org/10.1016/j.phpro.2011.06.083
[57] C. Jiang, W. Liu, G. Wang, Y. Chen, Y. Xing, C. Zhang, M. Dargusch, The corrosion behaviours of plasma-sprayed Fe-based amorphous coatings, *Surface Engineering* **34(8)** (2018) 634-639. https://doi.org/10.1080/02670844.2017.1319647
[58] M. A. Zavareh, A. A. D. M. Sarhan, B. B. A. Razak, W. J. Basirun, Plasma thermal spray of ceramic oxide coating on carbon steel with enhanced wear and corrosion resistance for oil and gas applications, *Ceramics International* **40(9)** (2014) 14267-14277. https://doi.org/10.1016/j.ceramint.2014.06.017
[59] K. Mathivanan, D. Thirumalaikumarasamy, P. Thirumal, M. Ashokkumar, Investigate the corrosion properties of stellite coated on AZ91D alloy by plasma spray technique, *Thermal Science* **26(2)** (2022) 911-920. https://doi.org/10.2298/TSCI200722209K

J. Electrochem. Sci. Eng. **14(4)** (2024) 473-486; http://dx.doi.org/10.5599/jese.2135

Open Access : : ISSN 1847-9286
www.jESE-online.org

Original scientific paper

Electrochemical behaviour of Ti6Al4V porous structures fabricated by powder metallurgy route

Maninder Singh[1], Amoljit Singh Gill[1,✉] and Parneet Kaur Deol[2]

[1]*Department of Mechanical Engineering, I. K. Gujral Punjab Technical University, Kapurthala, Punjab, India*

[2]*Department of Pharmaceutics, G.H.G. Khalsa College of Pharmacy Gurusar Sadhar, Ludhiana, Punjab, India*

Corresponding authors: ✉*amol_gill@rediffmail.com*; Tel.: +91-9988700421

Received: October 16, 2023; Accepted: February 11, 2024; Published: February 21, 2024

Abstract

In this investigation, the powder metallurgy process was used to fabricate porous structures of Ti6Al4V alloy by adding space holder powder particles. The samples were fabricated with varying levels of compaction pressure and other process parameters were kept unchanged in order to investigate the variation in electrochemical behaviour. It was observed that a lower level of compaction pressure resulted in an increase in corrosion current density and rate and a decrease in polarisation resistance. The sample's inability to achieve passivity against electrochemical corrosion, when fabricated using a lower level of compaction pressure, was linked to a higher number of interconnecting micropores. The results of the microstructure analysis confirmed the significant densification of the powder particles when higher compaction pressure was used. The study recommends that a compaction pressure of 300 MPa or higher may be used for fabricating porous structures for biomedical applications.

Keywords

Titanium alloy; biomaterials; space holder; compaction pressure; corrosion

Introduction

The rapid expansion of the biomedical implant sector has contributed to the substantial increase in human life expectancy [1]. This demographic information shows a higher incidence of degenerative ailments, including conditions such as arthritis and osteoporosis [2]. These conditions often result in discomfort or impairment of biological functions. Specifically, there has been a notable increase in primary total hip arthroplasty (THA) and primary total knee arthroplasties (TKA) [3]. Natural bone consists of two main types of hard tissues: cortical bone and cancellous bone. Cortical bone is characterized by its hardness and density, with porosity ranging from 5 to 10% and an elastic modulus ranging from 3 to 30 GPa. On the other hand, cancellous bone is composed of a

spongy network of trabecular bone, exhibiting a much higher porosity of 50 to 90 % and a lower elastic modulus within the range of 0.02 to 2 GPa [4].

The origin of modern implantology can be traced back to the late 19th century. Around this time, significant developments were made in the field. In 1891, researchers experimented with implants constructed from materials such as porcelain and gutta-percha [5,6]. Payne *et al*. took a different approach, using gold-plated tin capsules filled with gutta-percha [7]. However, as mentioned earlier, solid metal implants possess a significantly higher elastic modulus than natural bone. This dissimilarity can lead to a phenomenon known as stress shielding following implantation [8]. Stress shielding, in turn, triggers the dissolution and absorption of the bone tissue that is not under load, potentially causing the implant to become loose over time [9]. Inadequate osseointegration is another concern that hinders the promotion of bone ingrowth and the establishment of a strong bond between the implant and the surrounding bone [10].

Porous metallic structures have gained significant attention in recent years due to their ability to mimic the properties of natural tissues and promote integration within the human body. These structures are intricately designed with interconnected pores that can be customized to attain specific mechanical and biological properties. Such materials hold great promise for biomedical applications, particularly in the development of implants aimed at improving the lives of patients with various medical conditions. Bone implants featuring porous structures prove more effective in preventing subsidence and fostering osseointegration, primarily due to their similarity to the elastic modulus of natural bone [11].

The selection of implant biomaterial stands as a pivotal factor in ensuring the long-term success of implants. The selection of the right implant material is crucial for the success of medical interventions. Each material comes with its advantages and limitations, making it essential to carefully consider the specific application and patient needs. The earliest documented dental implants, crafted from materials like stone and ivory, have historical records tracing back to ancient China and Egypt. Additionally, in the 16^{th} and 17^{th} centuries, dental implants made from gold and ivory were reported [12]. Researchers studied various implant materials and their pivotal role in the success of medical interventions. Various implant materials, including wood, leather, cotton, silk, coral, animal bones, ivory, bitumen, glass, pyrex, bakelite, Formica laminate, and ceramics, have been studied for medical implant applications [13]. However, these early materials exhibited several shortcomings, such as limited durability, low biocompatibility, and restricted availability, rendering them unsuitable for long-term medical use. Consequently, the quest for stable implant materials led to the exploration of metals. Copper and its alloys were initially considered favourable for biomedical applications due to their affordability and bactericidal properties [14]. Nevertheless, they lacked the required durability for load-bearing applications and produced irritant and toxic salts when in contact with the biological environment, making them unsuitable for extended medical use. Other materials like gold, silver, platinum, and ruthenium were also explored but were found to have sufficient irritancy and toxicity to control microbial growth. Researchers also conducted an in-depth examination of the benefits associated with stainless steel [15]. This material is known for its durability, malleability, and compatibility with the human body, presenting an encouraging option. Nonetheless, it faces challenges over time due to its exposure to the body's fluctuating pH levels and corrosive surroundings. Despite the popularity of AISI 316L stainless steel as a preferred alloy for bio-implants, it is essential to note that it may release nickel and chromium, potentially triggering allergic reactions in certain patients. Zinc, a vital element for metabolism, holds promise for various biomedical applications, particularly orthopedic implants and cardiovascular treatments. Yet, its relatively low strength and plasticity pose challenges for long-term

biodegradable applications [16,17]. Cobalt-chromium-molybdenum (CoCrMo) alloys, rich in cobalt, molybdenum, and chromium, gained recognition for their biocompatibility, wear resistance, and corrosion resistance [18]. They found applications in surgical instruments, joint components, and dental prostheses. However, their susceptibility to break during bending and potential immune reactions limits their suitability in certain scenarios. Polymer biomaterials, particularly ultra-high molecular weight polyethylene (UHMWPE), offer inert and biocompatible solutions. Still, wear debris can lead to inflammation and tissue damage [19]. Magnesium, a biodegradable essential element in the human body, holds promise for orthopedic implants. However, its low strength and plasticity present challenges [20].

Titanium, specifically Ti6Al4V, offers an ideal blend of strength, biocompatibility, and corrosion resistance, making it a top choice for various implants [21]. Ti6Al4V excels in mechanical strength, which is particularly important in load-bearing applications. Its corrosion resistance, biocompatibility, and osseointegration capabilities further support its suitability for bio-implants [22,23]. Ti6Al4V, with its outstanding properties and clinical track record, emerges as a preferred choice for bio-implants, contributing to improved patient outcomes and enhanced quality of life [24] and, hence, used for the current investigation.

Fabrication plays a crucial role in customizing desired physical properties, including pore size, interconnectivity for bone ingrowth, and porosity, in implant manufacturing. Various fabrication techniques, such as injecting gas in liquid metal [25], introducing a foaming agent in molten metal [26], indirect foaming technique [26] and powder metallurgy technique [27] have been explored by the researchers to create implants with tailored properties. Space holder-based powder metallurgy process offers cost-effectiveness, enhanced porosity, and parameter control for fabricating porous metallic structures. It follows conventional powder metallurgy principles, employing metallic and space holder materials (*e.g.,* NaCl, boron carbide, saccharose, carbamide, ammonium hydrogen carbonate) to effectively regulate porous structures and improve component efficiency [28]. The mixture of metal powder and space holder powder is compacted to form a green compact. The space holder powder is further removed by the water leaching method or thermal disintegration, leaving behind the final porous metallic structure.

Titanium and its alloys demonstrate remarkable corrosion resistance due to their characteristic of building a protective oxide layer on the surface [29]. The observations made in various studies related to electrochemical corrosion analysis of porous structures of titanium alloys fabricated using the powder metallurgy process are presented in Table 1. Various studies have highlighted the risk of crevice corrosion of titanium structures fabricated using a powder metallurgy process [30-33]. The present study uses a space holder-based powder metallurgy process for fabricating porous structures of titanium alloy Ti6Al4V. Numerous studies have explored the fabrication of porous structures of titanium and its alloys using space holder-based powder metallurgy technique and reported attainment of properties similar to that of natural bone tissue [34]. However, most of these investigations concentrate on the mechanical properties of the porous structures, pore size distribution, and morphology of the emerging porosities. Few reports in the literature look at the variation of corrosion behaviour of porous titanium alloys with powder metallurgy parameters.

The investigation of corrosion is of immense importance. If a metallic implant is susceptible to higher corrosion inside the human body, it will release allergenic, toxic/cytotoxic or carcinogenic elements (*e.g.,* Ni, Co, Cr, V, Al) *in situ*. This will not only burden the body with severe health effects but will also worsen the mechanical qualities of an implant. The resistance of Ti implants against corrosion is highly dependent on the chemical composition of the alloy and the presence of pores [35].

While investigating the effect of the space holder content on the corrosion behaviour of the Ti-16Nb alloy, E Yılmaz *et al.* [36] observed that corrosion resistance got lowered with an increase in space holder content. The effect was attributed to an increase in the porosity of the structures with an increase in space holder content. Compaction pressure has been identified as one of the most significant parameters of the powder metallurgy process that alters the porosity of the fabricated parts [37]. The present study aims to investigate the variation of electrochemical corrosion behaviour of porous structures fabricated using a space holder-based powder metallurgy process by considering compaction pressure as a variable parameter. The study also focuses on identifying the nature of porosity that affects the electrochemical corrosion behaviour of fabricated porous structures.

Table 1. *Observations related to electrochemical corrosion analysis of titanium-based porous structures fabricated using powder metallurgy process*

Titanium alloys	Fabrication process used	Important observations	Ref.
Ti powders	Micro-arc oxidation (MAO) treated samples fabricated using powder metallurgy process	Improved corrosion behaviour has been observed after MAO treatment. Higher improvement was observed in the case of denser samples as compared to porous samples.	[38]
Ti6Al4V/xCu composite	Powder metallurgy	The creation of Ti_2Cu and intermetallic phases during sintering may cause the beneficial impact of adding Cu, which may encourage the formation of a more stable passive layer than that produced by Ti.	[39]
Ti35Nb7Zr5Ta alloy	Powder metallurgy (fully dense and loose sintering)	Electrical impedance values of fully dense β-Ti alloy have been found twice as high as those of commercially pure Ti, and for loose sintered specimens, they were almost five times higher.	[40]
Ti10Mo	Powder metallurgy (porosity variation using space holder content)	With increase in porosity from 2.8 to 66.9 %, the corrosion rate has been found increased exponentially from 1.6 to 17.1 g m^{-2}·day^{-1}.	[41]
TiAg alloys	Powder metallurgy (routes: mechanical alloying (MA) and blended elemental (BE))	The amount and distribution of intermetallic Ti_2Ag in the samples produced with the BE powders have been found directly connected to their superior corrosion resistance compared to the MA samples. The corrosion resistance of TiAg alloys has been found decreased by a significant amount of intermetallics present inside and on the edges of the grains.	[42]
Ti50Ta alloy	Powder metallurgy (variable sintering cycles)	The sintering process longer than 24 h has resulted in more porous and less homogeneous structures. Reduction in resistance to corrosion has been observed at higher sintering temperatures. It has been proposed that the oxide layer developed on the surface of samples fabricated using 24 h sintering cycle was more compact and offered superior corrosion protection than that of the pure Ti.	[43]
Ti35Zr28Nb	Powder metallurgy (porosity variation using space holder content)	With increase in porosity from 51.4 to 64.9 %, the corrosion rate has been found increased from 0.91 to 4.18 μm $year^{-1}$. The porous Ti35Zr28Nb samples demonstrated higher compressive yield strength and decreased corrosion rate as compared to unalloyed Ti samples with almost same porosity.	[44]
Ti40Nb and Ti25Nb5Fe	Powder metallurgy (variable sintering cycles)	For both alloys, samples sintered at 1250 °C for 4 h have demonstrated greater corrosion resistance than samples processed for 2 h.	[45]
Ti6Al4V	Powder metallurgy with halide surface treatment	Halide treatment at 200 °C with NH_4Cl has increased resistance of powder metallurgy sample against corrosion and oxidation at high temperatures.	[46]
Ti16Nb	Powder metallurgy (porosity variation using space holder content)	Corrosion resistance decreased as porosity increased.	[36]

Experimental

A spherical-shaped powder of titanium alloy Ti6Al4V with 99.8 % purity was used to prepare the samples. Ammonium bicarbonate was used as space holder powder because of its easy removal by thermal disintegration during the sintering process. Standard ASTM E-11 was followed to obtain a particle size of 325 mesh of metal powder and 50 mesh of space holder powder using standard sieves [47]. The powder particle size was selected from the literature to match the pore size range favourable for bone growth and vascularization and obtain the required physical strength for bone tissue engineering [48-52].

The porous metallic structures were fabricated using the standard powder metallurgy process consisting of mixing, compaction and sintering. Ti6Al4V powder, ammonium bicarbonate powder and ethanol (2 vol.%, as adhesive) were mixed for 2 h in a rotary mixer to achieve homogeneity. The content of the space holder in the mixture was kept at 30 wt.%. The mixture was further compacted under four distinct uniaxial compaction conditions using a die set and compression testing machine with a crosshead speed of 5 mm min^{-1}. The compacts were then sintered under vacuum conditions (10^{-5} mbar) in a tube furnace. The space holder removal operation was carried out at 200 °C for three hours and the final sintering conditions were fixed at 1200 °C for two hours. The parameters for fabrication of porous structures are summarised in Table 2. As the intended application of these porous structures is load-bearing implants, the selection of the parameters is based upon the recommendations made in various studies (listed in Table 1) to achieve mechanical properties for hard-tissue engineering applications. The fabricated samples were coded as Ti6Al4V-200, Ti6Al4V-300, Ti6Al4V-400 and Ti6Al4V-500 as per the value of used compaction pressure, *i.e*., 200 MPa, 300 MPa, 400 MPa and 500 MPa, respectively.

Table 2. *Parameters for powder metallurgy*

Parameter	Value
Compaction pressure, MPa	200, 300, 400, 500
Ti6Al4V powder particle size, mesh	325
Ammonium bicarbonate particle size, mesh	50
Percentage of *ammonium bicarbonate, w*t.%	30
Sintering temperature, *°C*	*1200*

The fabricated porous samples were polished, degreased in acetone, rinsed with water and air-dried before electrochemical corrosion testing. Phosphate-buffered saline solution (pH of 7.4 at 37°C) (composition: NaCl 8.0 g L^{-1}, KCl 0.2 g L^{-1}, KH_2PO_4 0.24 g L^{-1} and Na_2HPO_4 1.42 g L^{-1}) was considered as electrolyte. As the working, counter, and reference electrodes, respectively, the sample, a platinum wire, and an Ag/AgCl electrode were utilised for electrochemical corrosion testing. The sample was submerged in the electrolyte, and 1800 s of open circuit potentials (OCP) measurements were recorded. A potentiodynamic polarisation test of the sample was carried out after it was submerged in the electrolyte for 30 minutes. Potentiodynamic polarisation curves were captured at a scan rate of 5 mV s^{-1} from -1 to +1 V.

The fabricated samples were analysed using a scanning electron microscope (SEM) for micro-structural analysis. The SEM micrographs of the samples were used to investigate the pore morphology and interconnectivity. Porosity analysis of the porous structures was done using ImageJ software. ImageJ, an open-source image processing tool, plays a vital role in quantifying porosity by effectively separating pores from the material using thresholding and filtering methods. This analytical processing of the SEM micrographs using ImageJ provided the pore structure and porosity

of the samples. The investigation was required to determine the underlying condition of the electrochemical behaviour of the porous structures.

Results and discussion

The manufacturing of porous Ti6Al4V structure offers the possibility of reducing mechanical incompatibility as found in the case of solid components/implants. In addition, the rate at which new bone tissue grows and facilitates bone/implant biological attachment is well-reported for porous structures [53]. However, the main issue with porous metallic structures as implants is their corrosion behaviour [54]. Previous research demonstrated that the amount, form, and distribution of pores had an impact on how well porous materials resist corrosion [33,55]. The body fluid is a complex electrolyte medium that contains several agents, including chloride, that are erosive to metallic implants. Metal ions resulting from degradation by erosion inside the human body may impair the bones' and the surrounding tissues' ability to heal.

The influence of compaction pressure variation in the fabrication of porous metallic structures has been investigated in the context of electrochemical corrosion. The open circuit potential (OCP) curves of Ti6Al4V porous structures fabricated using different levels of compaction pressure as a function of immersion time are shown in Figure 1. The OCP curves of samples Ti6Al4V-500, Ti6Al4V-400 and Ti6Al4V-300 are seen to shift towards positive potential values with increasing time; this behaviour suggests that the oxide is forming on the specimen's surface. These OCP curves closely resemble those displayed by other titanium alloys such as Ti18Nb4Sn [56], Ti30NbXSn [57] and Ti16Nb [36]. Hence, these porous structures follow the titanium alloy typical behaviour of forming a passive protective coating on the exposed surface [58]. The OCP curve for the Ti6Al4V-200 sample shows that with an increase in the soaking period, the potential moved to negative values. A decrease in OCP values represents the dissolvable passive layer, while higher OCP values indicate the creation of a thicker oxide layer [59]. Hence, from the OCP curves of all four samples, it can be determined that the surface passive layer on Ti6Al4V porous structures, fabricated using higher values of compaction pressure, is found to be more stable.

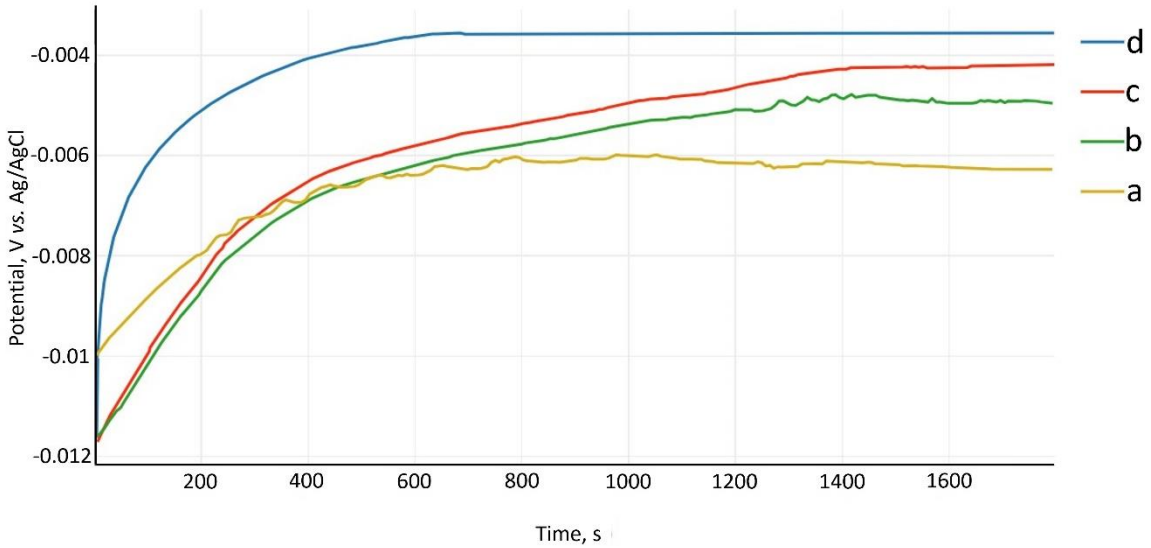

Figure 1. *OCP curves of samples (a) Ti6Al4V-200, (b) Ti6Al4V-300, (c) Ti6Al4V-400 and (d) Ti6Al4V-500*

The electrochemical polarization curves for the four samples are shown in Figure 2. The passivation capabilities of the Ti6Al4V-500, Ti6Al4V-400 and Ti6Al4V-300 porous samples were observed from the anodic polarisation curve. Due to either the heterogeneous structure of the

passive layer that formed on the inner surfaces of the pores or the absence of thickening of the generated passive layer, the Ti6Al4V-200 porous samples did not exhibit a clearly defined passivation plateau. According to Alves *et al*. [60], the rate of passive layer production for inner pores may vary.

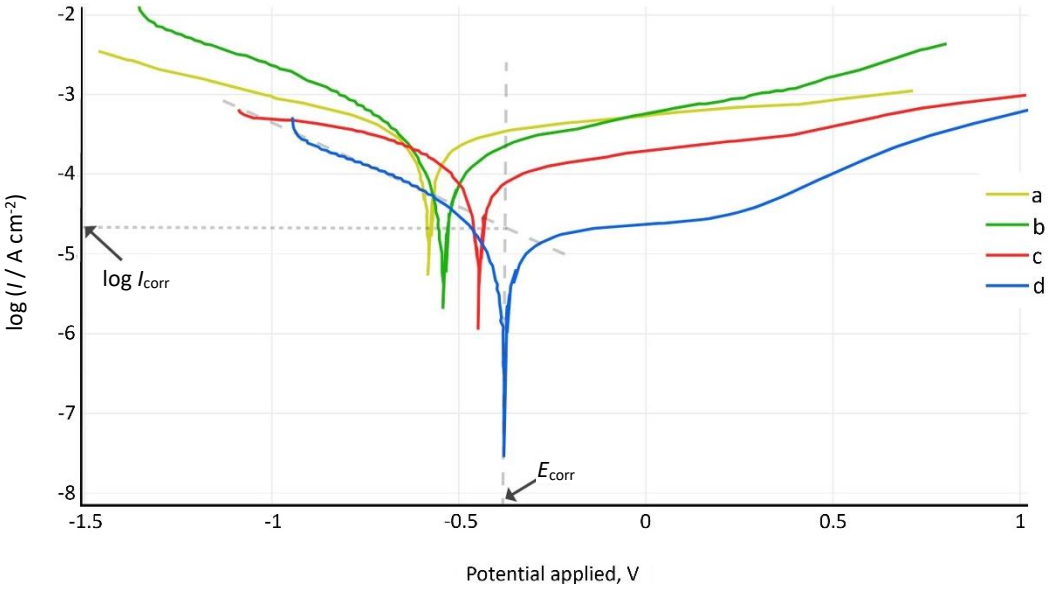

Figure 2. *Potentiodynamic polarization curves of samples (a) Ti6Al4V-200, (b) Ti6Al4V-300, (c) Ti6Al4V-400 and (d) Ti6Al4V-500 (with* E_{corr} *and* I_{corr} *interpretation)*

It is a known fact that porous structures exhibit poorly defined anodic Tafel area due to the dissolution reaction that occurs in the anodic polarisation curves prior to the passivation reaction [61]. Hence, the values of corrosion current density (I_{corr}) are extracted using the Tafel extrapolation method from the cathodic polarisation curves [41,44], as shown for a curve in Figure 2 (curve d).

The values of corrosion potential (E_{corr}) and I_{corr} are enlisted in Table 3. A lower value of I_{corr} and a more positive E_{corr} indicate better anticorrosion performance [62,63]. The findings showed that decreasing compaction pressure causes corrosion resistance to diminish. For powder metallurgy fabricated structures, it is a fact that increased compaction pressure results in increased powder-particle contact area, which lowers porosity [64]. It is possible that the greater surface area of the porous structure is the primary cause of diminished corrosion resistance. According to the reports, porous alloys are more susceptible to corrosion because their large surface area is exposed to the electrolyte [60]. Hence, it is important to investigate the microstructure of the samples.

Table 3. Values of E_{corr} *and* I_{corr} *for samples as per Tafel analysis.*

Sample	I_{corr}, $\mu A\ cm^{-2}$	E_{corr}, V
Ti6Al4V-200	*384*	*-0.58*
Ti6Al4V-300	*301*	*-0.54*
Ti6Al4V-400	*120*	*-0.44*
Ti6Al4V-500	*23*	*-0.36*

SEM pictures of the sintered Ti6Al4V porous structures are shown in Figure 3. The microstructure of the porous sample fabricated using a compaction pressure of 200 MPa (Figure 3(a)) is characterized by loosely packed powder along with large interconnected pores formed by the removal of space holder particles. The pore walls are irregular and indicate relatively poor compaction of metallic powder particles around the space holder powder particle during compaction.

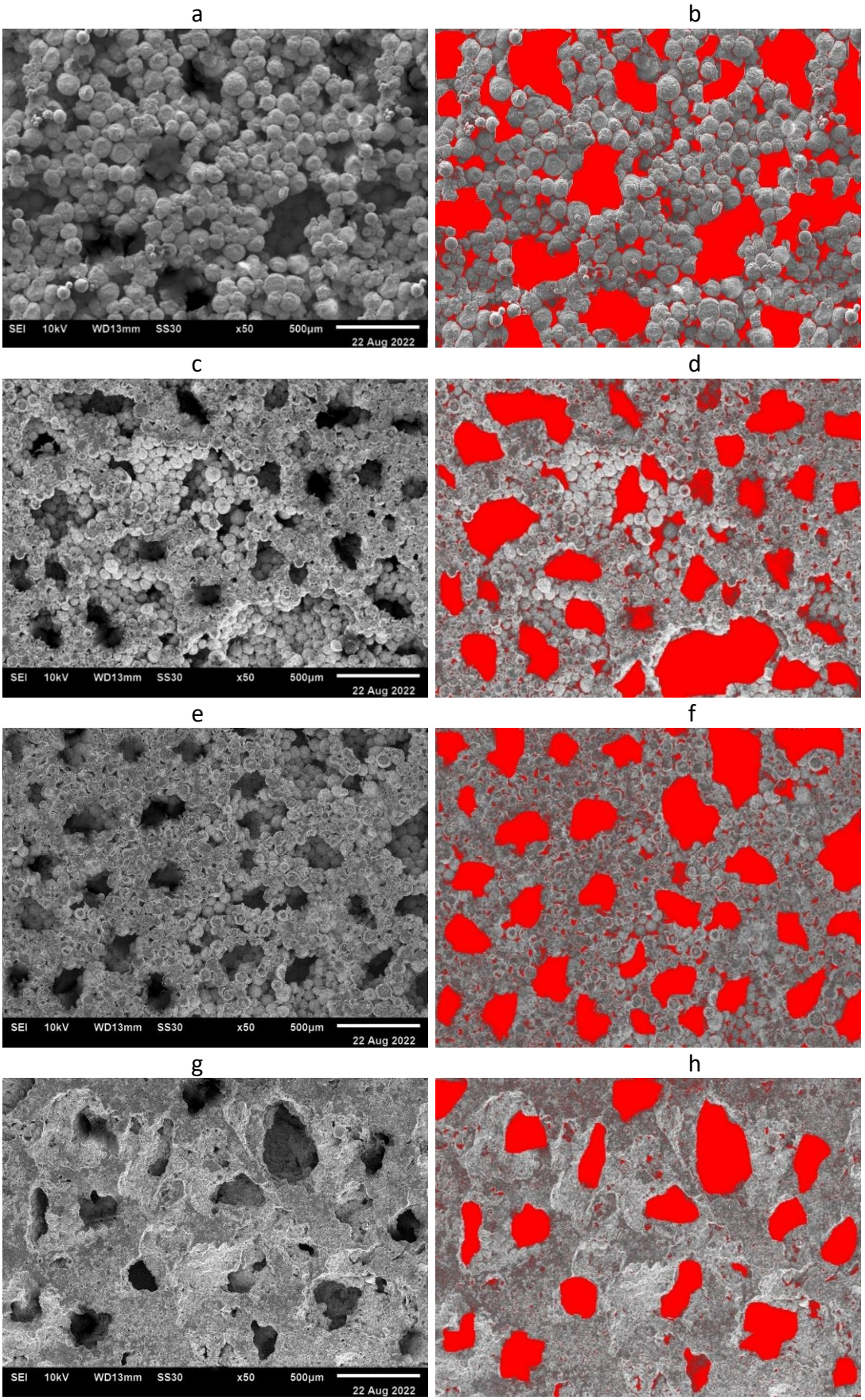

Figure 3. *(a) SEM micrograph of Ti6Al4V-200, (b) 2D image of Ti6Al4V-200 for Porosity analysis, (c) SEM micrograph of Ti6Al4V-300, (d) 2D image of Ti6Al4V-300 for porosity analysis, (e) SEM micrograph of Ti6Al4V-400, (f) 2D image of Ti6Al4V-400 for porosity analysis, (g) SEM micrograph of Ti6Al4V-500, and (h) 2D image of Ti6Al4V-500 for porosity analysis*

Powder-to-powder contact points are less and only a few necking points are visible for a powder particle. As the compaction pressure increases, the difference in powder particle packing is quite distinguishable in Figure 3 (a, c, e and g). With the increase in compaction pressure, the increase in homogeneity of distribution of metal particles around the space holder particle site and the increase in contact points are clearly visible. Figure 3(g) shows the densely packed and effectively sintered metal structure with well-defined pores formed by the thermal disintegration of the space holder.

In order to investigate the nature and distribution of porosity in these samples, the SEM images are further investigated using image processing software, ImageJ. The 2D images of the samples are shown in Figure 3(b, d, f and h). From these images, microporosity and macroporosity in the samples can be confirmed. The presence of microporosity is a characteristic of the powder metallurgy process. However, the macroporosity is deliberately obtained by removing space holder particles. It is evident from Figure 3(b) that in addition to macroporosity, microporosity is present in abundance for sample Ti6Al4V-200. Lower compaction pressure results in an uneven distribution of metal powder particles around the space holder material, leading to a reduced overall powder particle packing. Consequently, uneven distribution and larger pores emerge within the material's structure. Reduction in micro-porosity can be observed in Figure 3 (d, f and h) as the compaction pressure is enhanced. The porous sample fabricated using a compaction pressure of 500 MPa (Figure 3(h)) may be characterized by a significant reduction in microporosity. Also, the micropores are comparatively small and isolated.

From Figure 3 it can be concluded that the increase in compaction pressure leads to a finer and more homogeneous microstructure, resulting in reduced micropore size and the formation of a denser material. Further, a higher level of interconnected porosities in the sample Ti6Al4V-200 and -300 may trap the electrolyte and result in local corrosion. Individual studies by Fojt et al. and Li et al. reported similar observations with other titanium alloys. According to reports, alloys with a high level of interconnected porosity level can create adequate room for electrolyte to be captured and cause crevice corrosion [33,55]. Xie *et al*. [65] highlighted that for porous titanium alloy, the corrosion behaviour is influenced more by the microstructure than by the concentration of the alloying element. Thus, the results indicated that a higher compaction pressure (>300 MPa) must be considered for fabricating porous structures for bone implant applications or other biomedical applications.

Conclusions

This study investigates the effect of compaction pressure on the electrochemical corrosion behaviour of Ti6Al4V porous structures fabricated by the powder metallurgy process. Ti6Al4V is among the Ti alloys most frequently utilised in biomechanical applications (prostheses and implants). Microstructure and pore analysis revealed that both microporosity and macroporosity, as desired for a porous metallic structure for biomedical implant application, can be achieved by powder metallurgy process using the space holder technique. However, with the decrease in compaction pressure lower electrochemical corrosion resistance was observed. The higher level of interconnected micropores in the sample fabricated using a compaction pressure of 200 MPa has been attributed to its inability to attain passivity against electrochemical corrosion. Other levels of compaction pressure (300, 400 and 500 MPa) have shown satisfactory results and may be used for further investigations, which must include investigation of anodic layers formed on the surface of inner pores in terms of homogeneity, composition and morphology in relation to micro- and microporosity is required.

***Conflicts of interest**: The authors declare no conflicts of interest.*

References

[1] S. Tamilselvi, V. Raman, N. Rajendran, Evaluation of corrosion behavior of surface modified Ti-6Al-4V ELI alloy in hanks solution, *Journal of Applied Electrochemistry* **40** (2010) 285-293. https://doi.org/10.1007/s10800-009-9972-5

[2] C. D. Arrieta-González, J. Porcayo-Calderon, V. M. Salinas-Bravo, J. G. Chacon-Nava, A. Martinez-Villafañe. J. G. Gonzalez-Rodriguez, Corrosion behavior of Ni-Cr based coatings in simulated human body fluid environment, *International Journal of Electrochemical Science* **6** (2011) 3644-3655. https://doi.org/10.1016/S1452-3981(23)18277-0

[3] American Joint Replacement Registry, Annual Report on Hip and Knee Arthroplasty Data, 2018. https://www.wavespartnership.org/sites/waves/files/kc/WAVESAnnual-Report-2018-web_0.pdf (accessed 19. 09. 2023)

[4] L. H. Nguyen, N. Annabi, M. Nikkhah, H. Bae, L. Binan, S. Park, Y. Kang, Y. Yang, A. Khademhosseini, Vascularized bone tissue engineering: approaches for potential improvement, *Tissue Engineering B* **18(5)** (2012) 363-382. https://doi.org/10.1089/ten.teb.2012.0012

[5] N. N. Znamenski, Implantation künstlicher zähne, *Deutsche Monatsschrift für Zahnheilkunde* **9** (1891) 87-107.

[6] H. T. Hillischer, Implantation künstlicher Zähne nach dr. Znamensky, *Deutsche Monatsschrift für Zahnheilkunde* **9** (1891) 158-167.

[7] R. E. Payne, Implantation of tin capsule by spreading, *Items of Interest* **14** (1902) 125-226

[8] S. Limmahakhun, A. Oloyede, N. Chantarapanich, P. Jiamwatthanachai, K. Sitthiseripratip, Y. Xiao, C. Yan, Alternative designs of load−sharing cobalt chromium graded femoral stems, *Materials Today Communications* **12** (2017) 1-10. https://doi.org/10.1016/j.mtcomm.2017.05.002

[9] S. Wang, L. Liu, K. Li, L. Zhu, J. Chen, Y. Hao, Pore functionally graded Ti6Al4V scaffolds for bone tissue engineering application, *Materials & Design* **168** (2019) 107643. https://doi.org/10.1016/j.matdes.2019.107643

[10] D. M. D. Ehrenfest, P. G. Coelho, B. S. Kang, Y. T. Sul, T. Albrektsson, Classification of osseointegrated implant surfaces: materials, chemistry and topography, *Trends in Biotechnology* **28(4)** (2010) 198-206. https://doi.org/10.1016/j.tibtech.2009.12.003

[11] C. Song, L. Liu, Z. Deng, H. Lei, F. Yuan, Y. Yang, Y. Li, J. Yu, Research progress on the design and performance of porous titanium alloy bone implants, *Journal of Materials Research and Technology* **23** (2023) 2626-2641. https://doi.org/10.1016/j.jmrt.2023.01.155

[12] C. E. Misch, Contemporary implant dentistry, *Implant Dentistry* **8(1)** (1999) 90. https://journals.lww.com/implantdent/citation/1999/01000/contemporary_implant_dentistry.13.aspx

[13] J. Bartoníček, Early history of operative treatment of fractures, *Archives of Orthopaedic and Trauma Surgery* **130** (2010) 1385-1396. https://doi.org/10.1007/s00402-010-1082-7

[14] S. S. Abdalla, H. Katas, F. Azmi, M .F. M. Busra, Antibacterial and anti-biofilm biosynthesised silver and gold nanoparticles for medical applications: Mechanism of action, toxicity and current status, *Current Drug Delivery* **17(2)** (2020) 88-100. https://doi.org/10.2174/1567201817666191227094334

[15] G. Szczęsny, M. Kopec, D. J. Politis, Z. L. Kowalewski, A. Łazarski, T. Szolc, A review on biomaterials for orthopaedic surgery and traumatology: From past to present, *Materials* **15(10)** (2022) 3622. https://doi.org/10.3390/ma15103622

[16] H. R. Bakhsheshi-Rad, E. Hamzah, H. T. Low, M. Kasiri-Asgarani, S. Farahany, E. Akbari, M. H. Cho, Fabrication of biodegradable Zn-Al-Mg alloy: mechanical properties, corrosion behavior, cytotoxicity and antibacterial activities, *Materials Science and Engineering C* **73** (2017) 215-219. https://doi.org/10.1016/j.msec.2016.11.138

[17] N. El-Mahallawy, H. Palkowski, A. Klingner, A. Diaa, M. Shoeib, Effect of 1.0 wt.% Zn addition on the microstructure, mechanical properties, and bio-corrosion behaviour of micro alloyed Mg-0.24 Sn-0.04 Mn alloy as biodegradable material, *Materials Today Communications* **24** (2020) 100999. https://doi.org/10.1016/j.mtcomm.2020.100999
[18] D. I. Bardos, *Metallurgy of orthopaedic implants* in *Materials Sciences and Implant Orthopedic Surgery,* R. Kossowsky, N. Kossovsky, Eds., Springer, Dordrecht, Netherlands, 1986, p.125. https://doi.org/10.1007/978-94-009-4474-9_11
[19] D. Shekhawat, A. Singh, A. Bhardwaj and A. Patnaik. A short review on polymer, metal and ceramic based implant materials, *IOP Conference Series: Materials Science and Engineering* **1017(1)** (2021) 012038. https://doi.org/10.1088/1757-899X/1017/1/012038
[20] A. Sumayli. Recent trends on bioimplant materials, *Materials Today: Proceedings* **46** (2021) 2726-2731. https://doi.org/10.1016/j.matpr.2021.02.395
[21] J. A. Planell, M. Navarro, *Challenges of bone repair*, in *Bone repair biomaterials*, J. A. Planell, S. M. Best, Eds., Woodhead Publishing Limited, Cambridge, UK, 2009, p.3. https://doi.org/10.1533/9781845696610.1.3
[22] G. A. Sargent, A. P. Zane, P. N. Fagin, A. K. Ghosh, S. L. Semiatin, Low-temperature coarsening and plastic flow behavior of an alpha/beta titanium billet material with an ultrafine microstructure, *Metallurgical and Materials Transactions* A **39** (2008) 2949-2964. https://doi.org/10.1007/s11661-008-9650-y
[23] A. I. Kahveci, G .E. Welsch, Effect of oxygen on the hardness and alpha/beta phase ratio of Ti6A14V alloy, *Scripta Metallurgica* **20(9)** (1986) 1287-1290. https://doi.org/10.1016/0036-9748(86)90050-5
[24] F. Veronesi, P. Torricelli, L. Martini, M. Tschon, G. Giavaresi, D. Bellini, V. Casagranda, F. Alemani, M. Fini, An alternative ex vivo method to evaluate the osseointegration of Ti-6Al-4V alloy also combined with collagen, *Biomedical Materials* **16(2)** (2021) 025007. https://doi.org/10.1088/1748-605X/abdbda
[25] J. Banhart. Manufacture, characterisation and application of cellular metals and metal foams, *Progress in Materials Science* **46(6)** (2001) 559-632. https://doi.org/10.1016/S0079-6425(00)00002-5
[26] J. Banhart, J. Baumeister, Production methods for metallic foams, *MRS Online Proceedings Library* **521** (1998) 121. https://doi.org/10.1557/PROC-521-121
[27] N. Jha, D. P. Mondal, J. D. Majumdar, A. Badkul, A. K. Jha, A.K. Khare, Highly porous open cell Ti-foam using NaCl as temporary space holder through powder metallurgy route, *Materials & Design* **47** (2013) 810-819. https://doi.org/10.1016/j.matdes.2013.01.005
[28] B. Goyal, A. Pandey, Critical review on porous material manufacturing techniques, properties & their applications, *Materials Today: Proceedings* **46** (2021) 8196-8203. https://doi.org/10.1016/j.matpr.2021.03.163
[29] D. Prando, A. Brenna, M. V. Diamanti, S. Beretta, F. Bolzoni, M. Ormellese, M. Pedeferri. Corrosion of titanium: Part 1: Aggressive environments and main forms of degradation. *Journal of Applied Biomaterials & Functional Materials* **15(4)** (2017) e291-e302. https://doi.org/10.5301/jabfm.5000387
[30] K. H. W. Seah and X. Chen, A comparison between the corrosion characteristics of 316 stainless steel, solid titanium and porous titanium, *Corrosion Science* **34(11)** (1993) 1841-1851. https://doi.org/10.1016/0010-938X(93)90021-8
[31] K. H. W. Seah, R. Thampuran, X. Chen, S.H. Teoh, A comparison between the corrosion behaviour of sintered and unsintered porous titanium, *Corrosion Science* **37(9)** (1995) 1333-1340. https://doi.org/10.1016/0010-938X(95)00033-G

[32] K. H. W. Seah, R. Thampuran, X. Chen, S.H. Teoh, The influence of pore morphology on corrosion, *Corrosion Science* **40** (1998) 547-556. https://doi.org/10.1016/S0010-938X(97)00152-2
[33] J. Fojt, L. Joska, J. Málek, Corrosion behaviour of porous Ti-39Nb alloy for biomedical applications, *Corrosion Science* **71** (2013) 78-83. https://doi.org/10.1016/j.corsci.2013.03.007
[34] A. Rodriguez-Contreras, M. Punset, J. A. Calero, F. J. Gil, E. Ruperez, J. M. Manero, Powder metallurgy with space holder for porous titanium implants, *Journal of Materials Science & Technology* **76** (2021) 129-149. https://doi.org/10.1016/j.jmst.2020.11.005
[35] N. Eliaz, Corrosion of metallic biomaterials, *Materials* **12(3)** (2019) 407. https://doi.org/10.3390/ma12030407
[36] E. Yılmaz, A. Gökçe, F. Findik, H. O. Gulsoy, O. İyibilgin, Mechanical properties and electrochemical behavior of porous Ti-Nb biomaterials, *Journal of the Mechanical Behavior of Biomedical Materials* **87** (2018) 59-67. https://doi.org/10.1016/j.jmbbm.2018.07.018
[37] R. Khalifehzadeh, S. Forouzan, H. Arami, S. K. Sadrnezhaad, Prediction of the effect of vacuum sintering conditions on porosity and hardness of porous NiTi shape memory alloy using ANFIS, *Computational Materials Science* **40(3)** (2007) 359-365. https://doi.org/10.1016/j.commatsci.2007.01.007
[38] A. C. Alves, A. I. Costa, F. Toptan, J. L. Alves, I. Leonor, E. Ribeiro, R. L. Reis, A. M. P. Pinto, J. C. S . Fernandes, Effect of bio-functional MAO layers on the electrochemical behaviour of highly porous Ti, *Surface and Coatings Technology* **386** (2020) 125487. https://doi.org/10.1016/j.surfcoat.2020.125487
[39] H. J. Vergara-Hernández, L Olmos, V. M. Solorio, D. Bouvard, J. Villalobos-Brito, J. Chávez, O. Jimenez, Powder Metallurgy Fabrication and Characterization of Ti6Al4V/xCu Alloys for Biomedical Applications, *Metals* **13(5)** (2023) 888. https://doi.org/10.3390/met13050888
[40] L. M. Rodriguez-Albelo, P. Navarro, F. J. Gotor, J. E. de la Rosa, D. Mena, F. J. García-García, A. M. Beltrán, A. Alcudia, Y. Torres, Limits of powder metallurgy to fabricate porous Ti35Nb7Zr5Ta samples for cortical bone replacements, *Journal of Materials Research and Technology* **24** (2023) 6212-6226. https://doi.org/10.1016/j.jmrt.2023.04.212
[41] W. Xu, X. Lu, B. Zhang, C. Liu, S. Lv, S. Yang, X. Qu, Effects of porosity on mechanical properties and corrosion resistances of PM-fabricated porous Ti-10Mo alloy, *Metals* **8(3)** (2018) 188. https://doi.org/10.3390/met8030188
[42] J. Z. Carrullo, A. D. Borrás, V. A. Borrás, J. Navarro-Laboulais, J. P. Falcón, Electrochemical corrosion behavior and mechanical properties of Ti-Ag biomedical alloys obtained by two powder metallurgy processing routes, *Journal of the Mechanical Behavior of Biomedical Materials* **112** (2020) 104063. https://doi.org/10.1016/j.jmbbm.2020.104063
[43] G. Dercz, I. Matuła, M. Zubko, A. Kazek-Kęsik, J. Maszybrocka, W. Simka, J. Dercz, P. Świec, I. Jendrzejewska, Synthesis of porous Ti-50Ta alloy by powder metallurgy, *Materials Characterization* **142** (2018) 124-136. https://doi.org/10.1016/j.matchar.2018.05.033
[44] W. Xu, X. Lu, M.D. Hayat, J. Tian, C. Huang, M. Chen, X. Qu, C. Wen, Fabrication and properties of newly developed Ti35Zr28Nb scaffolds fabricated by powder metallurgy for bone-tissue engineering, *Journal of Materials Research and Technology* **8(5)** (2019) 3696-3704. https://doi.org/10.1016/j.jmrt.2019.06.021
[45] I. Çaha, A. Alves, C. Chirico, A. Pinto, S. Tsipas, E. Gordo, F. Toptan, Corrosion and tribocorrosion behavior of Ti-40Nb and Ti-25Nb-5Fe alloys processed by powder metallurgy, *Metallurgical and Materials Transactions* A **51** (2020) 3256-3267. https://doi.org/10.1007/s11661-020-05757-6
[46] S. A. Tsipas, E. Gordo. A. Jiménez-Morales, Oxidation and corrosion protection by halide treatment of powder metallurgy Ti and Ti6Al4V alloy, *Corrosion Science* **88** (2014) 263-274. https://doi.org/10.1016/j.corsci.2014.07.037

[47] M. P. I. Federation, *Standard test methods for metal powders and powder metallurgy products*, Metal Powder Industries Federation, Princeton, USA, 2019.
[48] Z. Chen, X. Yan, S. Yin, L. Liu, X. Liu, G. Zhao, W. Ma, W. Qi, Z. Ren, H. Liao, M. Liu, Influence of the pore size and porosity of selective laser melted Ti6Al4V ELI porous scaffold on cell proliferation, osteogenesis and bone ingrowth, *Materials Science and Engineering* C **106** (2020) 110289. https://doi.org/10.1016/j.msec.2019.110289
[49] C. M. Murphy, F.J. O'Brien, Understanding the effect of mean pore size on cell activity in collagen-glycosaminoglycan scaffolds, *Cell Adhesion & Migration* **4(3)** (2010) 377-381. https://doi.org/10.4161/cam.4.3.11747
[50] P. Ouyang, H. Dong, X. He, X. Cai, Y. Wang, J. Li, H. Li, Z. Jin, Hydromechanical mechanism behind the effect of pore size of porous titanium scaffolds on osteoblast response and bone ingrowth, *Materials & Design* **183** (2019) 108151. https://doi.org/10.1016/j.matdes.2019.108151
[51] S. Lu, D. Jiang, S. Liu, H. Liang, J. Lu, H. Xu, J. Li, J. Xiao, J. Zhang, Q. Fei, Effect of different structures fabricated by additive manufacturing on bone ingrowth, *Journal of Biomaterials Applications* **36(10)** (2022) 1863-1872. https://doi.org/10.1177/08853282211064398
[52] J. P. Zheng, L. J. Chen, D. Y. Chen, C. S. Shao, M. F. Yi, B. Zhang, Effects of pore size and porosity of surface-modified porous titanium implants on bone tissue ingrowth, *Transactions of Nonferrous Metals Society of China* **29(12)** (2019) 2534-2545. https://doi.org/10.1016/S1003-6326(19)65161-7
[53] N. Abbasi, S. Hamlet, R. M. Love, N.T. Nguyen. Porous scaffolds for bone regeneration. *Journal of Science: Advanced Materials and Devices* **5(1)** (2020) 1-9. https://doi.org/10.1016/j.jsamd.2020.01.007
[54] P. Du, T. Xiang, Z. Cai, G. Xie, The influence of porous structure on the corrosion behavior and biocompatibility of bulk Ti-based metallic glass, *Journal of Alloys and Compounds* **906** (2022) 164326. https://doi.org/10.1016/j.jallcom.2022.164326
[55] Y. H. Li, G. B. Rao, L. J. Rong, Y. Y. Li, The influence of porosity on corrosion characteristics of porous NiTi alloy in simulated body fluid, *Materials Letters* **57(2)** (2002) 448-451. https://doi.org/10.1016/S0167-577X(02)00809-1
[56] F. Rosalbino, D. Maccio, G. Scavino, A. Saccone, In vitro corrosion behaviour of Ti-Nb-Sn shape memory alloys in Ringer's physiological solution, *Journal of Materials Science: Materials in Medicine* **23** (2012) 865-871. https://doi.org/10.1007/s10856-012-4560-3
[57] P. E. Moraes, R. J. Contieri, E. S. Lopes, A. Robin, R. Caram, Effects of Sn addition on the microstructure, mechanical properties and corrosion behavior of Ti-Nb-Sn alloys, *Materials Characterization* **96** (2014) 273-281. https://doi.org/10.1016/j.matchar.2014.08.014
[58] J. Xu, W. Hu, S. Xu, P. Munroe, Z.H. Xie, Electrochemical properties of a novel β-Ta_2O_5 nanoceramic coating exposed to simulated body solutions, *ACS Biomaterials Science & Engineering* **2(1)** (2016) 73-89. https://doi.org/10.1021/acsbiomaterials.5b00384
[59] K. Li, Y. Li, X. Huang, D. Gibson, Y. Zheng, J. Liu, L. Sun, Y.Q. Fu, Surface microstructures and corrosion resistance of Ni-Ti-Nb shape memory thin films, *Applied Surface Science* **414** (2017) 63-67. https://doi.org/10.1016/j.apsusc.2017.04.070
[60] A. C. Alves, I. Sendão, E. Ariza, F. Toptan, P. Ponthiaux, A. M. P. Pinto, Corrosion behaviour of porous Ti intended for biomedical applications, *Journal of Porous Materials* **23** (2016) 1261-1268. https://doi.org/10.1007/s10934-016-0185-0
[61] E. McCafferty. Validation of corrosion rates measured by the Tafel extrapolation method. *Corrosion Science* **47(12)** (2005) 3202-3215. https://doi.org/10.1016/j.corsci.2005.05.046
[62] L. L. Liu, J. Xu, X. Lu, P. Munroe, Z. H. Xie, Electrochemical corrosion behavior of nanocrystalline β-Ta coating for biomedical applications, *ACS Biomaterials Science & Engineering* **2(4)** (2016) 579-594. https://doi.org/10.1021/acsbiomaterials.5b00552

[63] Q. Liu, D. Chen, Z. Kang, One-Step electrodeposition process to fabricate corrosion-resistant superhydrophobic surface on magnesium alloy, *ACS Applied Materials Interfaces* **7(3)** (2015) 1859-1867. https://doi.org/10.1021/am507586u

[64] A. S. Jabur, Effect of powder metallurgy conditions on the properties of porous bronze, *Powder Technology* **237** (2013) 477-483. https://doi.org/10.1016/j.powtec.2012.12.027

[65] F. Xie, X. He, S. Cao, M. Mei, X. Qu, Influence of pore characteristics on microstructure, mechanical properties and corrosion resistance of selective laser sintered porous Ti-Mo alloys for biomedical applications, *Electrochimica Acta* **105** (2013) 121-129. https://doi.org/10.1016/j.electacta.2013.04.105

J. Electrochem. Sci. Eng. **14(4)** (2024) 487-498; http://dx.doi.org/10.5599/jese.2140

Open Access : : ISSN 1847-9286
www.jESE-online.org

Original scientific paper

The solid particle erosion performance of tungsten inert gas yttria-stabilized zirconia - Inconel 625 composite cladding

Neeraj Kamboj[1,✉], Lalit Thakur[1] and Manpreet Kaur Arora[2]

[1]*Mechanical Engineering Department, National Institute of Technology,Kurukshetra, Haryana, 136119, India*

[2]*Mechanical Engineering Department, Baba Banda Singh Bahadur Engineering College, Fatehgarh Sahib, Punjab,140407, India*

Corresponding authors: ✉*neeraj_6180090@nitkkr.ac.in*

Received: October 20, 2023; Accepted: February 4, 2024; Published: March 4, 2024

Abstract

The yttria-stabilized zirconia (YSZ) - Inconel 625 (IN625) composite cladding was deposited on a stainless steel substrate using a tungsten inert gas welding manipulator to protect it from solid particle erosion. Erosion wear tests were carried out at room temperature according to the ASTM G76-18 procedure. The surface of the tested material was exposed to a jet of alumina erodent particles at impact angles of 30 and 90°, respectively. Scanning electron microscopy images were utilized to examine the morphologies of the eroded surface and the microstructure of cladding. The erosive performance of YSZ - IN625 composite cladding was 3.5 and 2.4 times compared to the substrate at different impact angles. Improved microhardness and fracture toughness resulting from the favourable interaction between the hard ceramic YSZ particles and the IN625 matrix led to the enhanced erosion performance of composite cladding. Micro-cutting and ploughing were the predominant wear mechanisms in the substrate during the solid particle erosion test at a 30° impact angle, whereas the indentation-induced plastic deformation was dominant at a 90° impact angle. The results also revealed that the micro-cutting, detached splats and fissures were responsible for the wear in composite cladding at 30 and 90° impact angles.

Keywords

Air jet erosion; hardness; fracture toughness; wear

Introduction

The deterioration of materials is a crucial concern for all manufacturing industries. Materials degradation often causes complete system failure. Abrasion, adhesion, corrosion, erosion, and surface fatigue are the most frequent types of wear that cause components to degrade. Abrasive, adhesive, and erosion wear are the primary types that significantly affect the financial losses and

maintenance costs of the various components. Erosion induced by impinging hard microscopic particles poses a significant challenge in petrochemical, turbine blades and food processing industries [1]. These industries' mechanical components must be protected on their working surfaces to prevent early failure [2,3]. Consequently, wear-resistant alloys or coatings are advised to counteract the erosion problems. The use of protective coating is a cost-effective approach to protect the components because the alloys with excellent wear and corrosive properties are very costly and always find difficulty in processing into some working component [4].

The tungsten inert gas (TIG) weld cladding process has become more popular in creating wear-resistant coatings compared to other surface modification techniques such as laser, electron beam and thermal spraying [5-8]. The high temperature and constrained cladding thickness are significant issues with thermal spray coatings. The TIG weld cladding method aims to achieve the desired mechanical and tribological capabilities by changing the composition and microstructure of the substrate surface without compromising the bulk properties [9,10]. Ni-based alloy claddings developed using the TIG weld cladding technique have demonstrated exceptional performance against wear at room and elevated temperatures [11-13]. It is well known that Ni-based alloys have several advantages, including high hardness, enhanced wear and erosion resistance. Additionally, alloys composed of nickel with high chromium concentrations are frequently used as corrosion-resistant coating materials owing to their remarkable resistance to oxidation and corrosion [14-16]. The TIG weld cladding can effectively protect the underlying substrate by producing a protective chromium oxide layer at high temperatures. These Cr_2O_3 protective oxide layers are stable, which creates a thick, continuous, and adherent layer that prevents the oxygen from contacting the coating or underlying substrate [7,17].

One study examined the erosion behaviour of 73Ni-13Cr-4Sn-4Bi-Mo alloy. The results showed that the material's erosive resistance is strongly correlated with the impact energy and velocities of the erodent [18]. Another research looked at how impact angle and testing duration affected the erosion of stainless steel (s.s.) at higher velocities. It found that the maximum depth of cut increased as the testing duration increased and peaked at an impact angle of 40°. At low-impact angles, the indentation-induced plastic deformation mechanism was dominant, but at high-impact angles, the micro-cutting/ploughing mechanism was predominant [19,20]. In an additional investigation, the behaviour of solid particle erosion in tungsten carbide (WC)-reinforced Ni-matrix-based laser-clad layers was examined to enhance the engineering components' performance for possible power plant applications. The findings showed that impact angle and erodent jet velocity are the main factors controlling the eroding behaviour of the WC-Ni laser clad. Signature wear at the erosion wear surface showed that ductile erosion processes controlled the erosion mainly, with WC particles being removed from the matrix as a secondary factor [21]. According to different research, micro-cutting and micro-fissuring were the main processes for the generation of mass losses during solid particle erosion in the erosive wear of Inconel 625 alloy coatings applied using the cold metal transfer (CMT) technique [22].

The inclusion of different ceramics like TiC, SiC, WC, Al_2O_3, etc., has established new upper limits for corrosion, oxidation, erosion, and wear resistance of Ni-based alloys [23-26]. The yttria-stabilized zirconia (YSZ) ceramic material is increasingly used for room and high-temperature environments where it exhibits high corrosion and wear resistance because it generates a solidly adherent ZrO_2 surface film [23,27-29]. The prevention of ferrous alloys (carbon and stainless steel) components in various industries from solid erosion is an important area of research. In this research, 304 stainless steel substrates were cladded with Inconel 625 + YSZ (25 wt.%) powder using the TIG weld cladding

process. Claddings' microhardness and fracture toughness have been calculated and compared with the substrate. The erosion behaviour of claddings was assessed using an air jet erosion test machine. The wear mechanism in worn-out claddings was examined using scanning electron microscopy (SEM) images.

Experimental

Materials and tungsten inert gas cladding

The AISI 304 stainless steel with dimensions of 25×25×5 mm was used as the substrate material. In this investigation, Inconel 625 (G.S.P., Mumbai, India) and YSZ (Mincometal, Bengaluru, India) powders with particle sizes of 15-50 and 30-50 µm, respectively, were considered for cladding deposition. The powder Inconel 625 (IN625) SEM images at 500× and 1,000× magnifications are displayed in Figure 1(a-b). The IN625 particles, which range in size from 15 to 50 µm, have a spherical shape. The IN625 powder's energy dispersive spectroscopy (EDS) spectrum is seen in Figure 1c.

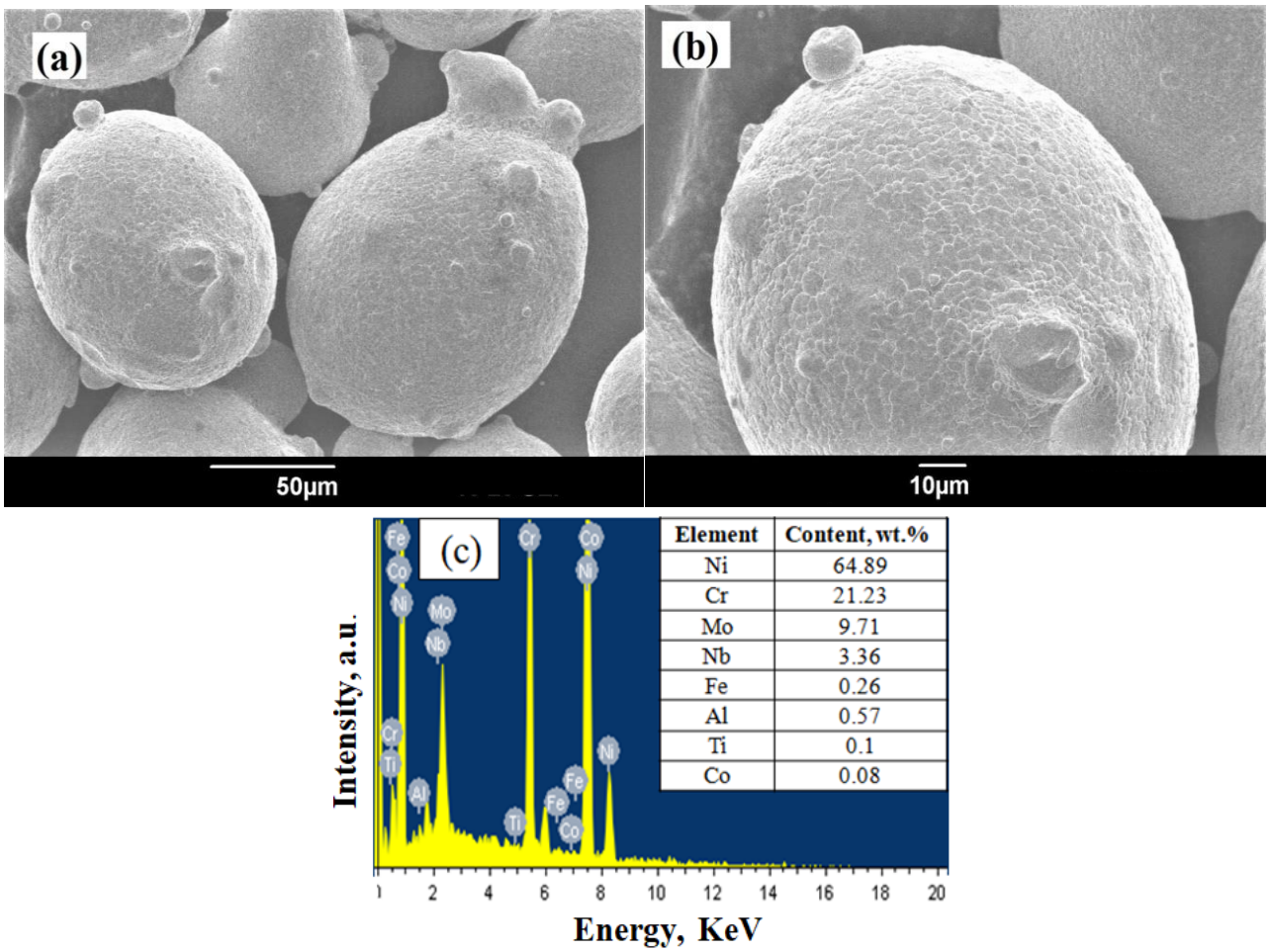

Figure 1. *SEM image of IN625 powder at (a) 500X (b) 1,000X, and (c) EDS spectrum of IN625 powder*

The primary elements found in the IN625 powder, according to EDS, are Ni, Cr, Mo, and Nb. Mechanical mixing of the Inconel 625 and YSZ (25 wt.%) powders was performed in a jar milling machine for 2 h. With this powder and polyvinyl alcohol (PVA. in 10 wt.%) [9] binder, a semisolid paste was created. The Inconel 625-YSZ (25 wt.%) + PVAbinder paste was applied evenly to the specimen's top surface. A 3-axis CNC-controlled TIG welding equipment was used to deposit the Inconel 625-YSZ (25 wt.%) claddings. The optimized process parameters were taken from the authors' previous study and optimized for room temperature wear performance, as indicated in Table 1 [18]. Figure 2 depicts

the process diagram of the TIG weld cladding technique. Figure 3(a-c) displays an SEM image, EDS spectra and XRD of powders containing a mixture of IN625 and YSZ (25 wt. %), respectively.

***Table 1**. TIG weld cladding process parameters used in the present work [23]*

Parameters	Current, A	Welding speed, mm min^{-1}	Standoff distance, mm	YSZ concentration, wt.%
Value	70	192	2	25

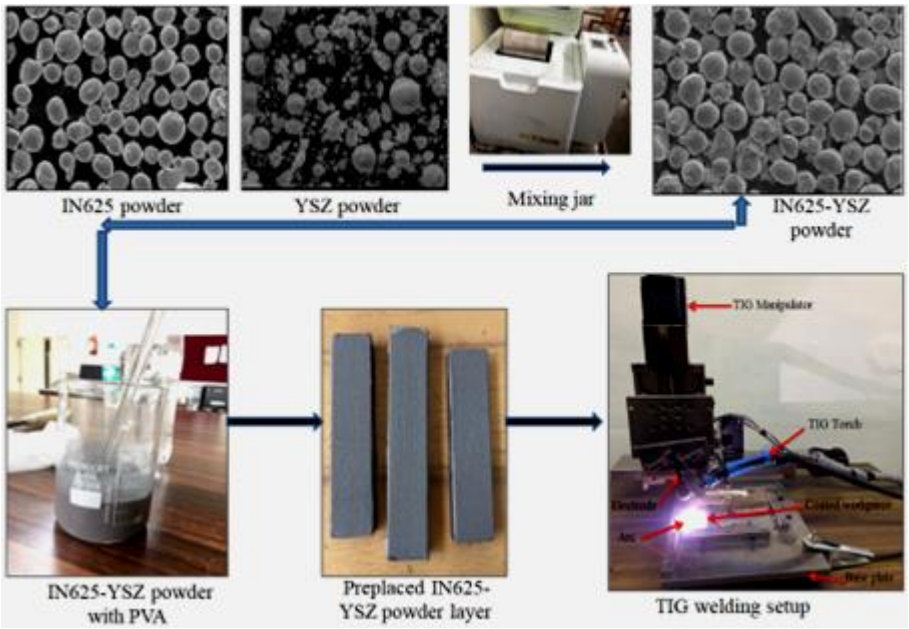

***Figure 2.** Process diagram for the TIG weld cladding*

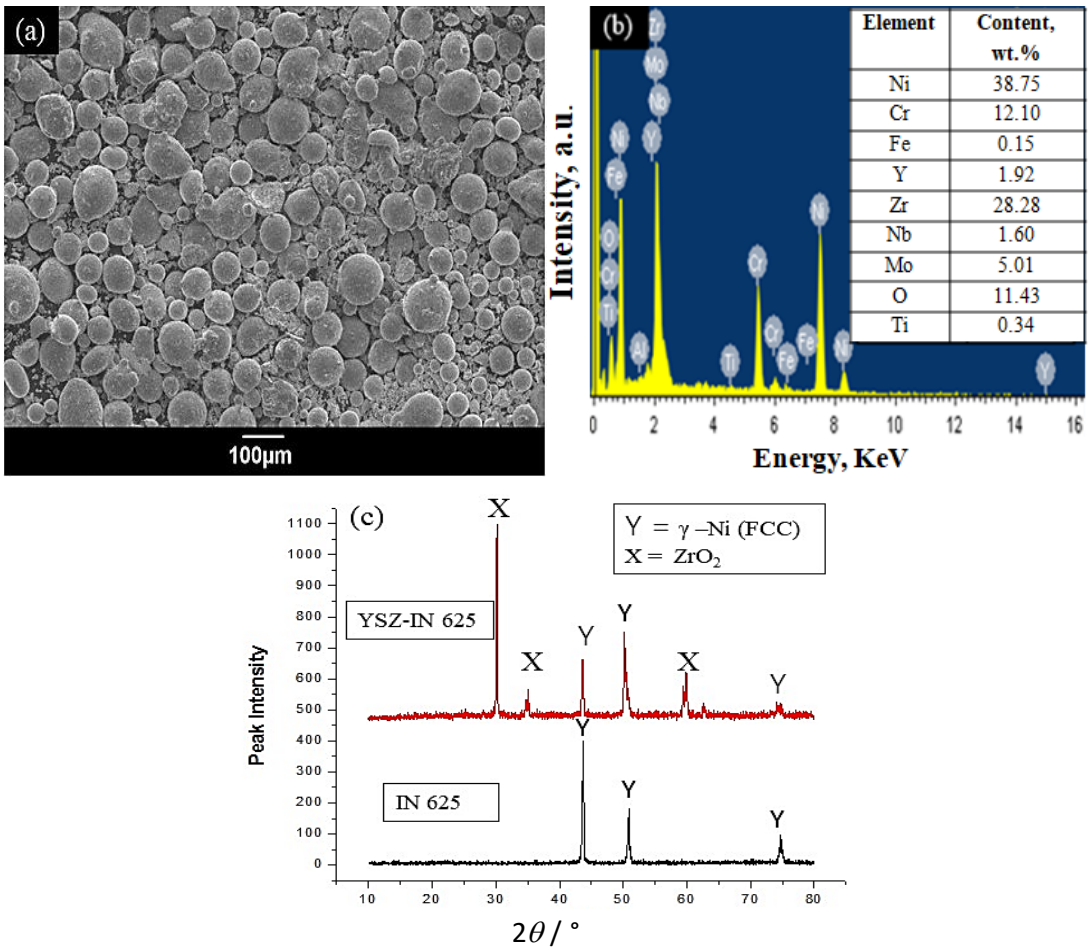

***Figure 3.** (a) SEM image, (b) EDS spectra and (c) XRD of IN625 and YSZ-IN625 powders*

Characterization techniques

A scanning electron microscope (JEOL JSM-6390LV) (SEM) with an energy dispersive spectroscopy (EDS) attachment and optical microscopy (OM) were used to perform the microstructural characterization of the claddings. To achieve a mirror-like polished cross-section and a smooth surface, the cut specimens were polished using emery grades ranging from 200 to 2,000 grit numbers using a double disc-polishing machine (Banbros Engineering Pvt. Ltd., India). An etchant was used to investigate the grain structure of claddings. Etchant was prepared by adding 15 mL HCl, 10 mL acetic acid, and 10 mL HNO_3 and then gently used on a polished surface for 20-30 s. A diffractometer (D8 Advance, Bruker, Germany) with CuKα radiation was used for the XRD analysis to identify the developed phase in the claddings. The cladding's microhardness was measured over the polished cross-section with the help of a Vicker's microhardness tester (XHVT-1000Z, China) at a 300 g load and 15 s dwell time. The mean microhardness value was determined by taking ten indents and reported in the current study. To evaluate the cladding's fracture toughness, ten indents were generated by a Vickers hardness tester through a substantial load of 10 kg. The cladding's fracture toughness was calculated using the Equation (1) [30]:

$$K_{IC} = 0.079\left(\frac{p}{b}\right)^{\frac{3}{2}} \log\left(4.5\frac{b}{z}\right) \quad (1)$$

Here p / kg is load, b / µm is half diagonal length, z / µm is the crack length from the indented centre.

Erosion test

An air erosion test according to ASTM G76-18 was carried out at ambient temperature using an air jet erosion test rig (TR-471-600, DUCOM-Bangalore, India) to investigate the erosion behaviour of the cladding. The working principle and position of the cladding workpiece are illustrated in Figure 4. The testing was performed using the alumina (Al_2O_3) erodent with particle sizes of around 50 µm. Figure 5 displays the SEM image of the alumna erodent used in this research. As per ASTM G7-18 standard, the powder feeding rate was set to 2 g s^{-1}, and the nozzle was placed 10 mm away from the workpiece. To evaluate the erosion behaviour of all samples, tests were conducted at two different angles, 30 and 90° [24,30], respectively. Furthermore, the erodent exposure time was set to 10 minutes.

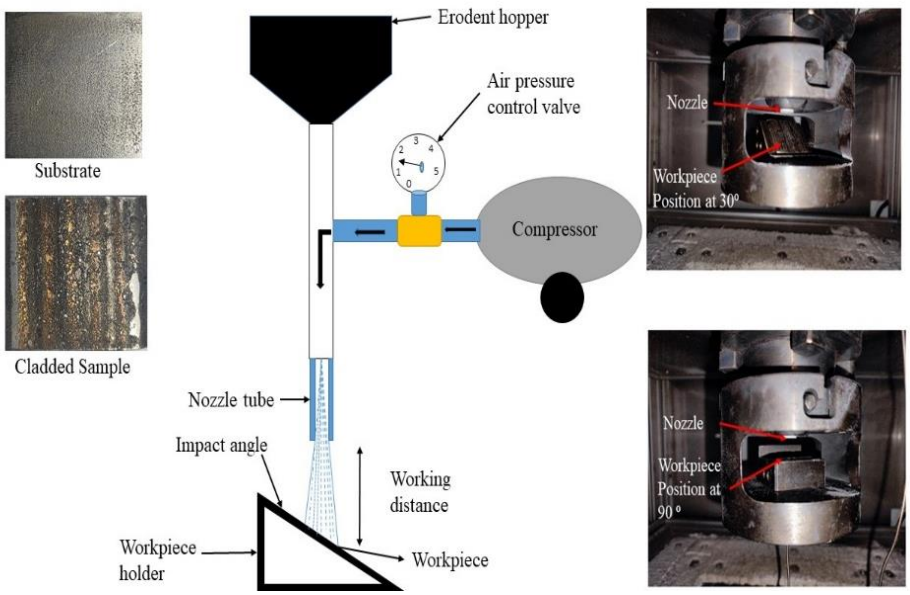

***Figure 4**. Systematic view of air jet erosion testsetup with workpiece positions*

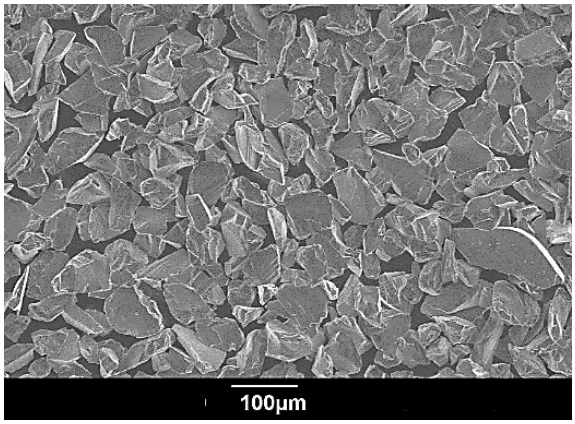

***Figure 5**. SEM image of alumina erodent*

Results and discussion

As-deposited composite cladding characterization

The surface morphology of as-deposited cladding is shown in Figure 6a. The YSZ particles appeared to be immersed in the matrix of IN625. The scattered YSZ particles (mostly partially melted) are consistently dispersed throughout the as-deposited cladding microstructure. Figure 6b-6c shows a cross-sectional SEM image and XRD pattern of the deposited cladding. The SEM image shows appropriate metallurgical bonding between composite cladding and the stainless steel substrate. Moreover, there are no cracks, and a smaller heat-affected zone has been developed in the cladding. XRD image shows a peak of γ- Ni-Cr-Fe along with Cr_2O_3 and ZrO_2 stable oxides phases. Inconel 625 powder primarily comprises Ni, Cr, and Fe elements. Figure 6d shows that cladding exhibited a dense microstructure with significant dendrites and an equiaxed type of grain growth.

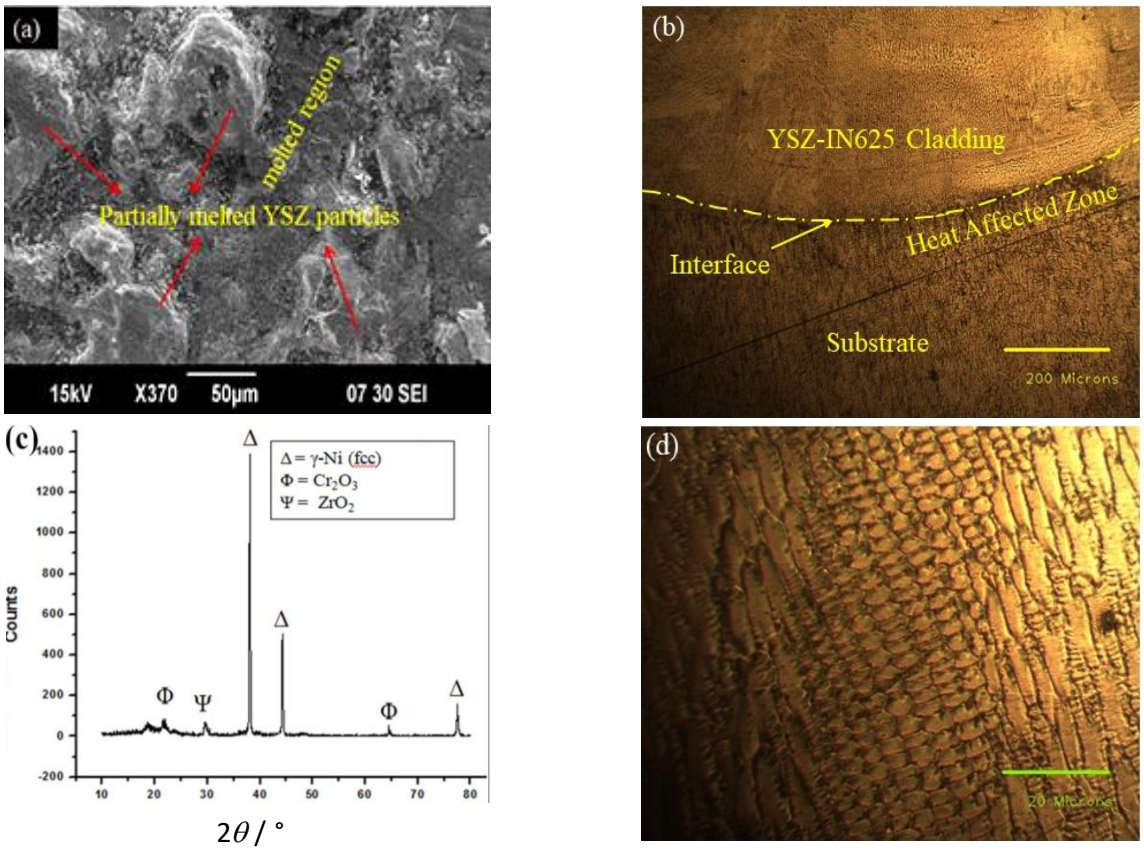

***Figure 6**. (a) SEM image of deposited cladding, (b) Cross-sectional SEM image of cladding along with substrate at lower magnification, (c) XRD, (d) SEM image of cladding at higher magnification*

Figure 7 (a-b) displays the EDS analysis of uncladded (substrate) and cladding samples. As revealed from EDS analysis, the substrate's primary constituents are Fe, Cr, and Ni. In contrast, a rich composition of elements like Ni, Cr, Zr, Mo, Nb and Fe has been observed in the cladding. The increase of Fe in the cladded sample could be explained by the dilution of the substrate matrix, which is essential for good metallurgical bonding with the substrate.

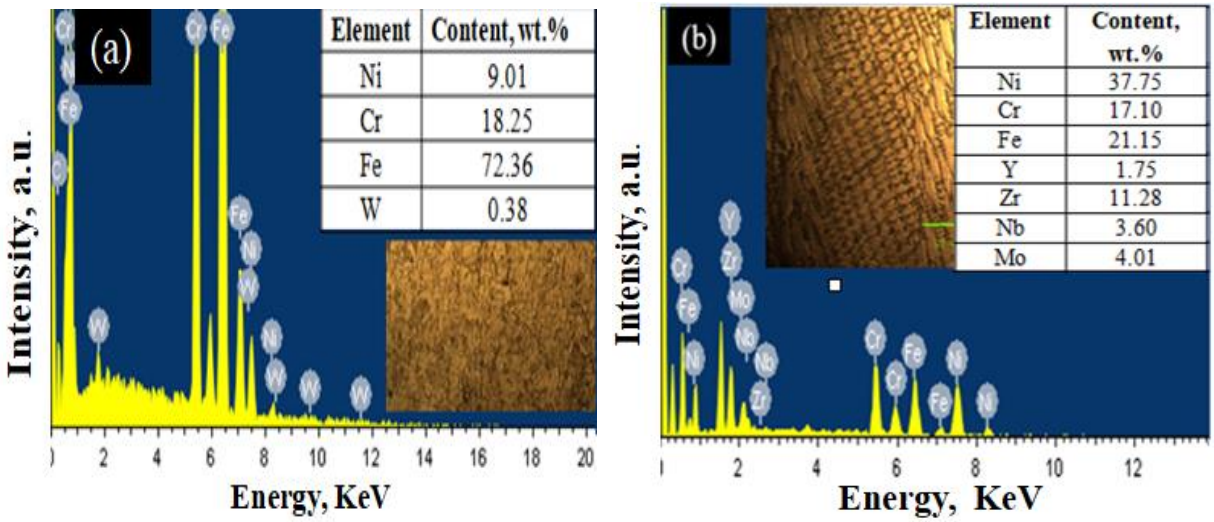

Figure 7. *(a-b) EDS result of uncladded sample (AISI 304 SS substrate) and cladded sample, respectively*

Microhardness and fracture toughness analysis

The microhardness of the substrate and cladding was measured by a Vickers microhardness tester at 300 g load and 15 s dwell time. The average microhardness for the substrate (stainless steel 304) and cladding was found to be 140 ± 5 $HV_{0.3}$ and 330 ± 4 $HV_{0.3}$, respectively, as shown in Figure 8a. The strain-hardening effect induced by strengthening elements such as Ni, molybdenum, and niobium existing in the cladding is responsible for this increase in microhardness [11,23]. This increase in hardness is also due to the difference in the coefficients of thermal expansion of YSZ and Inconel 625. This variation causes geometric dislocations (GD) and the pinning of dislocation motions at their edges by hard particles, resulting in matrix strain hardening [14]. The microhardness variation across the cross-sectional area and heat-affected zone (HAZ) are presented in Figure 8a.

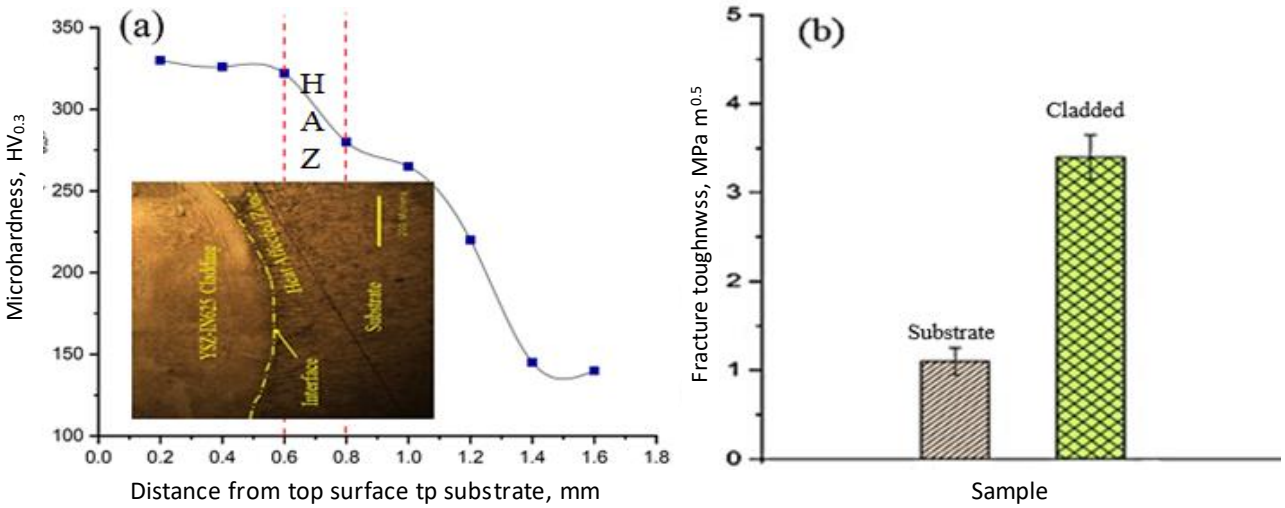

Figure 8. *(a) Vicker's microhardness distribution (b) fracture toughness values*

The heat-affected zone (HAZ) is that area of metal that has not been melted and has undergone changes in properties due to exposure to relatively high temperatures during TIG welding. The fracture toughness of substrate and cladding was found to be 1.1±0.04 and 3.4±0.06 MPa $m^{1/2}$, respectively. The high fracture toughness value of the cladding can be related to strain hardening and pinning effects caused by hard particles. The YSZ hard particles in composite cladding enhance fracture energy due to crack front blunting [31,32]. Figure 8b shows the fracture toughness values of substrate and cladding.

Effect of impingement angle on erosion (air-jet erosion test)

The solid particle erosion test was performed at 30 and 90° angles on the uncladded substrate and the cladding specimens. Figure 9a - 9d summarises optical pictures of the degraded surfaces of the substrate and cladded workpieces exposed to different test angles. It was discovered that cladded samples experienced less damage compared to the substrate at all the impingement angles. Figures 9a and 9b indicate that both testing angles leave a deeper impression on the substrate. In contrast, the surface of claddings has the most minor imprints (Figure 9c - 9d). Figure 9e depicts substrate and claddings' erosive wear (weight loss). In the cladded sample, the erosion rate is governed by the composition of cladding material [24,30]. The outcomes show that the erosive wear resistance of cladding samples is almost 3.5 times and 2.4 times better than uncladded samplesat 30 and 90° impingement angles, respectively. The composite cladding's superior performance can be attributed to its high hardness and fracture toughnes. As already stated, the YSZ-IN625 claddings have a high fracture toughness, which leads to higher erosion resistance. The YSZ particle reinforcement in the claddings helps to strengthen the IN625 matrix by dispersion. As a result, the reinforced claddings' microhardness and erosive resistance have increased even further. Furthermore, stable oxides such as Cr_2O_3 and ZrO_2 helped to improve composite claddings' erosion resistance.

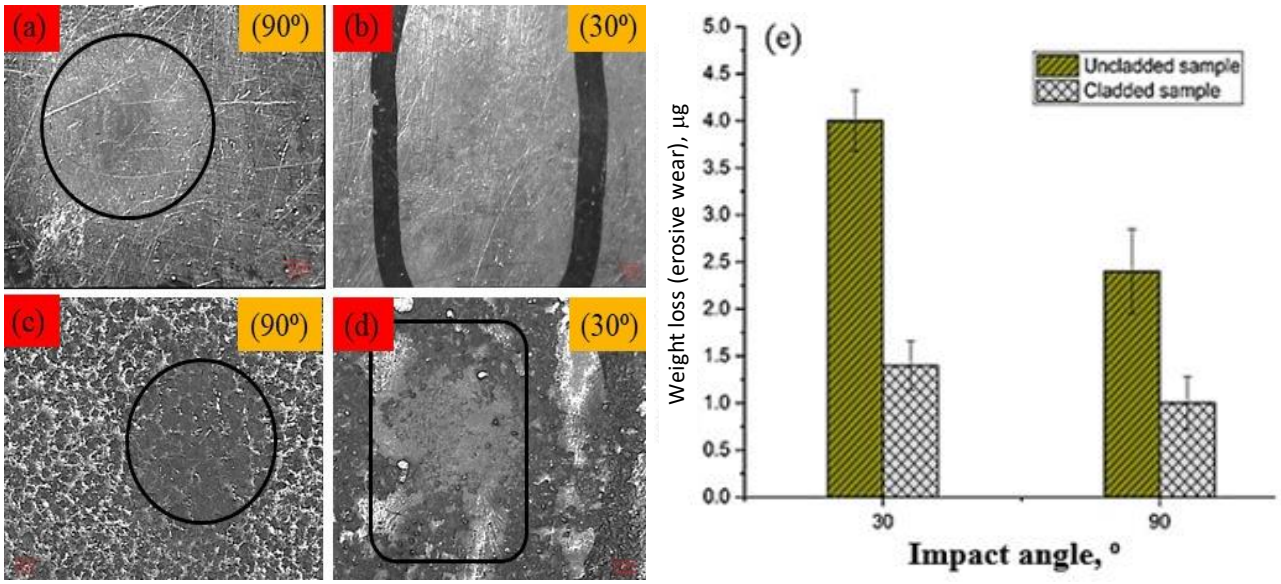

Figure 9. *(a-d) Optical pictures of the degraded surfaces of both (substrate and cladding) (e) weight loss Impact angle of the substrate and cladded sample at different impact angles*

Erosion mechanism

SEM images were used to investigate the erosive mechanism of the damaged outer layer of the substrate and cladding samples. Figure 10 (a-d) shows the surface morphology of the substrate and cladded samples subjected to the erosion test. At a 30° impact angle, material removal occurs in uncladded samples due to the micro-cutting and ploughing caused by the sharp edges of the

erodent, as shown in Figure 10a. Apart from that, some minor craters and cavities were also generated. Figure 10b shows the formation of craters due to the repetitive collision of eroded particles resulting in the pull-out of debris at a 90° impact angle. Material detachment from the groove indicates erosive wear. As a result, it is possible to conclude that the substrate exhibits a ductile erosion mechanism, in which the material predominantly fails via plastic deformation [30]. Indentation-induced plastic deformation was dominant at a 90° impact angle [20]. Maximum material removal happens at 30°, while less removal occurs at 90°.

As demonstrated in Figure 10c, micro-cutting and ploughing are significant erosion mechanisms that contribute to removing the material from the cladded sample. The SEM picture of degraded cladding revealed numerous abrasion markings with little plastic distortion and a few small grooves developed on the outer layer at a 30° impact angle, as illustrated in Figure 10c. At a 30° angle, the erodent imposes a powerful repeated tangential force onto the intended surface. This tangential force removed certain unmelted particles of the cladding, leaving behind traces of minor craters. The uniformly dispersed YSZ particles bind the IN625 matrix and limit the plastic deformation of the cladding in contrast to the uncladded sample. At a 90° impact angle, the impact of erosive particles on the splats led to the accumulation of debris liberated from the IN625 matrix at the location of impingement and the removal of a significant amount of material from the outer layer. The crater was formed by removing a chunk of material from the surface. Furthermore, as illustrated in Figure 9d, the impact created by the erodent is passed to the unmelted YSZ particles, producing cracks and contributing to crack propagation. A schematic representation of different types of plastic deformation by solid particles is presented in Figure 11.

YSZ-IN625 claddings exhibit superior erosion resistance to uncladded samples at all impact angles. The YSZ-IN625 composite cladding has higher fracture toughness and hardness values. An optimum mix of the microhardness and fracture toughness resulted from the favourable interaction between the hard ceramic YSZ particles with the IN625 matrix, which helped to enhance the erosion performance of YSZ-IN625 composite cladding.

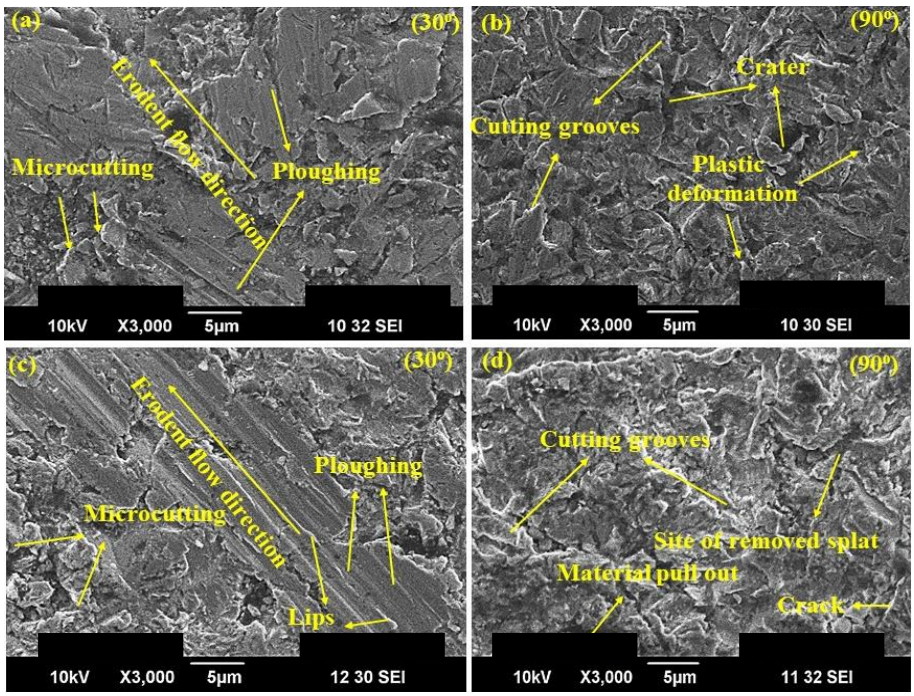

***Figure 10**. SEM images of (a-b) substrate and (c-d) YSZ-IN625 cladding eroded areas with impingement angles*

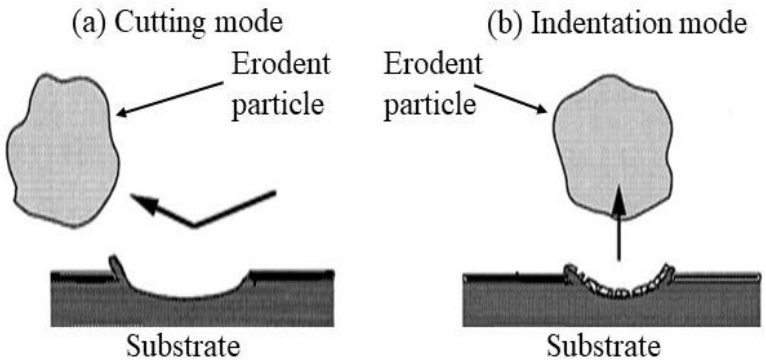

Figure 11. *Schematic representation of different types of plastic deformation by erodent (a) cutting mode at 30° and (b) indentation mode at 90°*

Conclusion

A YSZ-Inconel 625 composite cladding was developed using the TIG weld cladding technique and was analysed for its erosion performance. The following are the prominent conclusions of the current research:

- The cross-section of the produced cladding demonstrated a good metallurgical bonding with the substrate without any sign of cracking and high dilution.
- The microhardness value of the cladding was 330 $HV_{0.3}$, which is 2.5 times better than that of the substrate (140 $HV_{0.3}$).
- The fracture toughness test revealed that the cladding had a maximum toughness value of 3.4 MPa $m^{0.5}$ compared to the substrate's toughness value of 1.1 MPa $m^{0.5}$.
- The various stable phases and oxides, like γ- Ni, Cr_2O_3, and ZrO_2, acted as a protective layer and contributed to better erosion resistance.
- The partially melted YSZ particles retained their original shape in the cladding, resulting in a compact dendrite (IN625) and an equiaxed (YSZ) structure of grains, significantly enhancing the microhardness and resistance to erosion.
- The grooves and craters on surfaces indicate that the erosion mechanism comprises ploughing, micro-cutting, and indentation-induced plastic deformation for the substrate. The mechanisms of degradation in claddings at 30 and 90° impact angles included micro-cutting, detached splats, and cracks. The erosive wear performance of YSZ-IN625 cladding enhanced approximately 3.5 times at 30° and 2.4 times at 90° impact angles.

Acknowledgements*: This research received no specific grant from any funding agency in the public, commercial, or not-for-profit sectors.*

Conflicts of interest*: The authors also declare that they have no conflict of interest.*

References

[1] Z. Azakli, R. Gümrük, Particle Erosion Performance of Additive Manufactured 316L Stainless Steel Materials, *Tribology Letters* **69** (2021) 130. https://doi.org/10.1007/s11249-021-01503-0

[2] N. Kaur, M. Kumar, S .K. Sharma, D. Young, S. Kumar, N. M. Chavan, S. V Joshi, N. Singh, H. Singh, Applied Surface Science Study of mechanical properties and high temperature oxidation behavior of a novel cold-spray Ni-20Cr coating on boiler steels, *Applied Surface Science* **328** (2015) 13-25. https://doi.org/10.1016/j.apsusc.2014.12.033

[3] M. Naveed, H. Schlag, F. König, S. Weiß, Influence of the Erodent Shape on the Erosion Behavior of Ductile and Brittle Materials, *Tribology Letters* **65(18)** (2017) . https://doi.org/10.1007/s11249-016-0800-x
[4] J. H. Tylczak, Erosion-corrosion of iron and nickel alloys at elevated temperature in a combustion gas environment, *Wear* **302** (2013) 1633-1641. https://doi.org/10.1016/j.wear.2013.01.008
[5] J. Singh, L. Thakur, S. Angra, Abrasive wear behavior of WC-10Co-4Cr cladding deposited by TIG welding process, *International Journal of Refractory Metals and Hard Materials* **88** (2020) 105198. https://doi.org/10.1016/j.ijrmhm.2020.105198
[6] S. Saroj, C.K. Sahoo, M. Masanta, Microstructure and mechanical performance of TiC-Inconel825 composite coating deposited on AISI 304 steel by TIG cladding process, *Journal of Materials Processing Technology* **249** (2017) 490-501. https://doi.org/10.1016/j.jmatprotec.2017.06.042
[7] N. Kamboj, L. Thakur, A study of processing and high-temperature sliding wear behaviour of Inconel-625 alloy TIG weld cladding, *International Journal of Materials Engineering Innovation* **13** (2022) 1. https://doi.org/10.1504/ijmatei.2022.10045603
[8] N. Kamboj, L. Thakur, Tribology International Experimental investigation of the high temperature sliding wear behaviour of RSM optimized YSZ-Inconel 625 TIG weld cladding, *Tribology International* **187** (2023) 108741. https://doi.org/10.1016/j.triboint.2023.108741
[9] J. Singh, L. Thakur, S. Angra, Effect of argon flow rate and standoff distance on the microstructure and wear behaviour of WC-CoCr TIG cladding, *Journal of Physics: Conference Series* **1240** (2019). https://doi.org/10.1088/1742-6596/1240/1/012162
[10] [J. Singh, L. Thakur, S. Angra, A study of tribological behaviour and optimization of WC-10Co-4Cr Cladding, *Surface Engineering* **37** (2021) 70-79. https://doi.org/10.1080/02670844.2020.1745367
[11] S. S. Sandhu, A. S. Shahi, Metallurgical, wear and fatigue performance of Inconel 625 weld claddings, *Journal of Materials Processing Technology* **233** (2016) . https://doi.org/10.1016/j.jmatprotec.2016.02.010
[12] R. Ranjan, A. Kumar Das, Protection from corrosion and wear by different weld cladding techniques, *Materials Today: Proceedings* **57** (2022) 1687-1693. https://doi.org/10.1016/j.matpr.2021.12.329
[13] R. Panwar, P. Chandna, Parameter optimization of FSW aviation-grade AA8090 using Taguchi grey relational analysis, *Aircraft Engineering and Aerospace Technology* **95** (2023) 715-724. https://doi.org/10.1108/AEAT-05-2022-0118
[14] G. Sreedhar, M. M. Alam, V. S. Raja, Hot corrosion behaviour of plasma sprayed YSZ/Al_2O_3 dispersed NiCrAlY coatings on Inconel-718 superalloy, *Surface and Coatings Technology***2 04** (2009) 291-299. https://doi.org/10.1016/j.surfcoat.2009.07.026
[15] A. Bakkar, M. M. Z. Ahmed, N. A. Alsaleh, M. M. E. S. Seleman, S. Ataya, Microstructure, wear, and corrosion characterization of high TiC content Inconel 625 matrix composites, *Journal of Materials Research and Technology* **8** (2019) 1102-1110. https://doi.org/10.1016/j.jmrt.2018.09.001
[16] H. Y. Al-Fadhli, J. Stokes, M. S. J. Hashmi, B. S. Yilbas, The erosion-corrosion behaviour of high velocity oxy-fuel (HVOF) thermally sprayed inconel-625 coatings on different metallic surfaces, *Surface and Coatings Technology* **200** (2006) 5782-5788. https://doi.org/10.1016/j.surfcoat.2005.08.143
[17] B. Wang, J. Gong, A. Y. Wang, C. Sun, R. F. Huang, L. S. Wen, Oxidation behaviour of NiCrAlY coatings on Ni-based superalloy, *Surface and Coatings Technology* **149** (2002) 70-75. https://doi.org/10.1016/S0257-8972(01)01427-X

[18] T. Aravind Nagaraj, S. P. K. Babu, M. Rajkumar, R. Mahendran, High temperature erosion behavior of cast nickel base 73Ni-13Cr-4Sn-4Bi-Mo alloy, *Materials Research Express* **6** (2019) . https://doi.org/10.1088/2053-1591/ab26d0

[19] Q. B. Nguyen, V. B. Nguyen, C. Y. H. Lim, Q. T. Trinh, S. Sankaranarayanan, Y. W. Zhang, M. Gupta, Effect of impact angle and testing time on erosion of stainless steel at higher velocities, *Wear* **321** (2014) 87-93. https://doi.org/10.1016/j.wear.2014.10.010

[20] G. T. Burstein, K. Sasaki, Effect of impact angle on the slurry erosion-corrosion of 304L stainless steel, *Wear* **240** (2000) 80-94. https://doi.org/10.1016/S0043-1648(00)00344-6

[21] C. P. Paul, S. K. Mishra, P. Tiwari, L. M. Kukreja, Solid-Particle Erosion Behaviour of WC/Ni Composite Clad layers with Different Contents of WC Particles, *Optics and Laser Technology* **50** (2013) 155-162. https://doi.org/10.1016/j.optlastec.2013.03.002

[22] M. Solecka, M. Kopyściański, J. Kusiński, A. Kopia, A. Radziszewska, Erosive wear of inconel 625 alloy coatings deposited by CMT method, *Archives of Metallurgy and Materials* **61** (2016) 1201-1206. https://doi.org/10.1515/amm-2016-0199

[23] N. Kamboj, L. Thakur, A study of the processing and characterization of RSM optimized YSZ-Inconel625 wear-resistant TIG weld cladding, *Surface Topography: Metrology and Properties* **10** (2022) 045021https://doi.org/10.1088/2051-672X/aca345

[24] H. Vasudev, L. Thakur, H. Singh, A. Bansal, Erosion behaviour of HVOF sprayed Alloy718-nano Al_2O_3 composite coatings on grey cast iron at elevated temperature conditions, *Surface Topography: Metrology and Properties* **9** (2021) 035022. https://doi.org/10.1088/2051-672X/ac1c80

[25] H. Vasudev, L. Thakur, H. Singh, A. Bansal, A study on processing and hot corrosion behaviour of HVOF sprayed Inconel718-nano Al_2O_3 coatings,*Materials Today Communications* **25** (2020) 101626. https://doi.org/10.1016/j.mtcomm.2020.101626

[26] G. Bi, C. N. Sun, M. L. Nai, J. Wei, Micro-structure and mechanical properties of nano-TiC reinforced Inconel 625 deposited using LAAM, *Physics Procedia* **41** (2013) 828-834. https://doi.org/10.1016/j.phpro.2013.03.155

[27] A. Keyvani, M. Saremi, M. H. Sohi, An investigation on oxidation, hot corrosion and mechanical properties of plasma-sprayed conventional and nanostructured YSZ coatings, *Surface and Coatings Technology* **206** (2011) 208-216. https://doi.org/10.1016/j.surfcoat.2011.06.036

[28] D. F. Zambrano, A. Barrios, L. E. Tobón, C. Serna, P. Gómez, J. D. Osorio, A. Toro, Thermal properties and phase stability of Yttria-Stabilized Zirconia (YSZ) coating deposited by Air Plasma Spray onto a Ni-base superalloy, *Ceramics International* **44** (2018) 3625-3635. https://doi.org/10.1016/j.ceramint.2017.11.109

[29] T. Dharini, P. Kuppusami, N. Kumar, D. D. Kumar, A. K. Soman, A. M. K. Kirubaharan, Tribological properties of YSZ and YSZ/Ni-YSZ nanocomposite coatings prepared by electron beam physical vapour deposition, *Ceramics International* **47** (2021) 26010-26018. https://doi.org/10.1016/j.ceramint.2021.06.006

[30] G. Prashar, H. Vasudev, Structure-property correlation and high-temperature erosion performance of Inconel625-Al_2O_3 plasma-sprayed bimodal composite coatings, *Surface and Coatings Technology* **439** (2022) 128450. https://doi.org/10.1016/j.surfcoat.2022.128450

[31] F. F. Lange, The interaction of a crack front with a second-phase dispersion, *Philosophical Magazine* **22** (1970) 983-992. https://doi.org/10.1080/14786437008221068

[32] F. F. Lange, Phase retention and fracture toughness of materials containing tetragonal ZrO_2, *Pergamon Press Ltd*, 1980. https://doi.org/10.1016/b978-1-4832-8414-9.50098-5

J. Electrochem. Sci. Eng. **14(4)** (2024) 499-522; http://dx.doi.org/10.5599/jese.2246

Open Access : : ISSN 1847-9286
www.jESE-online.org

Original scientific paper

High-velocity oxy-fuel and high-velocity air fuel sprayed WC-Co-Cr coatings on solution-treated 21-4N steel for slurry and corrosion resistance

Rajanna Lingappa[1,✉], Tumakur Gangadhar Mamatha[1], Momballi Shivappadevaru Prabhuswamy[2], Vikrant Singh[3] and Anuj Bansal[3]

[1]*Department of Mechanical Engineering, JSS Science and Technology University, Mysuru, Karnataka 570006, India,*
[2]*Department of Mechanical Engineering, JSS Academy of Technical Education, Noida, Uttar Pradesh 201301, India*
[3]*Department of Mechanical Engineering, Sant Longowal Institute of Engineering and Technology, Longowal, Sangrur-148106, Punjab, India*

Corresponding author: ✉rajannalingappa07@gmail.com

Received: January 13, 2024; Accepted: April 19, 2024; Published: April 23, 2024

Abstract

This study aims to fabricate WC-Co-Cr coatings on the solution-treated 21-4N steel utilizing high-velocity oxy-fuel (HVOF) and high-velocity air fuel (HVAF) techniques. The microstructure, hardness, surface quality, porosity, slurry erosion, and corrosion resistance of HVOF and HVAF coatings on solution-treated 21-4N steel were investigated and compared. The HVAF sprayed WC-Co-Cr coating exhibited dense structure, more hardness (1582 HV), greater fracture toughness (5.69 MPa $m^{1/2}$), less decarburization, and lower porosity (0.97 %) as compared to HVOF sprayed coating. Further, slurry jet erosion tests and electrochemical corrosion tests provide a comprehensive evaluation of the coating's performance under erosive and corrosive conditions. Eventually, the conclusive results of the study affirm the exceptional performance of the high-velocity air fuel sprayed WC-Co-Cr coating, demonstrating its superiority in both erosion and corrosion resistance compared to the high-velocity oxygen fuel sprayed coating.

Keywords

Slurry jet erosion test, electrochemical corrosion test, surface modification

Introduction

Slurry erosion is a significant concern in various industries where mechanical components operate in harsh conditions, such as slurry pumps, chemical processing equipment, hydropower machinery, and construction equipment [1]. Slurry erosion is a form of wear caused by the abrasive action of a mixture of solid particles suspended in a liquid (water). Slurry erosion emerges when

abrasive particles suspended in a liquid come into contact with the surfaces of in-service components. This abrasive interaction leads to material loss and degradation of the affected components over time. By taking a proactive approach to protecting components against slurry wear and implementing appropriate measures, we can significantly extend their lifespan and reduce the maintenance and replacement costs of industrial and mechanical systems. Therefore, surface coatings and the use of wear-resistant metals and alloys are crucial techniques in engineering and material science for enhancing the durability and longevity of mechanical components, especially in harsh environments. Several surface modification processes, including weld overlays, chemically and thermally diffused coatings, and thermal spray processes, have been widely utilized to develop wear-resistant coatings on various components in industries where abrasion and erosion are prevalent concerns [2]. Thermal spray coatings have gained significant popularity in recent years due to their flexibility in material selection, minimal impact on coating properties, cost-effectiveness, lightweight, adaptability to complex shapes, rapid application process, versatility across industries, long service life, and outstanding resistance to erosive and corrosive wear [3]. However, WC-Co-Cr composite coatings were practically proven and precisely engineered compositions, enabling the development of coatings tailored for erosive wear and corrosion environments [4]. WC-Co-Cr coatings produced by the high-velocity oxy-fuel (HVOF) technique possess an optimum combination of high levels of hardness, wear, and corrosion resistance, making them suitable for a wide range of applications in industries such as aerospace, oil and gas, and hydropower. However, prolonged exposure of powder particles to the high-temperature flame in the HVOF process can lead to decarburization. As a result, the formation of undesired phases like W_2C and amorphous phases can have a detrimental effect on the quality and performance of HVOF-processed cermet coatings, impacting their resistance to erosive and corrosive wear [5]. Therefore, minimizing decarburization is a crucial aspect of enhancing the resistance of coatings (WC-Co-Cr) to both corrosion and erosion wear. Hence, the high-velocity air fuel (HVAF) process has gained recognition for its effectiveness in limiting decarburization during the spraying of coatings, particularly when compared to other thermal spray processes like HVOF. The HVAF process is a thermal spray coating technique that involves the controlled combustion of a mixture of air and fuel gas, usually propane or hydrogen, to produce a high-velocity, high-temperature gas stream used to propel coating material onto a substrate. The lower combustion temperature of HVAF compared to HVOF results in less prolonged exposure of the powder particles to high temperatures, thereby minimizing the extent of decarburization [6]. Therefore, the HVAF process is a preferred choice in situations where minimizing decarburization and achieving specific mechanical properties like high hardness, low porosity, uniformity, and higher fracture toughness are critical factors for the application. According to various researchers, improved coating properties are essential for enhancing resistance to erosive and corrosive wear [7-9]. Furthermore, extensive research has been conducted to analyze the structure and tribological properties of WC-Co-Cr coatings deposited through HVOF and HVAF processes [10-12]. Liu *et al.* [13] investigated the slurry erosion resistance of AISI 304 steel coated with a combination of WC-Co-Cr powder and Nano WC-12Co powder. They reported that the addition of 15 % WC-12Co nanopowder to the conventional WC-Co-Cr powder resulted in a significant improvement in coating hardness (1677 to 1873 HV0.3). Due to the uniform distribution of nano-WC-12Co particles among WC particles, the structure is less porous and dense. The slurry erosion resistance of the coating with 15 % Nano WC-12Co added to the WC-Co-Cr was superior to that of the conventional HVAF sprayed WC-Co-Cr coating, attributed to enhanced hardness and fracture toughness. The study conducted by Wang *et al.* [14] performed wear and

corrosion studies on coatings produced using both HVOF/HVAF processes. HVOF coating exhibits a smaller degree of decarburization, whereas HVAF coating demonstrates no decarburization. They concluded that HVAF coating outperformed HVOF coating with wear and corrosion resistance owing to its higher hardness, lesser porosity, and better toughness. Wang *et al.* [15] conducted sand erosion and cavitation tests on WC-CoCr coatings that were deposited using both processes onto AISI 316 austenitic steel. The phase analysis by X-ray diffraction (XRD) indicated the presence of decarburization in the HVOF-sprayed coating. In contrast, the XRD analysis of the HVAF-sprayed coating showed no signs of decarburization and exhibited superior mechanical properties. The sand erosion with cavitation tests revealed that HVAF coating showed better wear resistance against HVOF coating owing to higher hardness, lower porosity, and better fracture toughness. Kumar *et al.* [16] performed a sand erosion experiment on the HVOF/HVAF fabricated coatings (WC-Co-Cr) on the underwater turbine steel (16Cr5Ni). HVAF coatings had lower erosion wear loss than HVOF coatings due to improved properties such as improved adhesion, increased toughness, heightened hardness, and greater residual stress with a lower level of oxidation. Yang Li *et al.* [17] conducted solid particle erosion tests on WC-Co-Cr coatings developed by HVOF/HVAF processes. Their investigation revealed that HVAF coatings exhibited superior erosion resistance compared to HVOF coatings across all tested angles owing to lesser porosity, high hardness, and improved fracture toughness. Another study conducted by Hong *et al.* [18] investigated the corrosion properties of WC-CoCr coatings fabricated by the HVOF process under various spray conditions to optimize coating porosity. They disclosed that the coating developed under a particular spray condition had improved corrosion resistance due to decreased porosity as compared to other coatings developed under different spray conditions. It's worth noting that while there's extensive research on the morphology, tribological properties, erosion, and corrosion studies of WC-Co-Cr coatings produced by HVOF and HVAF processes, there seems to be a gap in comparative studies specifically addressing the erosive and corrosive wear performance of coated thermally treated steel. This gap might present an opportunity for further research to explore and compare the erosive and corrosive wear performance of WC-Co-Cr coatings applied to thermally treated steel using both HVOF and HVAF methods. In addition, conducting focused studies on the erosion resistance of coatings and investigating the implications of various parameters is critical for advancing protective solutions in erosive environments. Thus, from all this literature, it can be said that the superior quality and consistency of HVOF coatings are emphasized and attributed to precise control over parameters such as particle velocity, temperature, and coating microstructure. Secondly, the enhanced adhesion of HVOF coatings to the substrate is underscored, resulting from stronger interfacial bonding and improved coating-substrate cohesion. Thirdly, the finer microstructures and superior mechanical properties of HVOF-sprayed coatings are highlighted, owing to the higher particle velocities and thermal energy associated with the HVOF process. Lastly, while acknowledging the cost-effectiveness of electric arc spray for certain applications, the overall performance and value of HVOF spraying in terms of coating quality and longevity are emphasized, considering factors such as reduced maintenance costs and extended service life of coated components.

By keeping the above-mentioned things in consideration, the current study aims to compare WC-10Co4Cr coatings fabricated using two different thermal spray processes, namely high-velocity oxygen fuel and high-velocity air fuel on the solution-treated 21-4N utilizing a similar feedstock powder. Various parameters, including cross-sectional microstructure, hardness, surface quality, fracture toughness, and porosity of the coatings, were evaluated and compared. Furthermore, two coatings were subjected to slurry wear and electrochemical corrosion tests to evaluate their

performance under erosive wear and in corrosive environments. In addition, the comparison is also based on the morphologies of the coatings produced by HVOF and HVAF methods, particularly tested under erosion and corrosion wear conditions.

Experimental

Substrate material and coating powder

Commercially available from H.C. Stark (sintered and dried), the 86WC-10Co-4Cr powder was deposited on the solution-treated 21-4N steel substrate by HVOF and HVAF thermal spray equipment. The chemical constituents of cast 21-4N steel are 0.5 % C, 20.8 % Cr, 3.6 % Ni, 8.8 % Mn, 0.33 % N, 0.25 % Si, 0.13 % Mo, 0.001 % S, 0.04 % P, and 65.549 % Fe. For the HVOF process, a coarse powder with a nominal particle size of 15 to 45 µm (AMPERIT 556.074) was used, whereas a fine powder with a nominal particle size of 5-30 µm (AMPERIT 556.059) was used for the HVAF process. The two feedstock powders employed had the same composition (5.073 wt.% C, 10.992 wt.% Co, 3.039 wt.% Cr and 80.896 wt.% W) with a mean particle size of 21 µm for HVOF and 19 µm for the HVAF process. Using a scanning electron microscope (SEM) allows for a detailed examination of the morphology and composition of the powder particles with the corresponding EDS plot shown in Figure 1. The EDS analysis represents the distinct elements like WC, Co, Cr, and C in the powders. Figure 1(a) depicts the powder that seems to exhibit a high degree of porosity but with ideal spherical shapes.

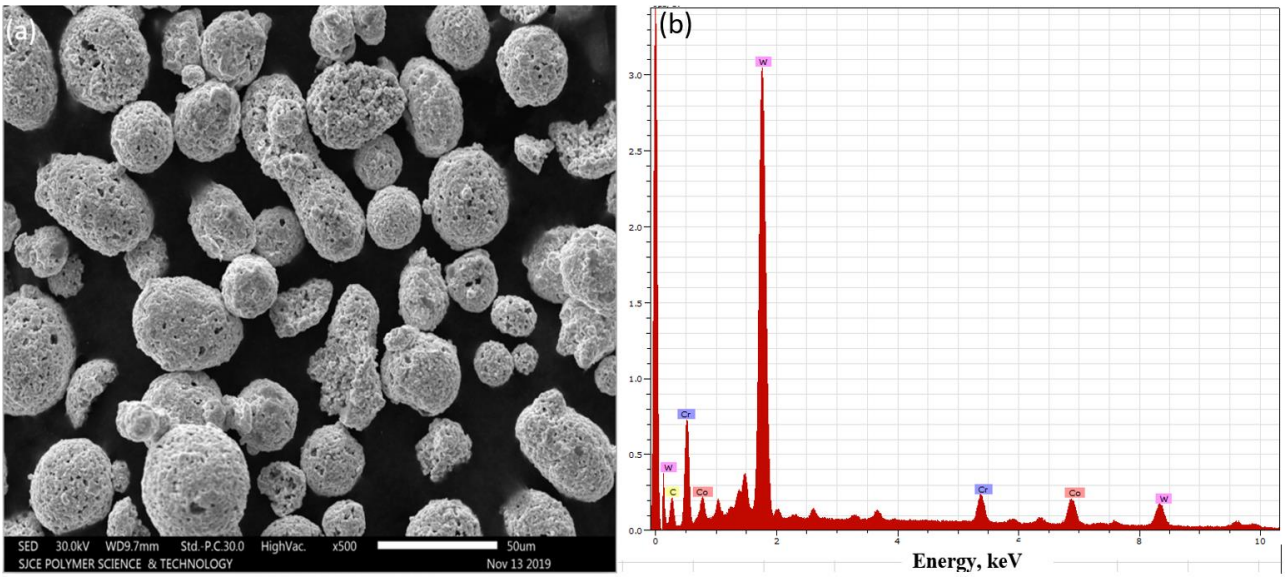

Figure 1. *Surface morphology of feedstock powder (a), and EDS graph (b)*

Coating procedure

Before coating deposition, a square specimen (100×100×5 mm^3) of solution-treated 21-4N steel was cleaned with acetone, and grit blasting was performed at 5 kg cm^{-2} pressure using alumina powder having a mesh size of 60 µm to enhance its roughness (R_a = 8.5 µm) for better adhesion of coating material. Two coating thicknesses of approximately 350 µm were developed using convertible gun C6 [Make: Kermetico] for both HVOF/HVAF systems at Spray Met Technologies Pvt. Ltd., Bengaluru, Karnataka. A square specimen sized 25×25×5 mm^3 [19] was machined from the coated substrate by a wire-electric discharge machine for a slurry erosion test. Table 1 provides the optimal process parameters used to develop the coatings. The temperature of the specimen was maintained below 120 °C during deposition by using a compressed air-cooling system, and the

spraying angle was 90 °C. Also, in the current research work, 2 levels and 3 factors are varied, keeping two parameters constant by varying one parameter at a time. So, the total samples coated from the HVOF and HVAF processes were 60 nos. (30 each). Each slurry experiment requires 3 samples, so a total of 18 from each HVOF and HVAF coated sample are consumed. Corrosion tests need 2 samples from each HVOF and HVAF coating.

Table 1 *HVOF and HVAF thermal spray process optimized process parameters with their values*

HVOF		HVAF	
Oxygen flow rate, SLPM*	250-300	Air flow rate, SLPM	83.4
Air flow rate, SLPM	460-550	Fuel (propane) bas flow rate, SLPM	84
Fuel (LPG) flow rate, SLPM	50-55	Nitrogen flow rate, SLPM	23.1
Oxygen pressure, MPa	1	H_2 flow rate, SLPM	15
Air pressure, MPa	5.5	Air pressure, MPa	5.79
Fuel pressure, MPa	7	Fuel pressure; MPa	5.92
Spray distance, mm	152-177	Spray distance, mm	177
Spray angle, °	90	Spray angle, °	90

*1 SLPM = 0.00073386 mol s^{-1}

Microstructure and phase characterization

Phase characterization of feedstock powder and fabricated coatings was conducted by employing a Bruker D8 Advance diffractometer (XRD) with an angular range of 2θ110 to 168° and an increment of 0.0001° angle using Cu Kα radiation. The field emission scanning electron microscope (FESEM) (ZEISS Neon 40) equipped with an energy dispersive spectroscopy (EDS) attachment was used to examine the coatings for microstructure cross-sections, the structure of feedstock powder, and the eroded sample surface. The roughness tester (Veeco Model: NT9100) was used to measure the surface irregularities of the fabricated coatings. Open-source image processing Image J analysis software was employed to determine the porosity of the as-sprayed coatings utilizing a 20,000× magnification SEM micrograph. The values reported were an average of ten measurements. The indentation crack method was used to measure the fracture toughness of the two coatings. The Vickers indenter was applied to the polished cross-section of the coating for 15 s at a load of 5 kg (49.05 N). The Evan and Wilsaw equation [20] was used to estimate the fracture toughness of coatings. The density of the coatings was calculated by subtracting the volume fractions of porosity from the volume fractions of their WC and Co-Cr binder counterparts. Carbide retention was calculated from the intensity integrals of WC and W_2C.

Microhardness of coatings

The Vickers microhardness test was conducted on various coated and uncoated samples employing the RMHT-201 apparatus. Indentation was executed under a load of 500 gm with a holding time of 20 seconds [21-22]. Subsequently, measurements were taken at five distinct points, and the average value was utilized for the analysis.

Slurry erosion wear test

According to the literature review, interacting factors comprising slurry velocity, impact angle, and sand concentration had noticeable effects on material removal [23]. The slurry erosion resistance of two separate thermally developed coatings was evaluated using a jet-type slurry erosion test apparatus, TR-411 [Ducom], as shown in Figure 2. The same test rig was also used by Singh *et al.* [24], in the existing literature. The test rig is made up of a conical-shaped tank (hopper) that can hold 60 kg of slurry. The slurry tank is filled with tap water and a particular size of sand

particles to prepare the slurry for testing. High-pressure fresh water is delivered into a mixing chamber through a positive displacement rotary vane pump powered by a 3-phase AC motor (1.5 kW). Furthermore, fresh sand particles are added into a mixing chamber using a spiral (worm) mechanism powered by an alternating current motor. Inside the mixing chamber, the freshly entered sand particles were mixed with high-pressure water before being ejected through a nozzle at the bottom of the mixing chamber and impacting the securely held specimen in the fixture. In this research, three parameters were used: slurry velocity (20 and 40 m s^{-1}), impact angles (30 and 90°), and sand concentrations (20,000 and 30,000 ppm). A fixed distance of 50 mm between the surface of the sample and the tip of the nozzle is maintained for all experiments. All the slurry erosion tests were carried out in compliance with ASTM G-73 standards. The specimen is placed in the holding fixture, and the angle range is varied from 15 to 90° at a step size of 15°, allowing the slurry to impact the specimen's surface by changing the various parameters. Silica sand collected from the riverbank contains particles with irregular shapes and sharp edges, which make it an effective erodent for slurry erosion tests. The particle sizes of 250 µm were sieved and mixed with tap water to prepare the slurry mixture for testing. The samples are washed with acetone to remove dirt, oil, and any attached matter from the sample surface before and following each slurry test, and the corresponding weight is measured using a weighing scale with a precision of 0.01 mg [Contech, CA224]. Each slurry test lasts 5 hours, with sample weight loss recorded at 30-minute intervals. Following weight measurement, calculate the volume loss of coatings by taking density into account.

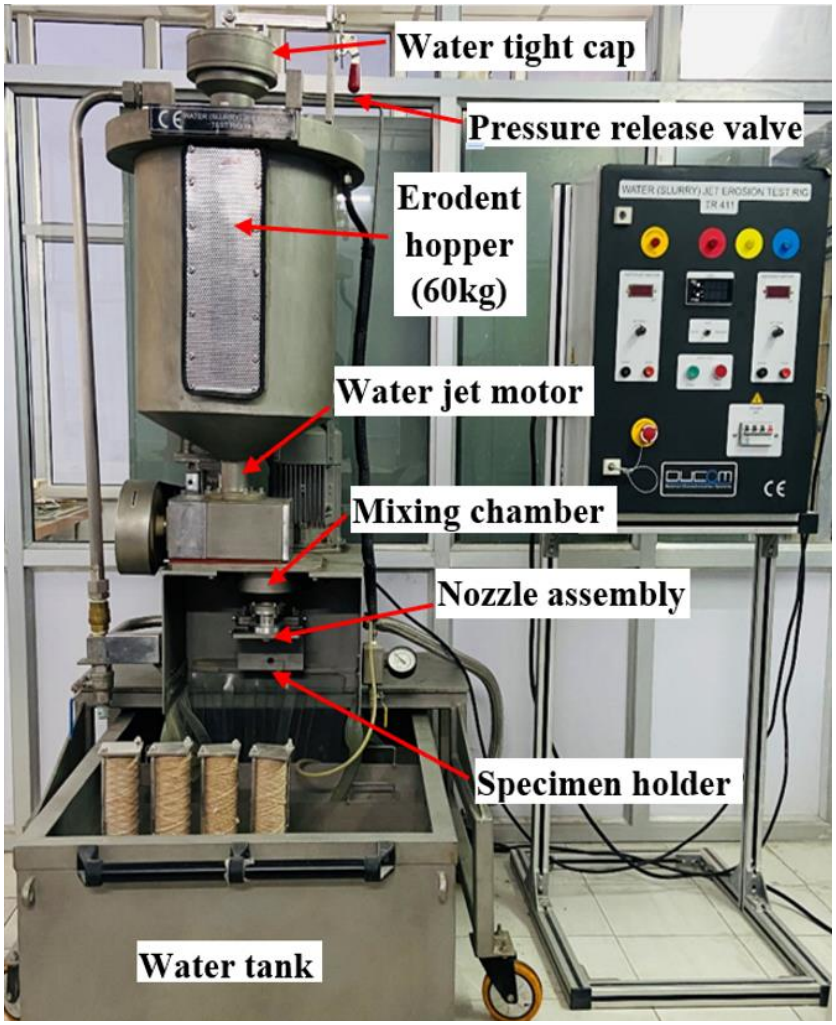

Figure 2. *Slurry jet erosion test rig setup [24]*

Electrochemical corrosion test

The potentiodynamic characteristics of two coatings were investigated using a three-electrode system with a potentiostat (Model 1010E, *Gamry Instruments)* at a scanning rate of 1 mV s^{-1}. The two WC-10Co-4Cr coated samples, each with an area of 1 cm^2, were immersed in a sodium chloride (NaCl) electrolyte. Using a standard three-electrode system, the corrosion parameters (E_{corr} and i_{corr}) of both coatings were measured. A saturated calomel electrode (SCE) functioned as the reference electrode, graphite operated as the counter electrode, and the coated sample treated as the working electrode in the standard electrochemical corrosion setup. The corrosion test setup employed a 3.5 wt.% NaCl solution as the working electrolyte. The electrochemical corrosion test is comprised of two main tests: open circuit potential (OCP) and potentiodynamic polarization test (PPT). The coated surface was dipped in a 3.5 wt.% NaCl solution at ambient temperature for an hour to allow for the establishment of a stable electrochemical condition. After the open circuit potential had stabilized, polarization curves were acquired at a scan rate of 1 millivolt per second (1 mV s^{-1}). Then, a plot of E versus Log I was constructed, and the meeting point of the anodic and cathodic polarization curves with their respective linear fits was identified and corresponding corrosion parameters (corrosion potential and corrosion current density) values were determined using the Tafel extrapolation method. To obtain an average value, at least four separate sets of experiments were performed on each specimen.

Results and discussion

Microstructure of substrate material

The microstructure of cast steel 21-4N steel and solution-treated steel is indicated in Figures 3(a) and 3(b). The heterogeneous structure of cast steel typically depicts two distinct phases, namely, the austenitic matrix phase (bright region) and carbide bunches (dark region), as shown in Figure 3(a). The cast steel microstructure contains two types of carbides, such as M_7C_3 and $M_{23}C_6$ (M can be Cr, C, and Fe) [25]. Since cast steel contains a high carbon content, it is generally chromium-sensitive, resulting in chromium carbide precipitation. These carbide precipitates were identified all along the grain boundary and within the austenite matrix [26]. The optical micrograph indicates that $M_{23}C_6$ carbides are located at grain boundaries, which is the most beneficial location. After obtaining sufficient energy from the heat treatment, chromium and carbon elements could move rapidly into the matrix, with grain boundaries being the beneficial location for carbide precipitation [27]. The optical microstructural image of solution-treated 21-4N steel (1150 °C for 120 min) is shown in Figure 3(b). This image (Fig. 3(b)) reveals that the volume fraction of carbides was significantly low, and a tiny fraction of carbides were concentrated at the grain boundary. Furthermore, solution treatment at an optimal temperature (1150 °C for 120 min) results in more uniform carbide dissolution in the austenitic matrix and a substantial number of twins appearing within the grain boundary region (complete carbide dissolution at the grain boundary). The reduction in carbides was attributed to the rapid penetration of chromium and carbon elements into the austenite matrix after obtaining the required energy from the heat treatment. Hence, the solution-treated (1150 °C for 120 min) 21-4N steel microstructure exhibits complete dissolution of carbide in the austenitic matrix, and a uniform austenitic phase was obtained as compared to the cast structure is depicted through optical micrographs.

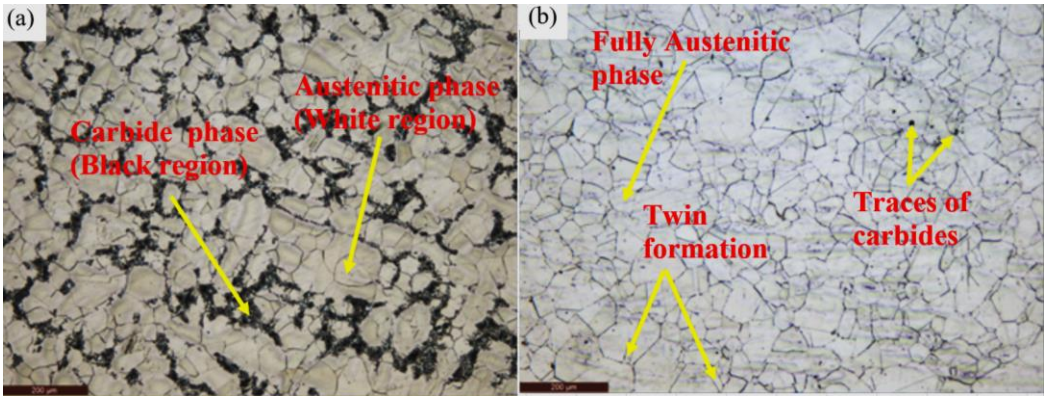

Figure 3. *Optical micro graphical microstructure of cast 21-4N steel (a) solution-treated 21-4N steel at 1150 °C and (b) 120 min*

Microstructure of coatings

Figure 4 indicates the cross-sectional microstructural photographs of two coatings obtained with FESEM and the EDS plot.

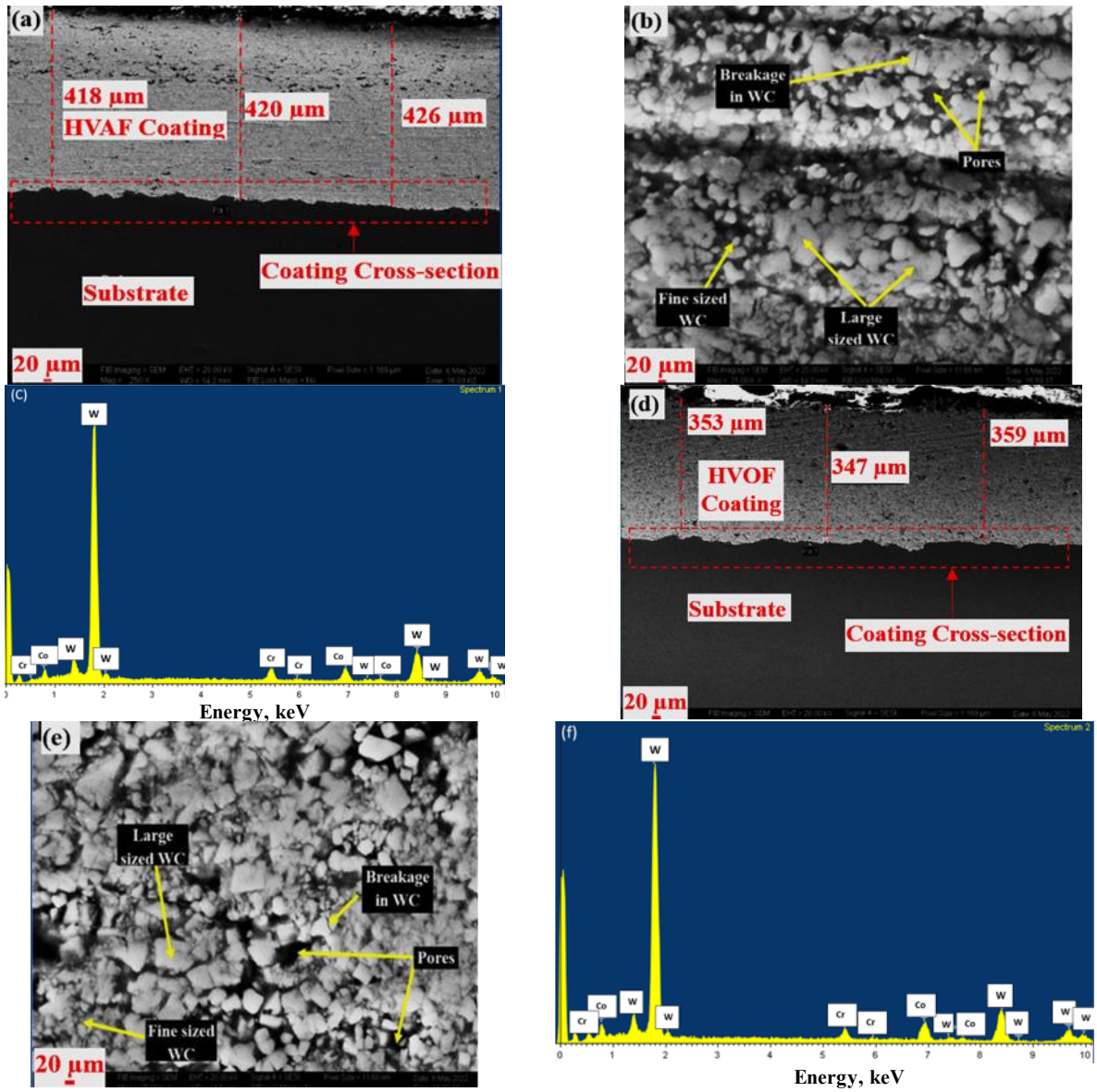

Figure 4. *Cross-sectional micrographs images of high and low magnification of (a and b) HVAF sprayed WC-CO-Cr coating, (d and e) HVOF sprayed WC-CO-Cr coating, EDS graph of (c) HVAF sprayed WC-Co-Cr coating, and (f) HVOF sprayed WC-Co-Cr coating*

The HVAF sprayed coating was observed to have an average thickness of around 421 µm, Figure 4(a) and the HVOF sprayed coating was observed to have an average coating thickness of around 353 µm, Figure 4(d). FESEM microstructure images present low and high-magnification views. Both coatings exhibit a robust and uniform structure in their micrographs, demonstrating strong bonding with the underlying substrate material. Further, each coating displays a certain level of laminar microstructure. In the HVOF coating, the presence of larger tungsten carbide (WC) particles within the binder matrix, and in certain areas, there are instances where WC particles appear to adhere to the coating with less surrounding binder material. Meanwhile, the HVAF coating displays a more consistent and uniform distribution of finer WC particles within the binder matrix [28]. Upon closer inspection of the high magnification images, Figures 4(b) and 4(e), some discernible pores and instances of WC particle breakages become apparent [29-31]. These breakages are attributed to the combination of high-velocity impact and the partially molten state of the particles impacted against the hard substrate material. It was also observed from images 4 (a) and 4 (d) that the pores that appear in the HVAF coating are fewer than in the HVOF coating. Furthermore, HVOF-fabricated coatings exhibit a non-uniform structure with more pores, while HVAF-sprayed coatings display a more compact structure with fewer pores. This distinction can be attributed to the intrinsic variations in the spraying processes. Specifically, the unique properties of the HVAF process contribute to the formation of a more tightly packed structure with reduced porosity.

Phase constitutions of coatings

Figure 5 shows XRD images of the original powder, HVAF, and HVOF deposited coatings. The graph of sprayed powder revealed that WC (JCPDF 00-51-0939) was the dominant phase, with a small amount of Co (JCPDF 15-806), W (JCPDF 00-004-0806), and Co_3W_3C (JCPDF 01-078-3750) phases being present. With WC as the dominant phase, minor phases of $Co_{12.9}Cr_{17.1}$ (JCPDF 01-080-8333) and W_2C (JCPDF 35-776) were detected in the HVAF coating. Furthermore, in the case of HVOF, the sprayed coating exhibits WC as a major phase with smaller traces of $Co_{12.9}Cr_{17.1}$, Co_3W_3C and W_2C (JCPDF 35-776) phases [32].

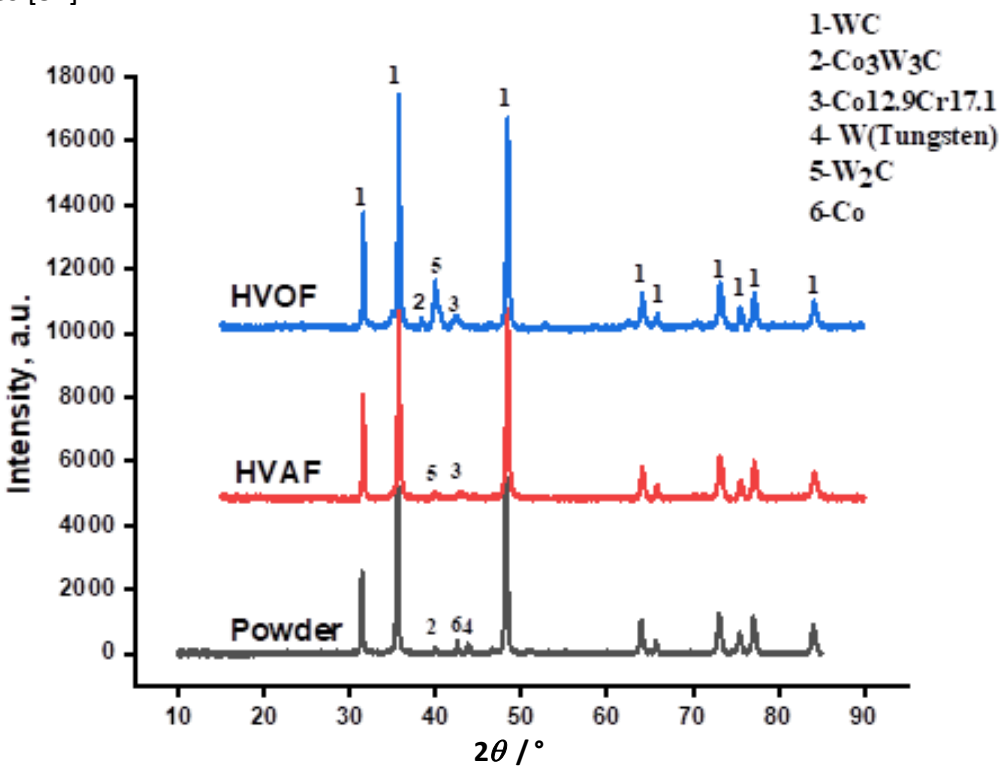

Figure 5. *Phase analysis (XRD) of powder, HVOF, and HVAF sprayed coating*

It is worth noting that the WC particles are transformed, including decarburization and dissolution, which lead to the formation of additional phases, including the presence of di-tungsten carbide (W_2C) in both coatings [33]. However, the diffraction peak of W_2C in the HVOF coating is higher than that of the HVAF coating. These results were consistent with previous work that used a similar powder as found in the literature [34-36]. Further, owing to the vaporization of a small amount of Co phase, no detectable cobalt-contained phases were present. However, both coatings demonstrate a noticeable quantity of Co-Cr-rich phase. *i.e.,* $Co_{12.9}Cr_{17.1}$ (42.638 degrees), as a similar phase is reported in the literature [37]. Hence, the High-Velocity Air Fuel (HVAF) process, by utilizing air instead of oxygen, can significantly impact the characteristics of the sprayed coating, particularly in reducing the effect of decarburization and minimizing the brittleness of the coating [38-39].

Microhardness analysis

The microhardness of the samples was assessed at five different locations, and the average was computed. This approach is necessary because the microhardness value can vary depending on the composition of the material. When the indentation occurs in areas with harder phases, the microhardness tends to be higher. Conversely, when the indent is located in regions with softer phases or defects, the microhardness may be lower. The average microhardness readings for the uncoated specimen were observed to be 164 HV, while for the HVAF-coated specimen, it was 1582 HV, and for the HVOF specimen, it was 1398 HV. The probable reason for variations in microhardness values between the specimens could be attributed to differences in material composition, grain structure, presence of defects, or variations in coating thickness. For instance, the HVAF-coated specimen might exhibit higher microhardness due to the application of a hard coating layer, while the uncoated specimen may have a lower microhardness value due to the absence of such coatings. Similarly, the HVOF specimen might have intermediate microhardness values depending on the specifics of the coating process and material used. Further, the indent micrographs of coated, HVAF, and HVOF sprayed samples are presented in Figure 6.

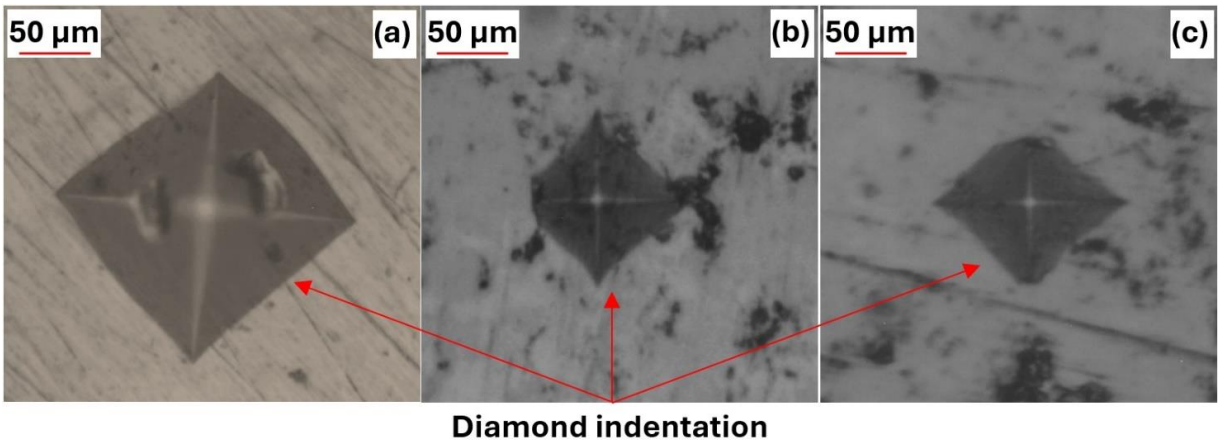

Figure 6. *Indent micrographs for (a) uncoated sample, (b) HVAF sprayed sample, and (c) HVOF sprayed sample.*

Fracture toughness, roughness, and porosity of coatings

The HVAF coatings showed a lower surface roughness of 2.16±0.12 µm against the HVOF coating roughness of 4.68±0.45 µm, which may be due to the use of fine powder particles in the HVAF process. In addition, the fracture toughness of HVAF coating (5.69±0.24 MPa $m^{1/2}$) is higher than that of HVOF coating (4.29±0.35 MPa $m^{1/2}$), possibly due to less porosity, improved bonding between WC particles, and the binder matrix offering higher resistance to cracking. The HVAF-

sprayed coating has a lower measured porosity (0.97±0.13 %) than the HVOF-sprayed coating (1.26±0.14 %), indicating that it is slightly more compact and has fewer pores. The microstructure analysis of two as-sprayed coatings was determined from SEM micrographs (20,000× magnification) of the coating cross-section using Magni-scientific image analysis software (Divergent Rays Computing Inc.). The porosity volume fraction (%), carbide volume fraction (%), carbide size (µm), binder volume fraction (%), and density (g cm^{-3} values are listed in Table 2.

Table 2. *Porosity volume fraction, carbide volume fraction, binder volume fraction, and density (gm cm^{-2}) of HVAF and HVOF sprayed coatings*

	HVOF	HVAF
Porosity volume fraction, %	1.26±0.14	0.97±0.13
Carbides volume fraction, vol.%	63.3±1.5	76.9±1.2
Carbides size, µm	1.1± 0.5	1.21± 0.3
Binder volume fraction, vol.%	35.05±0.63	22.01±0.31
Density, gm cm^{-3}	12.64	13.60

Slurry erosion responses of developed coatings

The cumulative volume loss from slurry erosion experiments can be influenced by different parameters, namely slurry velocity, impact angle, and sand concentration parameters. Goyal *et al.* [40] proposed a correlation for the wear rate of hydro turbine materials, Equation (1).

$$E_W = k\, V^p\, d^q\, C^r \quad (1)$$

where E_W represents slurry rate, V denotes the speed at which slurry impinges on the sample surface, d specifies the average erodent size, and C denotes sand concentration in the slurry. Values of k, p, q, and r denote the corresponding exponents of slurry velocity, average erodent size, and sand concentration. In the current research work, slurry erosion experiments were conducted to evaluate the performance of the HVOF and HVAF coatings under varying slurry velocity, impact angle, and sand concentration conditions at 2 levels. The parametric variation at 2 levels was chosen to maintain experimental tractability while capturing meaningful trends in slurry erosion behavior. By limiting the levels of variation, the focus on investigating the most significant factors influencing erosion resistance without introducing unnecessary complexity can be done. Furthermore, the selected levels for each parameter were based on previous literature findings and practical considerations. For example, the slurry velocity was varied at 20 and 40 m s^{-1} to encompass a range commonly encountered in industrial applications, allowing for a comprehensive assessment of erosion resistance under typical operating conditions [1]. Similarly, impact angles of 30 and 90° were chosen to represent both acute and normal impingement angles, reflecting real-world scenarios where hydroturbine components are subjected to varying degrees of erosion wear [1]. Lastly, sand concentrations of 20,000 and 30,000 ppm were selected to cover a range of abrasive particle densities typically encountered in slurry environments.

Effect of slurry velocity

The slurry velocity of impinging sand particles had a significant effect on the volume loss of both coatings. When particles in a slurry possess higher kinetic energy, they strike the material surface with more impact force. It has been revealed from the literature that more forceful impacts on the target material led to greater or higher volume loss at higher slurry velocity. Figure 7 bar chart illustrates the impact of varying slurry velocity (20 and 40 m s^{-1}) on two sprayed coatings at a sand concentration of 20,000 ppm with a 90° impact angle. We observed that the volume loss of both coatings is higher for

a normal impact angle (90°). This fact was confirmed by various researchers in their reported work [7-9,39]. Islam *et al.* [41] found that at lower velocities, the kinetic energy of the sand particles may not be sufficient to cause significant material removal. Instead, impacts are primarily elastic, meaning they don't exceed the threshold energy required for material removal. On the other hand, if the sand particles acquire more kinetic energy as a result of their increased velocity, it consequently leads to more material removal. According to Maekai *et al.* [42], impinging sand particles must have the same or higher than the critical energy to remove material from the substrate surface. As expected, sand particles achieve more critical energy at higher slurry velocities, resulting in higher material removal in comparison to lower velocities. As reported by Ramesh *et al.* [43], it corroborates the understanding that increasing slurry velocity directly translates to higher kinetic energy of the sand particles, leading to more focused and forceful impacts at multiple locations on the target material surface. This analysis demonstrates a significant difference in volume loss between the HVAF-sprayed coating and the HVOF-sprayed coating under two slurry velocities. At 20 m s^{-1} slurry velocity, the HVAF coating experienced 1.39 times lower volume loss as compared to the HVOF coating. Further, at 40 m s^{-1} slurry velocity, the HVAF coating demonstrated a lower volume loss, with a factor of 1.76 times as compared to the corresponding HVOF coating [44]. Hence, HVAF-coated steel showed a higher erosion resistance than HVOF coating at all velocities under given conditions. Therefore, the HVAF coating has the highest erosion resistance due to its high hardness, less porosity, and higher fracture toughness than the HVOF coating.

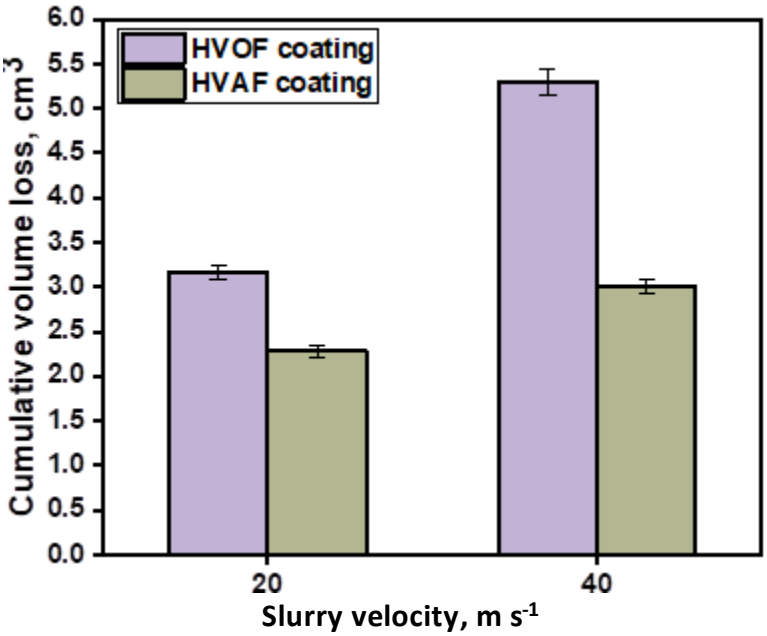

Figure 7. *Erosion volume loss of coatings (HVOF/HVAF) at different slurry velocities.*

Effect of impact angle

Hydro turbine parts in hydroelectric plants are prone to erosion wear during service due to the action of a wide range of impact angles at various locations. The erosion of target material at different angles can identify the angles that pose the highest risk of erosion under specified test conditions. These investigations aid in understanding the kind of erosion (whether it is ductile or brittle) under specific conditions. According to the literature review, ductile materials tend to exhibit more pronounced erosion at sharp angles, typically falling within the range of 15 to 30°, but at the higher angle of impact (90°), the erosion rate gradually decreases. For brittle materials, erosion wear tends to be less severe at low impingement angles. However, an increase in impact angle causes the force

of the impinging particles to cause substantial damage to the target material. As a result, brittle materials resist erosion wear at acute angles but are more vulnerable to shear stress and deteriorate more rapidly at normal angles [45]. Figure 8 bar chart illustrates the impact of varying impact angles (30 and 90°) on two sprayed coatings at a sand concentration of 30,000 ppm with 40 m s^{-1} slurry velocity. It appears from the figure that a trend in slurry erosion volume loss for both HVAF and HVOF-coated steel changes with increases in impact angles. This is the fragile nature of the coatings as reported by researchers [46]. Malik *et al.* [47] noticed that materials with high hardness, such as ceramics and cermets, withstand erosion at lower angles. In contrast, ductile metals suffer more material loss due to higher shear forces. In contrast, ductile material absorbs a significant amount of impact energy at normal angles, resulting in reduced material loss. In comparison, HVAF-coated steel showed higher erosion resistance than HVOF coating at all impact angles under given conditions. At a 30° impact angle, the HVAF coating experienced 1.53 times lower volume loss compared to the HVOF coating. In contrast, at a 90° impact angle, the HVAF coating demonstrated a lower volume loss, with a factor of 1.84 times as compared to the corresponding HVOF coating. However, the erosion mechanism changed from plowing to plastic deformation as the angle changed from 30 to 90°. This aligns with the fundamental principles of slurry erosion, where the angle at which particles impinge on a surface can significantly influence the volume loss of both coatings.

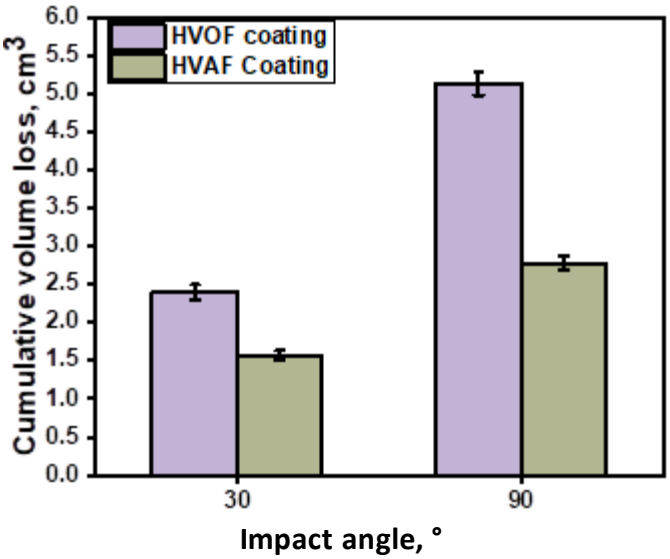

Figure 8. *Erosion volume loss of coatings (HVOF/HVAF) at different impact angles.*

Effect of sand concentrations

The concentration of sand particles in the slurry can have a significant effect on the erosive wear of the target material. At lower concentrations of sand particles in the slurry, there are fewer abrasive particles available for impact with the target surface. Consequently, the erosive effects are less pronounced. However, as the concentration of sand particles increases, more particles are available to interact with the target surface. This leads to a higher frequency of impacts and abrasions, resulting in an increased loss of material from the surface of the target. Figure 9 bar chart illustrates the impact of varying sand concentrations (20,000 and 30,000 ppm) on two sprayed coatings at a slurry velocity of 20 m s^{-1} with a 30° impact angle. The variation in volume loss with sand concentration for both coatings is an important finding. According to these studies [8,9,22,48-49], an increase in sand concentration would increase the frequency of indentation, resulting in more surface damage and material loss. Du *et al.* [50] express a similar view that an increase in sand concentration promotes more sand particles striking the target surface per unit time, causing more

mass loss. However, some researchers [51] reported that higher sand concentrations contributed to a reduction in mass loss. It is supported by the fact that at higher sand concentrations, inter-particle collision, the interaction between rebounding particles with the fresh incoming particles causes a shielding effect, which reduces kinetic energy, thereby altering the penetrating path of the sand particles, causing them to strike at different angles or bypass the impact surface, resulting in a lower weight loss. As reported by Kleis *et al.* [52], collisions among particles, particle motion, and sedimentation could enhance the effect of sand concentration on slurry erosion wear. At 20,000 ppm, the HVAF coating experienced 1.33 times lower volume loss compared to the HVOF coating. In contrast, at a 90° impact angle, the HVAF coating demonstrated a lower volume loss, with a factor of 1.53 times as compared to the corresponding HVOF coating. Hence, HVAF-coated steel showed the highest erosion resistance to HVOF coating at all sand concentrations, owing to improved hardness, lesser porosity, and higher fracture toughness than HVOF coating.

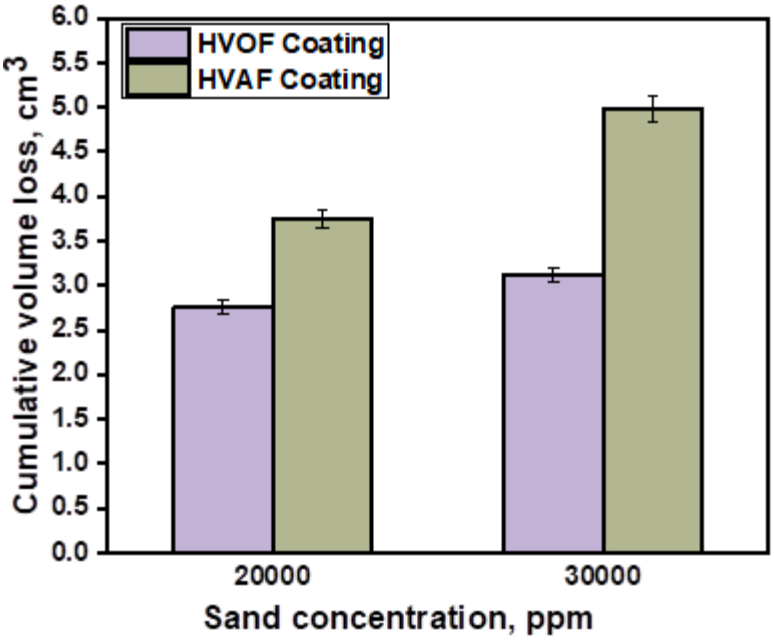

Figure 9. *Erosion volume loss of coatings (HVOF/HVAF) at different sand concentrations.*

Analysis of wear specimens

The impact of high-velocity sand particles causes the gradual degradation of coating material during service. To understand the mechanisms behind the removal of coating material are investigated by performing a surface morphological analysis of eroded samples under different conditions using SEM.

Effect of slurry velocity

Figure 10 indicates SEM images of eroded surfaces of HVOF/HVAF fabricated coatings by the effect of distinct slurry velocities (20 and 40 m s^{-1}) at a normal impact angle. The volume loss of both coatings is observed to increase with increasing slurry velocity. This is attributed to the increase in impact energy of sand particles on the surface of coatings, which leads to more forceful impacts, which subsequently result in greater mass loss from the coatings. Both coatings depict more volume loss at higher slurry velocities (40 m/s), but HVAF sprayed coating has lower volume loss as compared with HVOF sprayed coating at all slurry velocities, keeping other conditions identical. The SEM images of HVOF/HVAF coatings eroded at lower slurry velocity (20 m s^{-1}) are shown in Figures 10(a) and 10(b). The typical erosion mechanisms of the coatings were found to be craters, lip-based

plastic deformation, and spalling. The impact of sharp-edged sand particles created some deep craters in the HVOF coatings, as shown in Figure 10(a). The growth of smaller cracks and the removal of WC particles caused by crack coalescence in the inter-splat result in coating spalling in the form of debris. In comparison, HVAF coatings display a smoother surface than HVOF sprayed coating (Figure 10(b)). Figures 10(c) and 10(d) show the eroded images of HVOF/HVAF coatings at 40 m s^{-1} slurry velocity. At this velocity, coatings show enhanced damage compared to lower velocity (20 m s^{-1}), which increases the network of cracks and results in coating spallation, leading to more mass loss. It has been noticed that increasing slurry velocity causes more spalling of coatings due to WC grain detachment and more visible craters. Similar observations were made by the researcher in their work [53-55]. However, increasing the slurry velocity may not have an impact on the change in the mechanism of coating material removal in the current study. Thus, the combination of high hardness, fracture toughness, low porosity, and a dense structure helps to maximize the resistance of HVAF coatings.

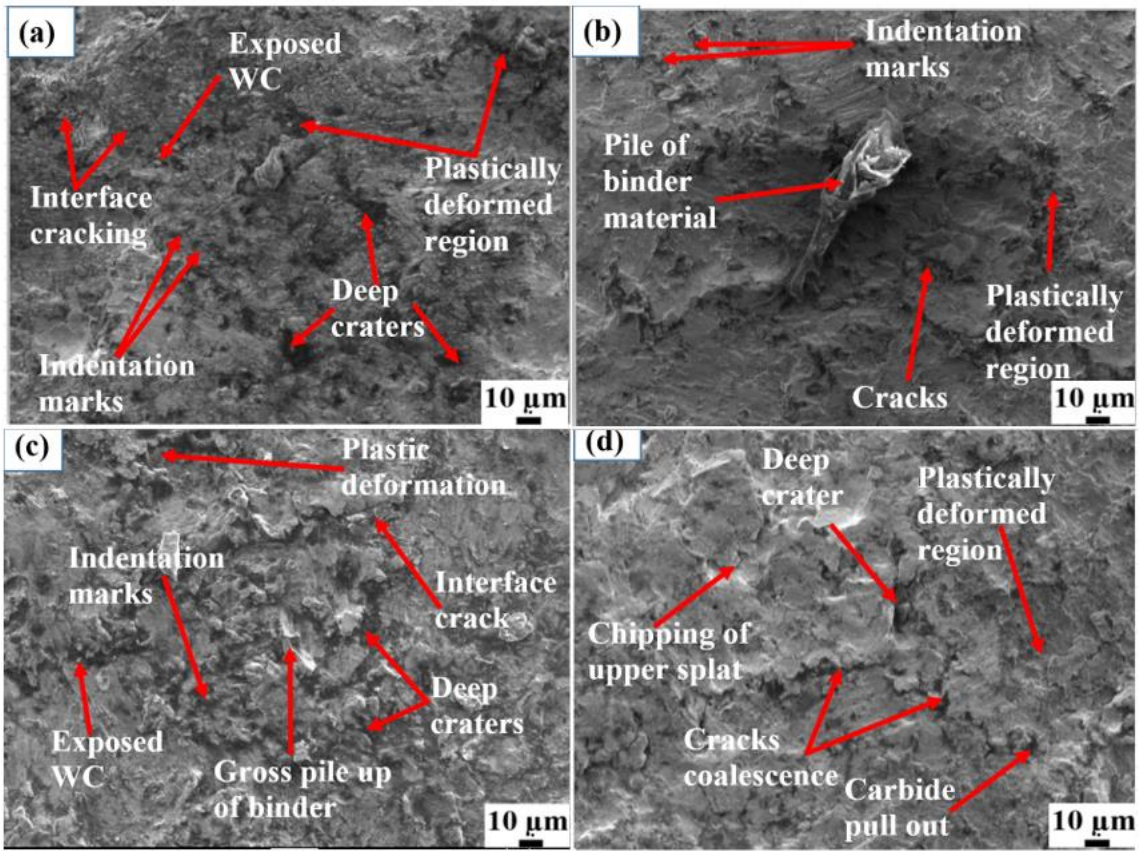

Figure 10. *Eroded SEM images of coatings at jet velocity of 20 m s^{-1} for (a) HVOF sprayed coating, (b) HVAF sprayed coating, and at 40 m s^{-1} for (c) HVOF sprayed coating, (d) HVAF sprayed coating*

Effect of impact angle

Figure 11 illustrates SEM images of eroded areas of both WC-CO-Cr coatings subjected to different impact angles (30 and 90°). The HVOF process typically depicts the coatings with larger tungsten carbide (WC) particles as observed from the microstructure. These larger particles may have more interstitial spaces between them, resulting in a higher porosity than HVAF coatings. Due to the larger particle size and potentially higher porosity, the erosive action of sand particles can more easily disengage or fracture individual WC particles from the binder matrix. This further diminishes the overall erosion resistance of the coating. As the impact angle increases, the energy transferred to the coating surface during the erosive process also increases, resulting in greater

material removal and higher volume loss. Both coatings exhibit the highest amount of volume loss at higher impact angles (90°), but HVAF sprayed coating has better resistance to erosion than HVOF sprayed coating at all impact angles, keeping other conditions identical. This behavior ideally represents the brittle nature of the fabricated coatings. Figures 11(a) and 11(b) SEM images provide valuable insight into the erosive mechanisms and wear patterns observed in HVOF and HVAF sprayed coatings subjected to an acute angle of 30°. It reveals ploughing marks caused by the tangential action of sand particles, binder matrix removal, micro-cutting, and deep grooves responsible for coating material loss. The sand particles slide against the coating, eradicating the softer binder material (Co/Cr) from the coating surface, leaving WC particles exposed to the coating surface. Then, further impingement of sand parties causes them to fall by leaving shallow craters. Figures 11(c) and 11(d) reveal the surface morphology of damaged surfaces of coatings at normal impact angles (90°). The coating spalling occurs mainly by plastic deformation, resulting in the ejecting of coating material. It was observed that owing to the effect of fatigue stress induced by the sand particles on the impact area of the coating, cracks could develop at the stress concentration areas. Further, cracks coalesced, resulting in the spalling of coatings and enhancing the mass loss of coating material. These findings align with the work of Liu *et al.* [56]. Hence, coatings spallation by fatigue stress of sand particles was the main mechanism of loss of coating material at a normal impact angle. HVAF-sprayed coatings had less surface damage than HVOF-sprayed coatings. Thus, the combination of high hardness, fracture toughness, low porosity, and a dense structure helps to maximize the resistance of HVAF coatings.

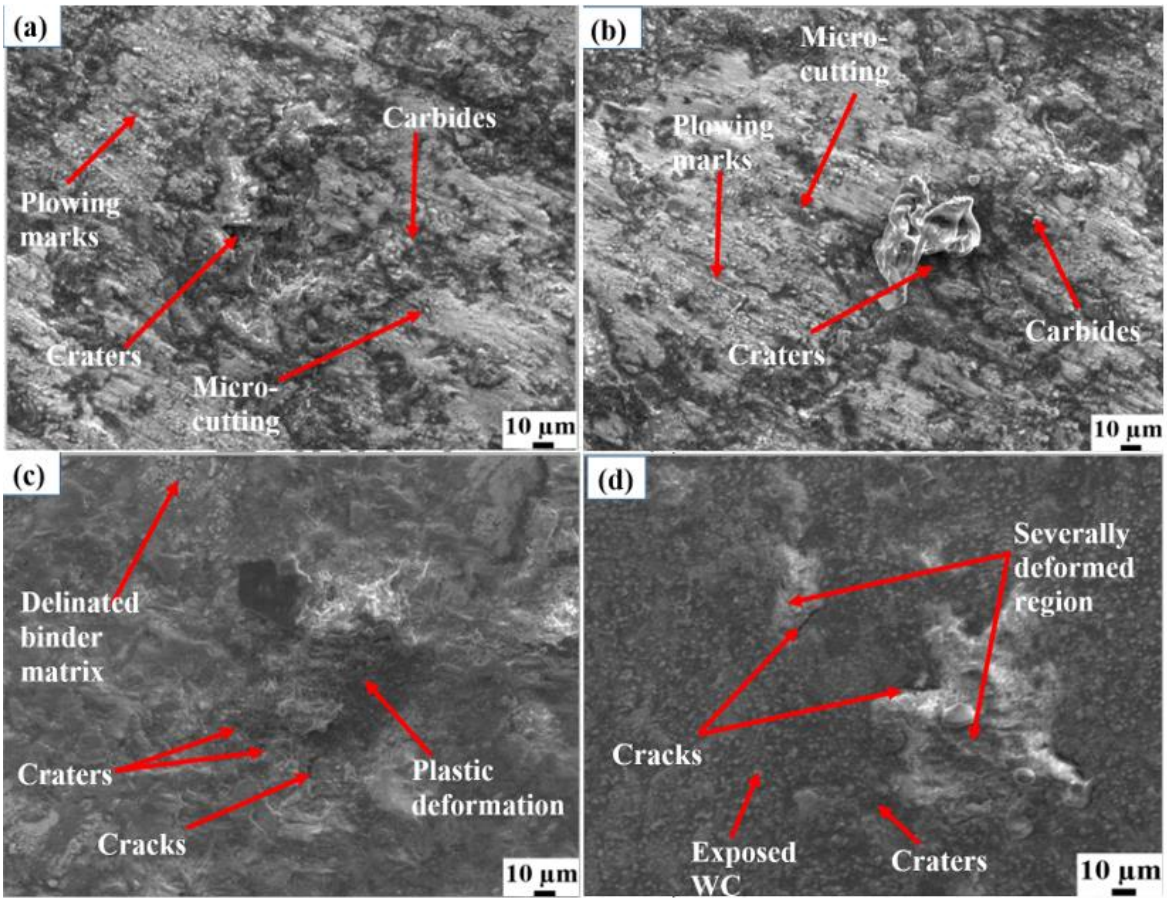

Figure 11. *Eroded SEM images of coatings at 30° impact angle for (a) HVOF sprayed coating, (b) HVAF sprayed coating, and at 90° for (c) HVOF sprayed coating, (d) HVAF sprayed coating*

Effect of sand concentrations

Figure 12 illustrates SEM images of eroded areas of both WC-CO-Cr coatings subjected to different sand concentrations (20,000 and 30,000 ppm). The volume loss of both coatings is observed to increase with increasing sand concentrations. For all concentrations, HVAF coatings perform better than HVOF coatings in terms of erosion resistance. As sand concentration goes up from 20,000 to 30,000 ppm, subsequently coatings damage elevates. The HVAF sprayed coating displays a smoother surface than the HVOF-coated surface for all sand concentrations. The main mechanism of material is the plowing of coating material, which leads to the formation of lips. From Figures 12(a) and 12(b), coatings are removed by plowing action followed by cutting off material from the impacted area, leading to the formation of smaller craters and carbides being exposed to the surface. Figures 12 (c) and 12(d) show that smaller craters were formed due to WC being pulled out from the binder material. Similar observations were made by [57] in their investigation. Thus, the improved properties of HVAF coatings help maximize the resistance compared to HVOF coatings.

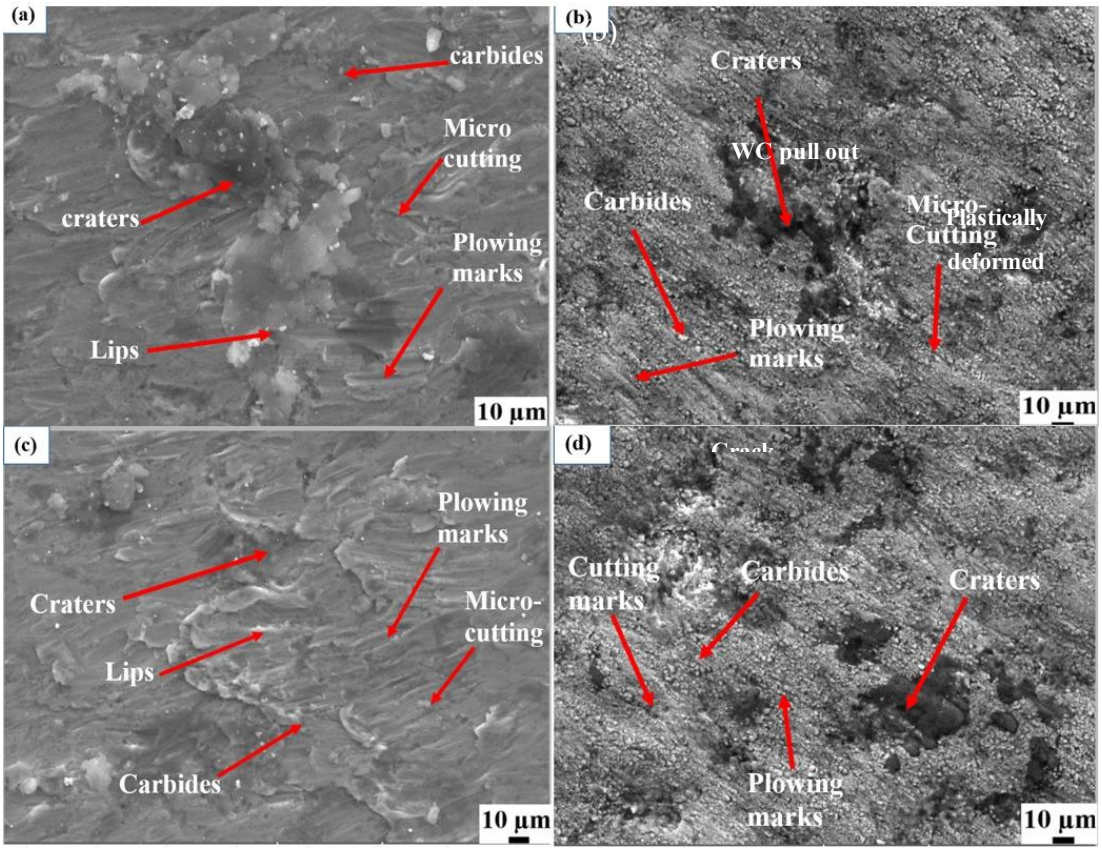

Figure 12. *Eroded SEM images of coatings at 20000 ppm slurry concentration for (a) HVOF sprayed coating, (b) HVAF sprayed coating, and at 30000 ppm for (c) HVOF sprayed coating, (d) HVAF sprayed coating*

Electrochemical corrosion test

The polarization curves (refer to Figure 13) obtained from this technique can provide important information about the corrosion resistance of coatings (HVOF/HVAF). The coated specimen was soaked in a 3.5 wt.% NaCl solution for 1 hour for stabilization of the OCP. After the establishment of a consistent OCP through preconditioning, polarization curves were obtained. These electrochemical parameters, such as the corrosion potential (E_{corr}) and current density (I_{corr}) can be determined from the polarization curves using the Tafel extrapolation method. This method involves fitting linear segments to both the anodic (corrosion) and cathodic (protection) portions of the polarization curves. These linear fits are used to estimate the corrosion potential (E_{corr}) and corrosion current

density (i_{corr}) by identifying the intersection point of the two lines. These values of Ecorr and i_{corr} for the two coatings are provided in Table 3. Specifically, the HVAF-sprayed coating exhibits an Ecorr value of -0.392 V, while the HVOF coating registers an E_{corr} value of -0.331 V. The i_{corr} value for the HVAF coating is measured at 15 A cm^2, indicating a lower rate of corrosion compared to the HVOF coating, which records an i_{corr} value of 40 A cm^2. This suggests that the HVAF-sprayed coating exhibits superior corrosion resistance under the given conditions. These findings were aligned with previous research [6,31] specifically confirming that the HVAF-fabricated WC-10Co-4Cr coating displays outstanding corrosion resistance. This is often attributed to factors such as the presence of crystalline Cr phase, lower porosity, and a homogeneous microstructure devoid of visible microcracks (as observed in Figure 4 and Table 2). It is acknowledged that corrosion typically initiates in flawed coating regions, including interconnected microcracks and pores prevalent in highly porous coatings. Additionally, various studies [53-54] have reported that chromium (Cr), a principal coating constituent, can generate a passive layer rich in chromium. This layer plays a pivotal role in preventing the dissolution of the binder matrix in sodium chloride solutions. The amalgamation of these factors underscores the enhanced corrosion resistance observed in the HVAF-fabricated WC-10Co-4Cr coating compared to its HVOF-sprayed counterpart.

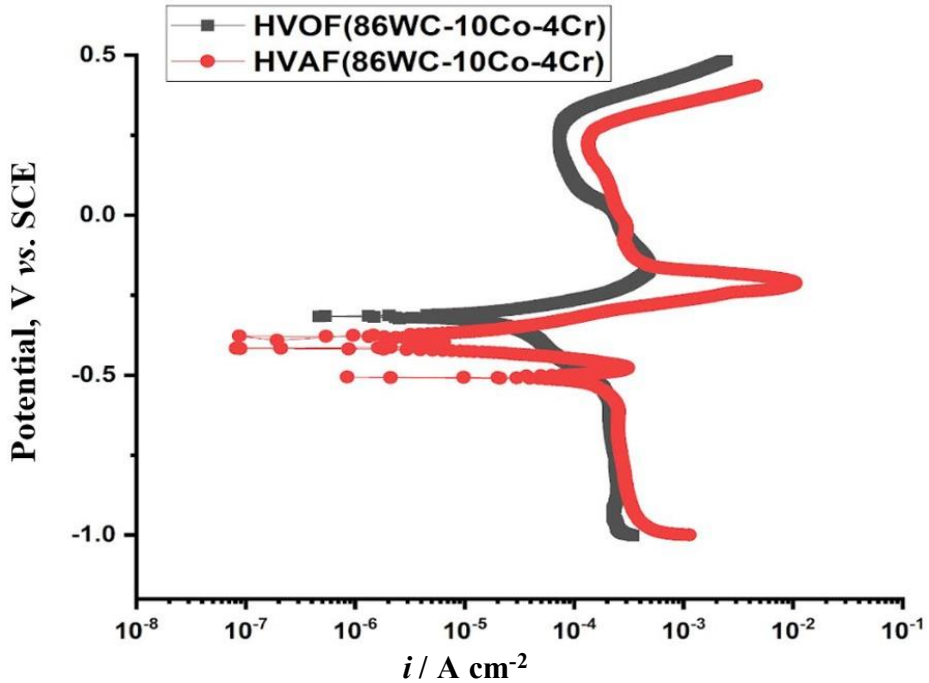

Figure 13. *Polarization curves of the HVOF/HVAF fabricated coatings in a 3.5 wt.% NaCl solution*

Table 3. *Corrosion potential and current density values of HVOF/HVAF fabricated coatings*

Coatings	*E* / V	i_{corr} / µA cm^{-2}
HVOF (86WC-10Co-4Cr)	-0.331	40
HVAF (86WC-10Co-4Cr)	-0.392	15

Analysis of corrosion specimen

Figure 14 depicts the corrosion surface morphology of HVOF/HVAF-developed WC-10Co-4Cr coatings. A significant number of WC particles were observed on the corrosion surfaces, resulting from binder material melting around the point of contact between WC particles and the binder matrix. Furthermore, the dissolution of a selective area of the binder matrix in a NaCl solution leads to WC particle dislodgement and microcavity formation [58]. The corrosion morphology depicted in

Figures 14(a) and 14(b), provides critical insights into how the HVOF/HVAF coatings respond to corrosive environments. The examination of the corrosion morphology revealed the presence of several distinctive features such as microcavities, corrosion pits, and micro-cracks as a result of the fallout of WC particles owing to binder material dissolving into NaCl. On the other hand, HVAF coating exhibits fewer microcavities, and microcracks due to reduced porosity are significant. Concurrently, an extremely thin white film forms on the surface of both coatings, caused by the presence of the Cr component in the coating material, which could produce a passive film, preventing corrosion through Cr element passivation. Other researchers observed similar phenomena in their study [59-61], particularly the formation of chromium oxide as a passive protective film on the surface of the coating, thereby suppressing the dissolution of binder material, resulting in less fall off of WC particles from the coating surface and improved corrosion resistance. According to the previous study [6,31,62], these facts may have considerable effects on the corrosion resistance of the WC-Co-Cr coating in several ways. The micro-galvanic corrosion mechanism is common in composite materials, especially those with dissimilar phases or constituents. While the WC particles are cathodically protected, the binder matrix is exposed to anodic corrosion. The oxidation of the matrix material releases metal ions into the electrolyte, resulting in the corrosion of the binder matrix. However, in comparison to coatings, the substrate material 21-4N steel has a lower corrosion potential value. When NaCl electrolyte penetrates the coating/substrate interface through micro-cracks and pores, micro galvanic corrosion could occur. Therefore, binder material subsequently dissolves around the WC particle/binder matrix interface, causing WC particles to fall out of the coating by creating corrosion cavities or pits in the coating.

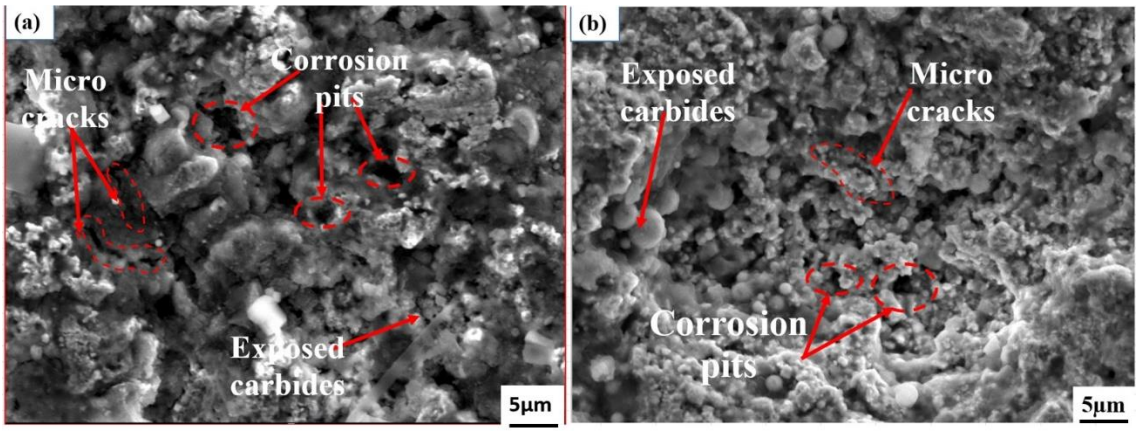

Figure 14. *Surface morphology of corroded WC-10Co-4Cr coatings: (a) HVOF and (b) HVAF*

Conclusions

1. The HVOF/HVAF fabricated WC-10Co-4Cr coatings had an appealing microstructure, and the HVAF sprayed WC-Co-Cr coating exhibited higher hardness (1582 HV), greater fracture toughness (5.69 MPa $m^{1/2}$), less decarburization, and lower porosity (0.97 %) as compared to HVOF sprayed coating.
2. The HVAF process, compared to HVOF, appears to be more effective in mitigating decarburization in the WC-10Co-4Cr coatings. This could be attributed to factors like lower combustion temperatures or the specific heating and cooling profiles associated with HVAF.
3. HVAF and HVOF fabricated coatings have demonstrated impressive performance in resisting slurry erosion and corrosion due to their high hardness and low porosity characteristics.

4. The synergistic combination of properties, which includes high hardness, fracture toughness, low porosity, a higher rate of carbide retention, and a dense structure, aids in improving the slurry erosion resistance of HVAF coatings over HVOF coatings.
5. The HVAF coating demonstrated outstanding corrosion resistance with respect to the HVOF coating, which can be attributed to its lesser porosity, consistent and bulky microstructure, and minimal cracks.
6. The damaged surface of the two coatings resulting from slurry erosion tests discloses the signs of plastic deformation, crater, gross removal of binder material, material removal by cracks coalescence in the binder matrix, and WC grain pull out owing to spalling.
7. The corrosion surface of the two coatings reveals that the binder material is susceptible to dissolution at the interface between the WC particles and the Co-Cr matrix, microcracks and corrosion pits were formed as a result of the WC particles being wiped out.

References

[1] V. Singh, A. Kumar Singla, A. Bansal, Impact of HVOF sprayed Vanadium Carbide (VC) based novel coatings on slurry erosion behaviour of hydro-machinery SS316 steel, *Tribology International* **176** (2022) 107874. https://doi.org/10.1016/j.triboint.2022.107874.

[2] V. Singh, A. Bansal, A. Kumar Singla, Response surface methodology (RSM) based analysis on slurry erosion behavior of laser textured and PTFE sprayed VC+ TiC coating deposited via HVOF, *Materials Today Communications* **36** (2023) 106843. https://doi.org/10.1016/j.mtcomm.2023.106843.

[3] V. R. Kiragi, A. Patnaik, T. Singh, G. Fekete, Parametric optimization of erosive wear response of TiAlN-coated aluminum alloy using Taguchi method, *Journal of Materials Engineering and Performance* **28** (2019) 838-851. https://doi.org/10.1007/s11665-018-3816-6.

[4] R. Kumar, K. Goyal, D. Bhandari, Slurry Erosion Behavior of Thermally Sprayed Nano YSZ Reinforced WC-10Co-4Cr Ceramic Nanocomposite Coatings, *Tribology Transactions* **66** (2023) 47-58. https://doi.org/10.1080/10402004.2022.2137446.

[5] M. Magdy EI-Rayes, M. Sherif EI-Sherif, S. Abdo Abdo, Comparative Study into Microstructural and Mechanical Characterization of HVOF-WC-Based Coatings. Crystals12 (2022) 969. https://doi.org/10.3390/cryst12070969.

[6] Y. Liu, W. Liu, Y. Ma, S. Meng, C. Liu, L. Long, S. Tang, A comparative study on wear and corrosion behaviour of HVOF-and HVAF-sprayed WC–10Co–4Cr coatings, *Surface Engineering* **33** (2007) 63-71. https://doi:10.1080/02670844.2016.1218194.

[7] H. Singh Grewal, S. Bhandari, H. Singh, Parametric study of slurry-erosion of hydro turbine steels with and without detonation gun spray coatings using Taguchi technique, *Metallurgical and Materials Transactions A* **43** (2007) 3387-3401. https://doi.org/10.1007/s11661-012-1148-y.

[8] D. Kumar Goyal, H. Singh, H. Kumar, V. Sahni, Slurry erosion behaviour of HVOF sprayed WC–10Co–4Cr and Al2O3+ 13TiO2 coatings on turbine steel, Wear **289** (2012) 46-57. https://doi.org/10.1016/j.wear.2012.04.016.

[9] G. Singh, S. Kumar, S. Satbir Sehgal, Erosion tribo performance of HVOF deposited WC-10Co-4Cr and WC-10Co-4Cr+ 2% Y2O3 micron layers on pump impeller steel, *Particulate Science and Technology* **38** (2018) 34-44. https://doi.org/10.1080/02726351.2018.1501780.

[10] G. Bolelli, L. M. Berger, T. Börner, H. Koivuluoto, L. Lusvarghi, C. Lyphout, P. Vuoristo, Tribology of HVOF-and HVAF-sprayed WC–10Co4Cr hard metal coatings: A comparative assessment, *Surface and Coatings Technology* **265** (2015) 125-144. https://doi:10.1016/j.surfcoat.2015.01.048.

[11] V. Kumar, V. Singh, R. Verma, A. Bansal, G. Ghosh, Cavitation-corrosion analysis of HVOF-sprayed WC-Co-Cr-graphene nanoplatelets coatings with LST pre-treatment. *International Journal of Refractory Metals and Hard Materials* **120** (2024) 106610. https://doi.org/10.1016/j.ijrmhm.2024.106610.

[12] K. Torkashvand, S. Joshi, V. Testa, F. Ghisoni, S. Morelli, G. Bolelli, L. Lusvarghi, F. Marra, M. Gupta, Tribological behavior of HVAF-sprayed WC-based coatings with alternative binders, *Surface and Coatings Technology* **436** (2022) 128296. https://doi.org/10.1016/j.surfcoat.2022.128296.

[13] S. L. Liu, X. P. Zheng, G. Q. Geng, Influence of nano-WC–12Co powder addition in WC–10Co–4Cr AC-HVAF sprayed coatings on wear and erosion behaviour, *Wear* **269** (2010) 362-367. https://doi.org/10.1016/j.wear.2010.04.019.

[14] Q. Wang, S. Zhang, Y. Cheng, J. Xiang, X. Zhao, G. Yang, Wear and corrosion performance of WC-10Co4Cr coatings deposited by different HVOF and HVAF spraying processes, *Surface and Coatings Technology* **218** (2013) 127-136. https://doi.org/10.1016/j.surfcoat.2012.12.041.

[15] Q. Wang, Z. Tang, L. Cha, Cavitation and sand slurry erosion resistances of WC-10Co-4Cr coatings, *Journal of Materials Engineering and Performance* **24** (2015) 2435-2443. https://doi.org/10.1007/s11665-015-1496-z.

[16] R. K. Kumar, M. Kamaraj, S. Seetharamu, A pragmatic approach and quantitative assessment of silt erosion characteristics of HVOF and HVAF processed WC-CoCr coatings and 16Cr5Ni steel for hydro turbine applications, *Materials & Design* **132** (2017) 79-95. https://doi.org/10.1016/j.matdes.2017.06.046.

[17] Y. Li, Y. Lian, J. Cao, L. Li, Solid particle erosion behavior of HVOF/HVAF sprayed WC-Co-Cr coatings, *Proceedings of the Institution of Mechanical Engineers, Part J: Journal of Engineering Tribology* **230/6** (2016): 634-643. https://doi.org/10.1177/1350650115608209.

[18] S. Hong, Y. Wu, Y. Zheng, B. Wang, W. Gao, G. Li, G. Ying, J. Lin, Effect of spray parameters on the corrosion behavior of HVOF sprayed WC-Co-Cr coatings, *Journal of materials engineering and performance* **23** (2014)1434-1439. https://doi.org/10.1007/s11665-014-0865-3

[19] A. Sharma, S. K. Goel, Erosion behavior of WC–10Co–4Cr coating on 23-8-N nitronic steel by HVOF thermal spraying. Applied Surface Science **370** (2016): 418-426. https://doi.org/10.1016/j.apsusc.2016.02.163.

[20] Q. Wang, S. Luo, S. Wang, H. Wang, C. Seshadri Ramachandran, Wear, erosion and corrosion resistance of HVOF-sprayed WC and Cr_3C_2 based coatings for electrolytic hard chrome replacement, *International Journal of Refractory Metals and Hard Materials* **81** (2019) 242-252. https://doi.org/10.1016/j.ijrmhm.2019.03.010.

[21] A Kumar Singla, A. Bansal, V. Singh, N. Khanna, D. Kumar Goyal, J. Singla, Satish Tailor, Development, characterization, and cavitation erosion analysis of high velocity oxy-fuel (HVOF) sprayed TiC and (70Cu-30Ni)-Cr based composite coatings on SS316 steel, *Tribology International* **186** (2023) 108621. https://doi.org/10.1016/j.triboint.2023.108621

[22] V. Singh, A. Bansal, A. Kumar Singla, D. Kumar Goyal, N. Khanna, Modification of SS316 steel with the assistance of high velocity oxy fuel (HVOF) process to upsurge its sustainability, In *Sustainable Materials and Manufacturing Technologies*, . CRC Press, 2023. 182-195. https://doi.org/10.1201/9781003291961

[23] X. Liu, J. Kang, W. Yue, Z. Fu, L. Zhu, D. She, J. Liang, C. Wang, Performance evaluation of HVOF sprayed WC-10Co4Cr coatings under slurry erosion, *Surface Engineering,* **35** (2019) 816-825. https://doi.org/10.1080/02670844.2019.1568661.

[24] V. Singh, A. Kumar Singla, A. Bansal, Influence of TiC Content on Slurry Erosion Behaviour of HVOF Sprayed Titanium Carbide and Cupronickel-Chromium Based Coatings, *Journal of Thermal Spray Technology* **32** (2023) 1739-1757. https://doi.org/10.1007/s11666-023-01613-2.

[25] N. Kumar, N. Arora, S. K. Goel, Slurry erosion study on nitrogen-alloyed austenitic stainless steel and weld beads, *Tribology Letters* **68** (2020) 92. https://doi.org/10.1007/s11249-020-01332-7.

[26] A. K. Chauhan, D. B. Goel, S. Prakash, Erosive wear of a surface coated hydro turbine steel, *Bulletin of Materials Science* **33** (2010) 483-489. https://doi.org/10.1007/s12034-010-0074-0.

[27] A. Kumar, A. Sharma, S. K. Goel, Effect of heat treatment on microstructure, mechanical properties and erosion resistance of cast 23-8-N nitronic steel, *Materials Science and Engineering A* **637** (2015) 56-62. https://doi.org/10.1016/j.msea.2015.04.031.

[28] H. Myalska, K. Szymański, G. Moskal, Microstructure and selected properties of WC-Co-Cr coatings deposited by high-velocity thermal spray processes, *Solid State Phenomena* **246** (2016) 117-122. https://doi.org/10.4028/www.scientific.net/ssp.246.117.

[29] S. L. Liu, X. P. Zheng, G. Q. Geng, Influence of nano-WC–12Co powder addition in WC–10Co–4Cr AC-HVAF sprayed coatings on wear and erosion behaviour, *Wear* **269** (2010) 362-367. https://doi.org/10.1016/j.wear.2010.04.019.

[30] K. Torkashvand, V. Krishna Selpol, M. Gupta, S. Joshi, Influence of test conditions on sliding wear performance of high-velocity air fuel-sprayed WC–CoCr coatings, *Materials* **14** (2021) 3074. https://doi.org/10.3390/ma14113074.

[31] Q. Wang, S. Zhang, Y. Cheng, J. Xiang, X. Zhao, G. Yang, Wear and corrosion performance of WC-10Co4Cr coatings deposited by different HVOF and HVAF spraying processes, *Surface and Coatings Technology* **218** (2013) 127-136. https://doi.org/10.1016/j.surfcoat.2012.12.041.

[32] K. Ofelia Méndez-Medrano, C. Jesús Martínez-González, F. Alvarado-Hernández, O. Jiménez, Víctor Hugo Baltazar-Hernández, H. Ruiz-Luna, Microstructure and properties characterization of WC-Co-Cr thermal spray coatings, *Journal of Minerals and Materials Characterization and Engineering* **6** (2018) 482-497. https://doi.org/10.4236/jmmce.2018.64034.

[33] M. M. El Rayes, E. M. Sherif, H. S. Abdo, Comparative Study into Microstructural and Mechanical Characterization of HVOF-WC-Based Coatings, *Crystals* **12** (2022) 969. https://doi.org/10.3390/cryst12070969.

[34] D. Naha, S. Chatterjee, M. Ghosh, J. Dutta Majumdar, A. Majumdar, HVOF sprayed WCCocr coating on mild steel: microstructure and wear evaluation, *IOSR J. Appl. Phys.* **8** (2016) 47-56. https://doi.org/10.9790/4861-08114756.

[35] K. Fan, W. Jiang, V. Luiz, T. Gong, W. Feng, J. Ruiz-Hervias, P. Yao, Influence of WC Particle Size on the Mechanical Properties and Residual Stress of HVOF Thermally Sprayed WC–10Co–4Cr Coatings, *Materials* **15** (2022) 5537. https://doi.org/10.3390/ma15165537.

[36] L. Chang, W. Wang, D. Ma, J. Xie, Deposition effects and interface structure of HVOF-sprayed multimodal WC-CoCr coatings, *Journal of Materials Research* **38** (2023) 4345-4356. https://doi.org/10.1557/s43578-023-01147-x.

[37] A. Karimi, C. Verdon, G. Barbezat, Microstructure and hydro abrasive wear behaviour of high-velocity oxy-fuel thermally sprayed WC-Co (Cr) coatings, *Surface and Coatings Technology* **57** (1993) 81-89. https://doi.org/10.1016/0257-8972(93)90340-T.

[38] A. Garfias Bulnes, V. Albaladejo Fuentes, I. Garcia Cano, S. Dosta, Understanding the influence of high-velocity thermal spray techniques on the properties of different anti-wear WC-based coatings, *Coatings* **10** (2020) 1157. https://doi.org/10.3390/coatings10121157.

[39] Y. Y. Santana, L. JG Barbera-Sosa, J. Caro, E. S. Puchi-Cabrera, M. H. Staia, Mechanical properties and microstructure of WC–10Co–4Cr and WC–12Co thermal spray coatings deposited by HVOF, *Surface engineering* **24** (2008) 374-382. https://doi.org/10.1179/174329408X326380.

[40] D. Kumar Goyal, H. Singh, H. Kumar, V. Sahni, Slurry erosive wear evaluation of HVOF-spray Cr 2 O 3 coating on some turbine steels, *Journal of thermal spray technology* **21** (2012) 838-851. https://doi.org/10.1007/s11666-012-9795-5.

[41] M. Aminul Islam, T. Alam, Z. N. Farhat, A. Mohamed, A. Alfantazi, Effect of microstructure on the erosion behavior of carbon steel, *Wear* **332** (2015) 1080-1089. https://doi.org/10.1016/j.wear.2014.12.004.

[42] I. A. Maekai, G. A. Harmain, Influence of operating parameters on slurry erosion of stainless steel f6nm, *Tribology in Industry* **42** (2020) 236. https://doi.org/10.24874/ti.780.10.19.02.

[43] C. S. Ramesh, D. S. Devaraj, R. Keshavamurthy, B. R. Sridhar, Slurry erosive wear behaviour of thermally sprayed Inconel-718 coatings by APS process, *Wear* **271** (2011) 1365-1371. https://doi.org/10.1016/j.wear.2011.01.057.

[44] S. Bhandari, H. Singh, H. Kumar, V. Rastogi, Slurry erosion performance study of detonation gun-sprayed WC-10Co-4Cr coatings on CF8M steel under hydro-accelerated conditions, *Journal of thermal spray technology* **21** (2012) 1054-1064. https://doi.org/10.1007/s11666-012-9799-1.

[45] M. H. Buszko, A. K. Krella, An influence of factors of flow condition, particle and material properties on slurry erosion resistance, *Advances in Materials Science* **19** (2019) 28-53. https://doi.org/10.2478/adms-2019-0010.

[46] G. Santacruz, A. Shigueaki Takimi, F. Vannucchi de Camargo, C. Pérez Bergmann, Cristiano Fragassa, Comparative study of jet slurry erosion of martensitic stainless steel with tungsten carbide HVOF coating, *Metals* **9** (2019) 600. https://doi.org/10.3390/met9050600.

[47] J. Malik, I. H. Toor, W. H. Ahmed, Z. M. GaSEM, M. A. Habib, R. Ben-Mansour, and H. M. Badr, Evaluating the effect of hardness on erosion characteristics of aluminum and steels, *Journal of materials engineering and performance* **23** (2014) 2274-2282. https://doi.org/10.1007/s11665-014-1004-x

[48] J. Singh, Analysis on suitability of HVOF sprayed Ni-20Al, Ni-20Cr and Al-20Ti coatings in coal-ash slurry conditions using artificial neural network model, *Industrial Lubrication and Tribology* **71** (2019) 972-982. https://doi.org/10.1108/ILT-12-2018-0460.

[49] R. Kumar, S. Kumar, D. Mudgal, Silt erosion performance of high velocity oxy fuel-(HVOF) sprayed Al2O3–Cr2O3 composite coatings on turbine steel, *Industrial Lubrication and Tribology* **74** (2022) 572-579. https://doi.org/10.1108/ILT-08-2021-0346.

[50] J. Du, J. Zhang, J. Xiao, C. Zhang, Slurry erosion behavior of HVOF sprayed WC-12Co and Cr3C2-25NiCr coatings deposited on 16Cr5Ni stainless steel, *Surface Review and Letters* **27** (2020) 1950193. https://doi.org/10.1142/S0218625X19501932.

[51] H. S. Grewal, H. S. Arora, A. Agrawal, H. Singh, S. Mukherjee, Slurry erosion of thermal spray coatings: effect of sand concentration, *Procedia Engineering* **68** (2013) 484-490. https://doi.org/10.1016/j.proeng.2013.12.210.

[52] V. Singh, A. Kumar Singla, A. Bansal, Influence of laser texturing along with PTFE topcoat on slurry and cavitation erosion resistance of HVOF sprayed VC coating, *Surface and Coatings Technology* **470** (2023) 129858. https://doi.org/10.1016/j.surfcoat.2023.129858.

[53] S. Brioua, K. Belmokre, V. Debout, P. Jacquot, E. Conforto, S. Touzain, Jordi Creus, Corrosion behavior in artificial seawater of thermal-sprayed WC-CoCr coatings on mild steel by electrochemical impedance spectroscopy, *Journal of solid state electrochemistry* **16** (2012) 633-648. https://doi.org/10.1007/s10008-011-1403-y

[54] Y. Huang, X. Ding, C. Yuan, Z. Yu, Z. Ding, Slurry erosion behaviour and mechanism of HVOF sprayed micro-nano structured WC-CoCr coatings in NaCl medium, *Tribology International* **148** (2020) 106315. https://doi.org/10.1016/j.triboint.2020.106315.

[55] M. Sharma, D. Kumar Goyal, G. Kaushal, Tribological investigation of HVOF-sprayed coated turbine steel under varied slurry erosion conditions, Material proceedings **24** (2020) 869-879. https://doi.org/10.1016/j.matpr.2020.04.397.

[56] X. Liu, J. Kang, W. Yue, Z. Fu, L. Zhu, D. She, J. Liang, C. Wang, Performance evaluation of HVOF sprayed WC-10Co4Cr coatings under slurry erosion, *Surface Engineering* **35** (2019) 816-825. https://doi.org/10.1080/02670844.2019.1568661.

[57] D. C. Ribu, R. Rajesh, D. Thirumalaikumarasamy, A. R. Kaladgi, C. A. Saleel, K.S. Nisar, A. Afzal, Experimental investigation of erosion-corrosion performance and slurry erosion mechanism of HVOF sprayed WC-10Co coatings using design of experiment approach. Journal of Materials Research and Technology, **18** (2022), 293-314. https://doi.org/10.1016/j.jmrt.2022.01.134.

[58] E. Sadeghimeresht, N. Markocsan, P. Nylén, A comparative study of corrosion resistance for HVAF-sprayed Fe-and Co-based coatings, *Coatings* **6** (2016) 16. https://doi.org/10.3390/coatings6020016.

[59] T. Arunnellaiappan, S. Baskaran, S. Arun, R. Prithivirajan, Corrosion behaviour of detonation gun sprayed cermet coatings on AA5083, *Surface Engineering* **37** (2021) 263-270. https://doi.org/10.1080/02670844.2020.1807096.

[60] J. A. Picas, E. Rupérez, M. Punset, A. Forn, Influence of HVOF spraying parameters on the corrosion resistance of WC–CoCr coatings in strong acidic environment, *Surface and Coatings Technology* **225** (2013) 47-57. https://doi.org/10.1016/j.surfcoat.2013.03.015.

[61] F. Wang, F. Zhang, L. Zheng, H. Zhang, Structure and corrosion properties of Cr coating deposited on aerospace bearing steel, *Applied Surface Science* **423** (2017) 695-703. https://doi.org/10.1016/j.apsusc.2017.06.099.

[62] J. E. Cho, S. Y. Hwang, K. Y. Kim, Corrosion behavior of thermal sprayed WC cermet coatings having various metallic binders in strong acidic environment, *surface and coatings technology* **200** (2006) 2653-2662. https://doi.org/10.1016/j.surfcoat.2004.10.142.